Substrate-Dependent Photodetection with Functional Nanomaterials

Dissertation
der Mathematisch-Naturwissenschaftlichen Fakultät
der Eberhard Karls Universität Tübingen
zur Erlangung des Grades eines
Doktors der Naturwissenschaften
(Dr. rer. nat.)

vorgelegt von
Christine Alexandra Schedel
aus Göppingen

Tübingen
2022

Gedruckt mit Genehmigung der Mathematisch-Naturwissenschaftlichen Fakultät der Eberhard Karls Universität Tübingen.

Tag der mündlichen Qualifikation:	21.10.2022
Dekan:	Prof. Dr. Thilo Stehle
1. Berichterstatter/-in:	Prof. Dr. Marcus Scheele
2. Berichterstatter/-in:	Prof. Dr. Thomas Chassé

This dissertation was carried out in the group of Prof. Dr. Marcus Scheele at the Institute of Physical and Theoretical Chemistry of the Eberhard Karls University of Tübingen between May 2018 and July 2022.

To my parents.

Abstract

The speed of response of a photodetector is influenced by many factors, including the geometry of the device, the photoabsorber, and the electrodes. A wide variety of substrate materials such as Si/SiO$_2$, glass, sapphire, and several flexible polymer foils are used in the fabrication of these detectors. Although the dielectric influences on nanostructured materials often used as photoabsorbers are widely known, the influence of the substrate on the performance of photodetectors, especially with respect to their speed of response, is scarcely explored.

This work focuses on the influence of the substrate on the speed of response of otherwise identical photodetectors. Firstly, the setup is presented that was developed for the time-resolved photocurrent studies. Both, the response of a detector towards a laser impulse and a laser square pulse illumination, need to be investigated for the complete study of the photodetector response. The impulse response of the detector displays its non-steady state behavior and information about present decay mechanisms can be obtained. This is important for the application of the device in telecommunication, where short, delta-shaped laser impulses are utilized for data transmission. Illumination with a square pulse of sufficient pulse width to reach steady state conditions in the photodetector allows to estimate the factor that limits its speed of response (RC time, transit time, diffusion time or recombination time). The time-resolved responses towards both techniques are governed by the slowest time component present in the detector. The accuracy of the developed setup is confirmed by an examination of commercial photodetectors.

Then, it is shown that Si/SiO$_2$ cannot be used as substrate for such time-resolved photoelectrical studies under visible illumination, because the silicon generates a photocurrent signal itself. Hence, soda-lime glass with a high dielectric constant and the polyimide poly(4,4'-oxydiphenylene pyromellitimide), also known as Kapton HN, with smaller dielectric constant, are utilized as substrate materials. The influence of these two substrates on two different classes of nanostructured photoabsorbers with outstanding optoelectronic properties, namely CdSe quantum dots and WSe$_2$, is subsequently presented.

Thin films of iodide-capped CdSe quantum dots that are sensitized with zinc β-tetraaminophthalocyanine (CdSe/I$^-$/Zn4APc) absorb not only in the visible range but also in the first telecommunication window, thus, this material is a very interesting photoabsorber. When deposited on top of glass and polyimide, CdSe/I$^-$/Zn4APc thin films show distinct differences in their speed of response under illumination with a laser impulse. CdSe/I$^-$/Zn4APc films deposited on polyimide have a significantly diminished tail current compared to the glass devices. This is due to the smaller dielectric constant of polyimide that allows fewer trap states near the substrate / semiconductor interface to be occupied, making the multiple trapping and release mechanism less pronounced. It leads to an enhanced 3 dB bandwidth of 85 kHz for detectors on polyimide, vs. 67 kHz for devices on glass. On the contrary, a comparable decay behavior is observed on both substrates under square pulse illumination reaching steady state photocurrent, since all trap states are saturated at long

illumination times. Because of high photoresistances, even for channel lengths of only 350 nm, all photodetectors are RC limited.

To obtain faster photodetectors, the photoresistance must be reduced. This requires materials with higher charge carrier mobilities than those present in CdSe/I^-/Zn4APc. WSe_2 as layered van der Waals material not only offers high charge carrier mobilities, but also exhibits rich excitonic features that makes this material an interesting candidate for optoelectronic applications. Indeed, examined photodetectors using WSe_2 as the active material have a faster response than the ones based on CdSe/I^-/Zn4APc. The speed of response of the photodetectors when using polyimide and glass as substrate is examined in detail. When WSe_2 is attached on polyimide, the detector is RC limited, whereas on glass, excitonic diffusion processes arise. The strong dielectric screening of glass reduces the depletion width at the metal / semiconductor interface compared to the situation on polyimide and with that alters the factor that limits the speed of the detector. On glass, the 3 dB bandwidth can be tuned up to 2.6 MHz with an increasing electric field. This acceleration of the glass detectors can be seen in both impulse and square pulse investigations.

In summary, this work provides experimental evidence that the choice of the substrate is an important aspect when high-speed photodetectors are to be developed and that it should be given more consideration in the future than it has received so far.

Zusammenfassung

Die Geschwindigkeit eines Photodetektors wird von vielen Faktoren beeinflusst, dazu zählen die Geometrie des Bauteils, der Photoabsorber und die Elektroden. Zahlreiche Substratmaterialien werden bei der Herstellung dieser Geräte genutzt, wie beispielsweise Si/SiO$_2$, Glas, Saphir und einige flexible Polymerfolien. Obwohl die dielektrischen Einflüsse auf nanostrukturierte Materialien, die häufig als Photoabsorber verwendet werden, weithin bekannt sind, ist der Einfluss des Substrats auf die Leistung der Photodetektoren, insbesondere im Hinblick auf ihre Geschwindigkeit, kaum erforscht.

Diese Arbeit konzentriert sich auf den Einfluss des Substrates auf die Geschwindigkeit von ansonsten identischen Photodetektoren. Zunächst wird der Messaufbau vorgestellt, der für die zeitaufgelösten Photostromstudien entwickelt wurde. Für die vollständige Untersuchung der Photostromantwort eines Detektors müssen sowohl dessen Reaktion auf einen Laserimpuls als auch auf einen Rechteckspuls untersucht werden. Die Impulsantwort des Detektors zeigt sein instationäres (Nicht-Gleichgewichts-)Verhalten auf und es können Informationen über vorliegende Abklingmechanismen gewonnen werden. Dies ist wichtig für die Anwendung des Detektors in der Telekommunikation, in der kurze, deltaförmige Laserimpulse für die Datenübertragung eingesetzt werden. Die Beleuchtung des Detektors mit einem Rechteckspuls, dessen Pulsbreite ausreicht, um den Gleichgewichtszustand zu erreichen, ermöglicht die Abschätzung des geschwindigkeitsbegrenzenden Faktors (RC Zeit, Transitzeit, Diffusionszeit oder Rekombinationszeit). Das Antwortverhalten des Detektors wird bei beiden Techniken von der langsamsten Zeitkomponente bestimmt, die im Bauteil vorliegt. Die Genauigkeit des entwickelten Aufbaus wird durch die Untersuchung kommerzieller Photodetektoren bestätigt.

Dann wird gezeigt, dass Si/SiO$_2$ bei Verwendung von sichtbarer Strahlung nicht als Substrat für solch zeitaufgelöste photoelektrische Studien verwendet werden kann, weil das Silizium selbst bereits ein Photostromsignal erzeugt. Daher werden Kalk-Natron-Glas mit einer hohen Dielektrizitätskonstante und das Polyimid Poly(4,4'-oxydiphenylenpyromellitimid), auch bekannt als Kapton HN, mit einer geringeren Dielektrizitätskonstante als Substratmaterialien verwendet. Der Einfluss dieser beiden Substrate auf zwei unterschiedliche nanostrukturierte Photoabsorberklassen mit herausragenden optoelektronischen Eigenschaften, nämlich CdSe Quantenpunkte und WSe$_2$, wird daraufhin dargelegt.

Dünnschichten von Iodid-umhüllten CdSe Quantenpunkten, die mit Zink-β-tetraaminophthalocyanin sensibilisiert sind (CdSe/I$^-$/Zn4APc), absorbieren nicht nur im sichtbaren Bereich, sondern auch im ersten Telekommunikationsfenster, was dieses Material zu einem sehr interessanten Photoabsorber macht. Auf Glas und Polyimid aufgebracht ergeben sich deutliche Unterschiede in der Geschwindigkeit der Detektoren bei Beleuchtung mit einem Laserimpuls. CdSe/I$^-$/Zn4APc Schichten auf Polyimid weisen im Vergleich zu den Glasbauteilen einen deutlich geringeren Photostrom beim Abklingen des Signals auf. Dies ist auf die geringere Dielektrizitätskonstante von Polyimid zurückzuführen, die es weniger Fallenzuständen in der Nähe der Substrat / Halbleiter-Grenzfläche erlaubt, besetzt zu werden.

Dadurch ist der Mechanismus des mehrfachen Einfangens und Freisetzens (engl.: multiple trapping and release mechanism) auf Polyimid weniger stark ausgeprägt. Es ergibt sich eine verbesserte 3 dB Bandbreite von 85 kHz für die Detektoren auf Polyimid im Vergleich zu 67 kHz für diejenigen auf Glas. Im Gegensatz zur Impulsbeleuchtung wird unter Rechteckspulsbeleuchtung ein vergleichbares Abklingverhalten auf beiden Substraten beobachtet, da alle Fallenzustände bei langen Beleuchtungszeiten gesättigt sind. Aufgrund der hohen Photowiderstände sind alle Detektoren selbst bei Kanallängen von nur 350 nm RC limitiert.

Um schnellere Photodetektoren zu erhalten, muss der Photowiderstand verringert werden. Dies erfordert Materialien, die höhere Ladungsträgerbeweglichkeiten besitzen als CdSe/I^-/Zn4APc. WSe_2 als van-der-Waals Schichtmaterial bietet nicht nur eine hohe Ladungsträgerbeweglichkeit, sondern weist auch zahlreiche exzitonische Eigenschaften auf, was dieses Material zu einem interessanten Kandidaten für optoelektronische Anwendungen macht. Die untersuchten Photodetektoren, die WSe_2 als aktives Material nutzen, sind tatsächlich schneller als solche, die auf CdSe/I^-/Zn4APc basieren. Die Geschwindigkeit dieser Photodetektoren wird bei Verwendung von Polyimid und Glas als Substrat untersucht. Wird WSe_2 auf Polyimid aufgebracht, so ist der Detektor RC limitiert, während bei den Detektoren auf Glas exzitonische Diffusionsprozesse auftreten. Die starke dielektrische Abschirmung von Glas verkürzt die Verarmungszone der Metall / Halbleiter-Grenzfläche im Vergleich zur Situation auf Polyimid und verändert damit den geschwindigkeitsbegrenzenden Faktor des Detektors. Auf Glas kann eine 3 dB Bandbreite von bis zu 2.6 MHz ermittelt werden, wenn das elektrische Feld erhöht wird. Diese Beschleunigung der Glasdetektoren lässt sich sowohl bei Impuls- als auch bei Rechteckpulsuntersuchungen beobachten.

Zusammenfassend kann gesagt werden, dass diese Arbeit experimentelle Beweise dafür liefert, dass die Wahl des Substrates einen wichtigen Aspekt bei der Entwicklung von Hochgeschwindigkeitsphotodetektoren darstellt und in Zukunft stärker als bisher erfolgt berücksichtigt werden sollte.

Contents

1

Introduction

1.1 Motivation

The first report on photoconductivity dates back to 1873, when W. Smith observed a change in the resistance of selenium under different intensities of illumination[1] with its spectral dependence being discussed by Sale[2] in the same year. Shortly afterwards, in 1876, W. Adams and R. Day reported on the photovoltaic effect of a selenium photocell.[3] Nowadays, photodetectors are used quite frequently in both photoconductive and photovoltaic mode and are utilized for example in telecommunication, industrial control, medical health care, for environmental monitoring, and as cameras for optical imaging and in night vision. These applications place different requirements on the detectors regarding speed, responsivity, quantum yield, and spectral response.

High-speed photodetectors are particularly needed in optical communications, where they are used as interconnects in data transfer. Light signals in optical fibers are used for long-distance data transmission, while data processing is performed electrically in the computer using field-effect transistors in integrated circuits. Hence, an optical switch is required to convert the optical signal into an electronic one. This process is rather slow compared to the speed of transmission within an optical fiber[4] and the switching speed of a transistor[5]. With an acceleration of the photodetection process, data transfer can be accelerated overall.[6] The so-called telecommunication windows are located in the near infrared (NIR) with three practical bands at 850 nm (first window), 1.3 µm (second window) and 1.55 µm (third window), where optical fibers are optimized for their attenuation and absorption properties.[7, 8] However, high-speed photodetectors are also required for the visible (vis) range due to data transmission by means of visible light communication.[9, 10] Even though this is a niche technology that could be used as an information transmitter in light spots in museums or at exhibitions, its importance should not be underestimated. It enables tap-proof data transmission in closed spaces, enhancing communication security considerably, and minimizing electromagnetic interference, e.g., in airplanes or hospitals.

Most of the electronics today is based on silicon, which is also regularly used in photodetectors. However, it has limited capabilities due to its indirect band gap at 1.1 eV and several emerging materials have been suggested to replace it as active material in photodetectors. Nanostructured materials are of particular interest because quantum confinement creates novel properties that distinguish them from their conventional 3D counterparts. Thus, quantum dots, nanowires and nanosheets have become the focus of interest.[11, 12] In this work, the performance of CdSe quantum dot (QD) and WSe_2 photodetectors is examined.

In order to accelerate the speed of response of photodetectors, many investigations are devoted towards the development of the photoabsorbing material, where, e.g., QD photodetectors can be modulated by trap state engineering[13-16] and transition metal dichalcogenides (TMDCs) are modulated due to surface oxidation / doping.[17-19] While using the same active material, the choice of the electrode metal can accelerate the photoresponse[20-26] and also the electrode geometry has to be considered.[27-30] In addition, strain can influence the speed of a photodetector, which is examined frequently.[31-36] In contrast, although it is well known that surface and interface engineering has a great influence on nanostructured systems[37], to the best of my knowledge, very few studies are available regarding the influence of the substrate on the performance of photodetectors, especially with regard to the speed of the detectors.

GaS nanosheets have been studied by Hu et al. in 2013 on both Si/SiO_2 and polyethylene terephthalate (PET) substrates and distinct differences on responsivity, external quantum efficiency and linear dynamic range have been reported.[38] The authors hypothesize that trap states at the SiO_2 surface might play an important role in this context. However, the influence of the substrate towards the speed of the GaS photodetector response could not be investigated due to setup limitations.

In 2013, Lopez-Sanchez et al. mentioned the influence of different growth techniques and surface treatments of the substrate Si/SiO_2 on not only the responsivity but also the speed of response of a monolayer MoS_2 photodetector. Very large differences in photoresponse decay times were reported, ranging from 0.3 to 4000 s.[22] They were attributed to differing surface hydrophobicities as both, adsorbed moisture on MoS_2[39] and different silanol group densities on the surface of SiO_2 substrates for graphene devices[40], are reported to have an significant influence on the electronic properties.

Kufer et al. examined mono- and bilayer MoS_2 photodetectors in 2015 and checked the influence of a HfO_2 encapsulation.[19] The temporal response could be accelerated considerably with a HfO_2 layer on top of the MoS_2 from approx. 120 ms to 8 ms, which was ascribed solely to the removal of surface bound oxygen and water due to protection of the device from the atmosphere. The possible influence of the changed dielectric environment was not discussed.

Cui et al. investigated Ga_2O_3 detectors in 2017 on both quartz and polyethylene naphthalate (PEN) substrates but concentrated on the influence of oxygen vacancies towards the speed of the photoresponse.[41] The authors showed that for varying amounts of oxygen defects in Ga_2O_3 the performance of the photodetectors on quartz and PEN is comparable, but they did not perform in-depth comparative studies.

A more detailed investigation on both the responsivity and the speed of the photoresponse was shown by E et al. in 2020. They investigated BeZnO alloy on sapphire, PET and PEN.[42] The photocurrent rise and fall under square pulse illumination was fitted biexponentially with the fast component of the recovery (fall) time being in the range of 9 ms up to 16 ms and the slow one in between 34 ms to 76 ms, depending on the substrate used. The overall rapid recovery was ascribed to a high density of defect states working as recombination centers in the amorphous film. Similarly, the response (rise) times of the detectors vary, however, differences of the substrates and their influences towards the response and recovery time constants are not discussed.

In 2021, Cadatal-Raduban et al. investigated TiO_2 thin films on silicon, quartz and soda-lime glass.[43] The responsivity varied significantly, whereas the estimated fall time is roughly the same, with minor variations ascribed to different crystallinities of the TiO_2 film on the three substrates.

Environmental effects of the KOH electrolyte concentration on the responsivity of a photoelectrochemical Nb_2C photodetector deposited on indium tin oxide (ITO) coated glass was shown by Gao et al in 2021, but no variation in the speed of the detector was observed.[44] In contrast, when the active material was applied on a Si/SiO_2 substrate and measured in air, the detector was strongly slowed down. The authors ascribed this to a possible oxidation of Nb_2C and did not investigate the time-dependent photoresponses of the different devices further.

There are even photodetector studies in which the utilized substrate material is not mentioned[13, 45], which further emphasizes how little attention has been devoted to this aspect in the development of photodetectors to date.

1.2 Objective

Photodetectors for optical communication need to fulfill high requirements. Users are demanding continually increasing data transfer rates, and to ensure this, photodetectors must be accelerated. Therefore, new materials have to be examined with regard to their photoelectronic properties, and combining inorganic nanostructures with organic semiconductors offers a wide range of possibilities to tune the material properties.

The aim of this thesis was to establish a setup for time-resolved photocurrent studies and to perform first investigations of the speed of the photoresponse of nanostructured materials within the framework of the so-called “Coupled Organic Inorganic Nanostructures for Fast, Light-Induced Data Processing” (COINFLIP)[46-48] project. Materials of interest are CdSe QDs sensitized with the dye zinc β-tetraaminophthalocyanine and WSe_2 crystals. In this context, the effect of different substrate materials on the speed of otherwise identical photodetectors should be examined in more detail. Therefore, I investigated photodetectors based on a silicon wafer with thermally grown SiO_2 layer (Si/SiO_2), on glass and on the polyimide poly(4,4'-oxydiphenylene pyromellitimide), also known as Kapton HN.

1.3 Outline of this Thesis

The relevant theoretical background is presented in Chapter 2 – “Photodetection with Functional Nanomaterials”. An introduction to photodetection is provided with a detailed overview of the common types of photoelectric photodetectors, focusing on the speed of the devices. The two techniques employed in this thesis, the illumination of a detector with a very short laser pulse (named impulse illumination) and the illumination with a suitably long square pulse reaching steady state conditions in the photoresponse (named square pulse illumination), are introduced. In addition, fundamental aspects of nanostructured materials are given, in specific for the investigated CdSe QDs and the transition metal dichalcogenide (TMDC) WSe_2. A brief overview of known influences of a dielectric on the material classes examined is provided.

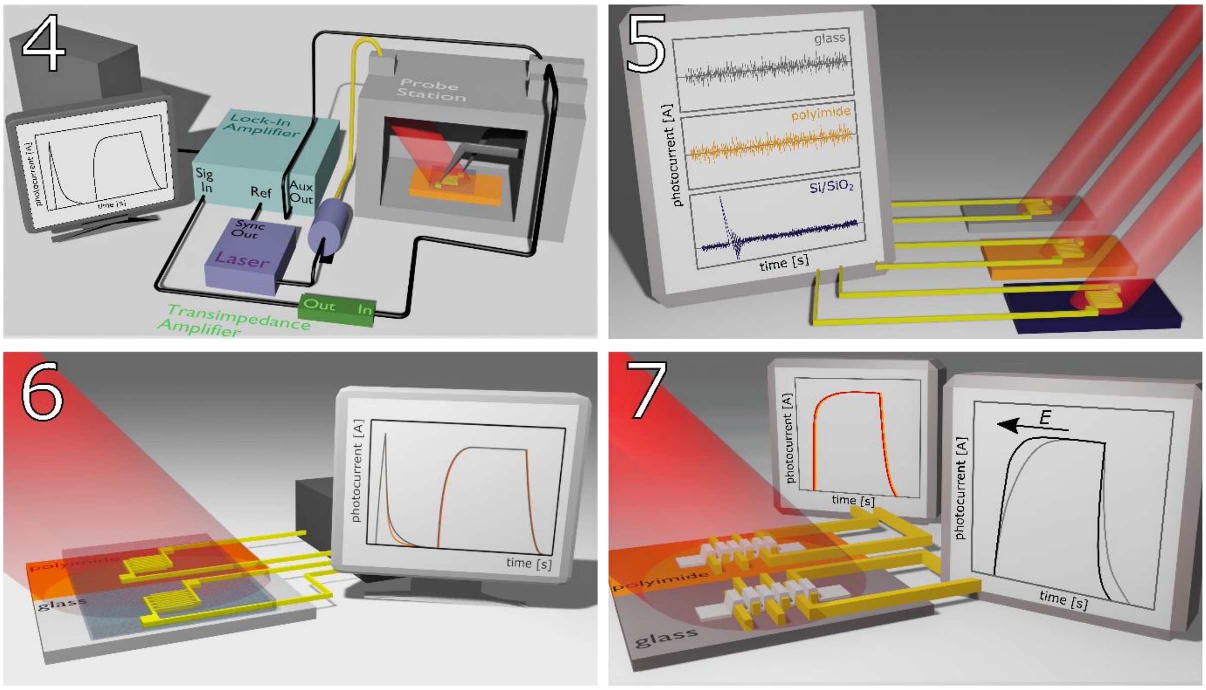

Figure 1.1. Graphical Outline of this Thesis. Chapter 4: “Proof of Concept: The Time-Resolved Photocurrent Setup”, Chapter 5: “Substrate Selection”, Chapter 6: “Substrate Effects on the Bandwidth of CdSe Quantum Dot Photodetectors”, reprinted with permission from Schedel et al.[49] Copyright 2021, American Chemical Society. Chapter 7: “Substrate Effects on the Speed Limiting Factor of WSe_2 Photodetectors”, reprinted with permission from Schedel et al.[50] Copyright 2022, the Royal Society of Chemistry (PCCP Owner Societies).

In Chapter 3 – “Methods and Materials” the developed setup is described, and the other methods used are reported. Furthermore, the investigated photodetectors and their preparation are described in detail.

To verify the accuracy of the established setup, I examined commercial photodetectors. These results are presented in Chapter 4 – "Proof of Concept: The Time-Resolved Photocurrent Setup". The square pulse and impulse illumination techniques are demonstrated, and the electrical bandwidth determination used in this work is presented. The graphical presentation of the developed time-resolved photocurrent setup is given in panel 4 of Figure 1.1.

If a semiconductor is to be investigated as active material for a high-speed photodetector, not every material can be exploited as substrate for the detector. Chapter 5 – “Substrate Selection” deals with this observation using the example of a Si/SiO_2 wafer and briefly introduces the substrate materials chosen for this work, glass and polyimide. Si/SiO_2 being not suitable as substrate for time-resolved photoinvestigations using visible light illumination is published in ACS Materials and Interfaces, included in the paper “Substrate Effects on the Bandwidth of CdSe Quantum Dot Photodetectors”.[49] The graphical illustration of this Chapter is given in panel 5 of Figure 1.1.

The studies of iodide-capped CdSe QD photodetectors crosslinked with the dye zinc β-tetraaminophthalocyanine (Zn4APc), named in the following as CdSe/I^-/Zn4APc, are presented in Chapter 6 with the figure of content shown in panel 6 of Figure 1.1. Both, the response towards a laser impulse (= impulse or non-steady state photoresponse) and towards a square pulse (= square pulse or steady state response), of detectors on glass and polyimide are investigated. Significant differences in the speed of the impulse responses are observed for different substrates, with an electrical bandwidth of 85 kHz on polyimide, whereas identical QD detectors on glass are limited to 67 kHz. The time limitation of both detectors, the resistance – capacitance (RC) time, is discussed and a way to reduce it is demonstrated. The results presented in this Chapter are published in ACS Materials and Interfaces, bearing the same title "Substrate Effects on the Bandwidth of CdSe Quantum Dot Photodetectors".[49]

To circumvent very high resistances, such as those limiting the performance of the CdSe/I^-/Zn4APc photodetectors in Chapter 6, the advantages offered by layered structures should be exploited and WSe_2 photodetectors are presented in Chapter 7 – "Substrate Effects on the Speed Limiting Factor of WSe_2 Photodetectors". Polyimide and glass are used as substrate materials. The devices based on polyimide are RC limited, whereas the ones on glass are limited by excitonic diffusion processes, which is visible in both impulse and square pulse photoresponses. With that, the bandwidth of the detectors on glass can be increased up to about 2.6 MHz with increasing electric field, whereas the bandwidth on polyimide is not affected by the electric field. The results presented in this Chapter are published in Physical Chemistry Chemical Physics, with the same title as this Chapter has.[50] The graphical illustration for this investigation is shown in panel 7 of Figure 1.1.

Chapter 8 - "Summary and Outlook" summarizes all the results of this thesis and gives an outlook on how this research might be continued.

2

Photodetection with Functional Nanomaterials

2.1 Photodetection

Photodetectors convert incident optical signals into electronic signals and are classified into two major groups, one being thermal detectors and the other being photoelectric detectors.[51, 52] In thermal detectors, the optical energy is measured directly by observing a temperature rise because of the absorption of the energy of photons. This is a rather slow process and therefore not suited for the detection of fast optical signals.[53-55] Photoelectric detectors, on the other hand, are based on the photoelectric effect and, due to many different designs, offer a wide variety of working mechanisms that allow perfect tunability to the needs of the application, including fast-switching devices.

Due to their compact size, photodetectors based on the internal photoelectric effect are primarily used. In this process, an electron is excited to a higher energy level by the absorption of a photon and an electron-hole pair is formed. The photon energy required for this is[51, 52, 55-59]

$$h\nu \geq E_g \tag{1}$$

with the Planck's constant (h), the frequency of the incident radiation (ν) and the energy difference of the corresponding energy levels (E_g). When the semiconductor used as photodetector is excited with the optical band gap energy ($E_{g,opt}$), a Coulomb-bound electron-hole pair, a so-called exciton, is formed, cf. Figure 2.1a. The energy levels of the excitons are energetically below the conduction band (E_C) and the exciton binding energy (E_B) of the ground state exciton can be calculated according to:[60-65]

$$E_B = \frac{Me^4}{8h^2{\varepsilon_r}^2{\varepsilon_0}^2} \tag{2}$$

with the reduced mass of the electron-hole pair ($M = \frac{m_n m_p}{m_n + m_p}$, calculated via electron mass (m_n) and hole mass (m_p)), the elementary charge (e), the vacuum permittivity (ε_0), and the dielectric constant of the semiconductor (ε_r). This binding energy must first be expended to separate the exciton into free charge carriers ($E_g = E_{g,opt} + E_B$), which can then contribute to a photocurrent under the influence of an electric field. Strongly bound electron-hole pairs occur primarily in ionic crystals or organic molecular crystals. There, the exciton is typically located in the same unit cell and in the extreme case even on the same atom and is referred to as Frenkel exciton. In contrast, in inorganic semiconductors with high dielectric constants, the interaction is strongly screened and the electron-hole pair, also called Mott-Wannier exciton, is spatially extended.[60, 61] The average distance of the two bound charge carriers is the Bohr exciton (a_{Exc}) radius:[61, 62, 65]

$$a_{Exc} = \frac{\varepsilon_0 \varepsilon_r h^2}{\pi M e^2} \tag{3}$$

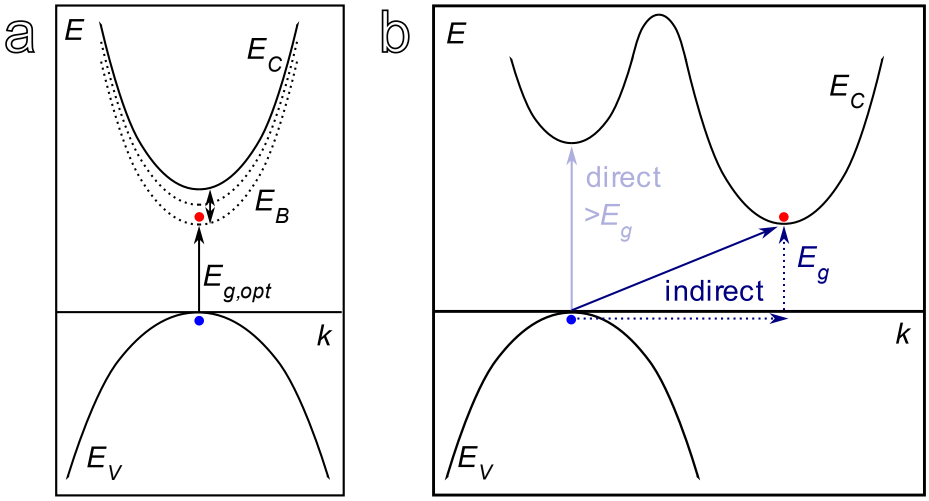

Figure 2.1. Energy levels of a) a direct band gap semiconductor with excitonic levels indicated by dotted lines, b) an indirect band gap semiconductor with both indirect (dark blue) and direct (light blue) transitions. Blue dot = hole, photogenerated in the valence band (E_V), red dot = electron, excited into excitonic levels or the conduction band (E_C).

Figure 2.1a shows a semiconductor with a direct band gap, such as GaAs or InP. The maximum of the valence band and the minimum of the conduction band are at the same position in reciprocal space (k-space) and an optical transition can take place solely due to the absorption of a photon. For a semiconductor with an indirect band gap, such as Si or Ge, the maximum of the valence band and the minimum of the conduction band are at different k-values, cf. Figure 2.1b. A photon alone cannot cause an excitation over the indirect band gap, since it has only a very small k-vector, and a phonon must be excited in addition. Momentum transfer with the lattice takes place, making this process less efficient than a direct transition. Direct transitions can be obtained in an indirect band gap semiconductor under excitation with higher energies.[57, 59, 63, 66] In addition, a distinction is made between intrinsic semiconductors, in which electrons are excited from valence to conduction band, and extrinsic ones, in which transitions occur that involve dopant states in the band gap.[55, 56, 59, 63]

2.1.1 Figures of Merit

The performance of photodetectors can be compared in varying aspects using figures of merit.

For many applications, the speed of response of a photodetector is essential. Optical communication systems, for example, operate at high rates of several tens of Gbits/s.[52, 67] Therefore, an extremely fast response of the photodetector utilized in an optical receiver in the range of picoseconds is required. With a sub-nanosecond response of the detector, the radiative recombination lifetime of a material can be measured in a time-resolved photoluminescence system.[68] Environmental detection using light detection and ranging, so-called LIDAR, is used among others for geodesy, seismology and in autonomous driving, requiring nanosecond response of the detectors.[69] Photodetectors with microsecond response time can be exploited for heart rate and blood oxygen saturation measurements.[70] Millisecond response, for example, is required for flame detection in vulnerable industrial facilities[71] and is sufficient for optical imaging[14, 72], since 10 – 60 frames/s are perceived by the eye as a continuous flow.

The rise time (t_{rise}) is a measure of the speed of response and is defined as the time it takes for the photocurrent to increase from 10 % to 90 % of its total value, and the fall time (t_{fall}), correspondingly the reverse, is defined as the time it takes to decrease from 90% to 10 %. They have to be distinguished from the response time or time constant (τ) which is the time it takes to reach $\left(1-\frac{1}{e}\right) \approx 63.2\,\%$ of the final value. The rise time can be calculated from the response time by considering a factor of 2.2.[73, 74] Another possibility to specify the speed of response is by giving the electrical bandwidth of the device. The 3 dB bandwidth is the frequency at which the photocurrent is reduced to $\sqrt{0.5} \approx 70.7\,\%$ of its steady state photocurrent value, corresponding to a reduction of the signal power to 50 %.[74, 75] The bandwidth can be estimated based on the photoresponse of the detector towards a delta-shaped laser pulse. By fast Fourier transformation (FFT) of the impulse response ($f(t)$) the power spectrum ($P(\omega)$) is given as[66, 76-83]

$$P(\omega) = |\mathrm{FFT}\big(f(t)\big)|^2 \tag{4}$$

and can be converted to the logarithmic scale using $\mathrm{dB} = 10log_{10}\frac{P(\omega)}{P_1}$, with the signal power under steady state conditions (P_1). The 3 dB bandwidth ($f_{3\ dB}$) is related to rise time and response time approximately via[55, 73-75, 84-86]

$$f_{3\ dB} = \frac{1}{2\pi\tau} = \frac{2.2}{2\pi t_{rise}} \approx \frac{0.35}{t_{rise}} \tag{5}$$

Both, the choice of active material with its corresponding charge carrier mobilities and the device geometry used, determine the speed of response of a photodetector. Therefore, a detailed description of the parameters that affect the rise time / bandwidth is provided in the following sections for each detector type.

Not every material can be used as absorber for every application as the range of the optical spectrum exploited in applications differs. The ultraviolet (UV) part of the spectrum is exploited among others for flame detection[87], in chemical analysis for example for toxin screening in food[88] and for monitoring of solar UV exposure[89]. Visible light communication requires high-speed photodetectors in the visible range (vis).[9, 10] In addition, vis image sensors are used in cameras[72, 90], for example for safety applications like blind spot warning systems for cars[91]. In the near infrared (NIR), telecommunication[8, 92], biomedical imaging[93] and night vision and surveillance[94, 95] are possible applications for photodetectors. Since photocarriers can only be generated when photons are absorbed, the wavelength dependent absorption coefficient ($\alpha(\lambda)$) of the active material in a photodetector is of major importance and defines its spectral response. The spectral response describes the magnitude of the photoresponse as a function of the wavelength of the illumination. Figures of merit used to display it are responsivity ($R(\lambda)$) and quantum efficiency ($\eta(\lambda)$).[51, 75]

The responsivity correlates the generated photocurrent (I_{Photo}) to the incident optical power (P_{opt}) and is defined as:[8, 51, 55, 74, 75, 84, 96]

$$R = \frac{I_{Photo}}{P_{opt}} \tag{6}$$

The external quantum efficiency (η) is defined as the ratio of the number of generated photocarriers (I_{Photo}/e) to the number of incident photons ($P_{opt}/h\nu$). It thus gives the probability that an incident photon will generate an electron-hole pair that contributes to the photocurrent and is closely related to the responsivity.[51, 52, 55, 66, 84, 97]

$$\eta = \frac{I_{Photo}h\nu}{eP_{opt}} = \frac{Rh\nu}{e} \tag{7}$$

Incident light can be reflected at the surface of a photodetector, reducing the number of photons that can enter the device and might be absorbed. Furthermore, if the absorption coefficient of the semiconductor is low at the wavelength of the incident illumination and the active semiconductor material is not sufficiently thick, only a small fraction of the incoming photons will be absorbed, and the rest will be transmitted. The internal quantum efficiency accounts for this by considering only the number of photons absorbed, not the number of incident photons.[51, 55, 66]

The long-wavelength cutoff of the spectral response is the wavelength corresponding to the band gap of the active material as with lower energies no electrons can be excited and $\alpha(\lambda)$ decreases sharply (if trap states in the band gap or excitation over the Schottky barrier in a metal-semiconductor diode, cf. Chapter 2.1.1.2, are neglected). For shorter wavelengths, $\alpha(\lambda)$ increases strongly and the spectral response generally matches the absorption spectrum of the active material.[19, 98-100] Since most photons are absorbed in the range of $1/\alpha(\lambda)$[66], i.e., near the surface of a photodetector, where charge carriers recombine rapidly due to a large number of recombination centers (which is especially pronounced for conventional 3D semiconductors), a short wavelength cutoff exists as well.[51, 52]

For many photodetectors, more than one charge carrier can be generated in the circuit for only one absorbed photon. This is expressed by gain, which specifies how many charge carriers per generated electron-hole pair contribute to the current flow.[51] The current due to the absorption of photons is named primary photocurrent, whereas the increase of photocurrent due to gain mechanisms is called secondary photocurrent.[52, 73] Gain plays a major role in photoconductors and phototransistors and will be discussed in more detail in the associated Chapters 2.1.2.1 and 2.1.2.3.

The responsivity does not consider the size of a photodetector. The area-independent figure of merit that allows direct comparison of different detectors is the so-called specific detectivity (D^*):[75, 96, 101, 102]

$$D^* = \frac{R\sqrt{Af}}{\delta I_{noise}} \tag{8}$$

with the current noise spectral density (δI_{noise}), the detector area (A) and the electrical bandwidth (f). The unit [$\mathrm{cm}\sqrt{\mathrm{Hz}}/\mathrm{W}$] is also known as Jones.

A signal-to-noise ratio of one is the lower detection limit of a photodetector. It indicates that incident radiation with optical powers equal to, or lower than this value cannot be measured as the generated signal is equal to, or lower than the noise current. The corresponding optical power, the Noise Equivalent Power (NEP), can be calculated according to:[55, 74, 75, 84, 96, 102]

$$NEP = \frac{\delta I_{noise}}{R} \tag{9}$$

The range with linear response of the photodetector towards the incident optical power is called linear dynamic range.[51]

2.1.2 Types of Photodetectors

There are many types of photodetectors that show significant differences in their performance and varying figures of merit are optimized. In the following, the most common types, namely photoconductors, photodiodes, and phototransistors, are described in more detail with focus on their speed of response.

2.1.2.1 Photoconductor

A photoconductor is a semiconductor with ohmic electrical contacts whose conductivity increases significantly under illumination due to the generation of additional free charge carriers, cf. Figure 2.2a. The conductivity (σ) can be calculated according to[52, 57, 61, 63, 75, 92]

$$\sigma = e(\mu_n n + \mu_p p) \tag{10}$$

with the mobilities of electrons (μ_n) and holes (μ_p) and the corresponding charge carrier densities (n, p). If z electron-hole pairs are photogenerated per second, the additional free electron / hole densities (Δn / Δp) are:[63]

$$\Delta n = z\tau_n \tag{11a}$$
$$\Delta p = z\tau_p \tag{11b}$$

with the free lifetime of electrons and holes (τ_n, τ_p), respectively, that describe the time during which the respective charge carrier is a free, mobile carrier in the corresponding band. By applying an electric field, mobile charge carriers can be swept to the electrodes and contribute to the photocurrent in the meantime.[58, 74] The photoconductivity ($\Delta\sigma$) is[63]

$$\Delta\sigma = ze(\mu_n \tau_n + \mu_p \tau_p) \tag{12}$$

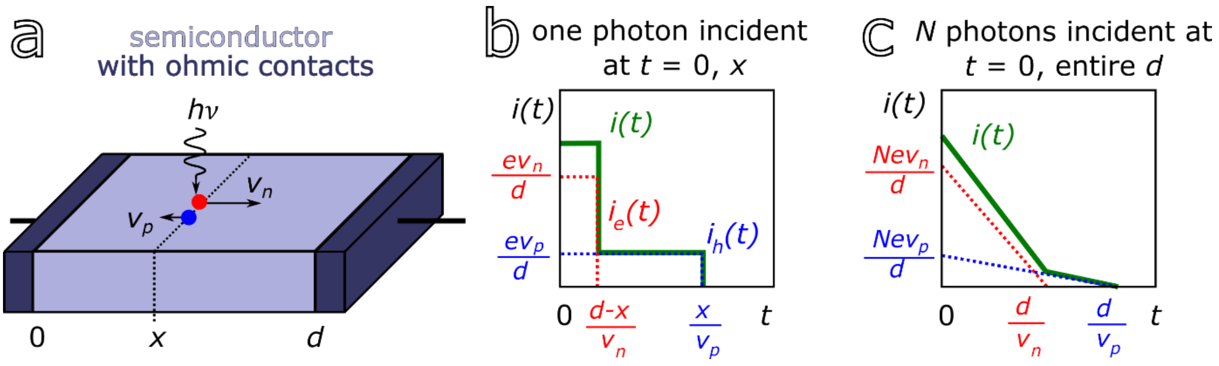

Figure 2.2. a) Schematic of a photoconductor, with the velocity of electrons being larger than the velocity of holes ($v_n > v_p$). b) Transient photocurrent with one photon being absorbed at position x at time $t = 0$, c) Transient photocurrent when the entire photoconductor length is illuminated at $t = 0$. Electron and electron current depicted in red, hole and hole current depicted in blue, total current shown in green. Figure similar to Bowers and Wey.[103]

The speed of response of a photoconductor can be limited by several factors. The time required for the charge carriers to reach the electrodes, the transit time (t_{trans}), is an important aspect, not only for photoconductors but for all photodetectors. If an exciton is generated at a specific position (x) in the semiconductor with length (d), the charge carriers get separated by the applied electric field ($\mathcal{E}$) and the mobile carriers are swept towards the electrodes, cf. Figure 2.2. The current ($i(t)$) is defined by Ramo's theorem according to[51, 104]

$$i(t) = -\frac{e}{d}v(t) \tag{13}$$

with the electric charge being moved at the velocity ($v(t)$). Under the assumption that charge carriers move with constant velocity (hole velocity (v_p) and electron velocity (v_n)), the hole and the electron need the times[103]

$$\frac{x}{v_p} \tag{14a}$$

$$\frac{d-x}{v_n} \tag{14b}$$

respectively, to reach the electrodes, cf. Figure 2.2b. If the whole detector is illuminated, electron-hole pairs are generated across the entire channel length, resulting in both holes and electrons being collected directly at their corresponding electrodes and having to travel the entire length (d) when generated near the opposing electrode, cf. Figure 2.2c. This gives the transit time:[52, 55, 58, 63, 85, 105]

$$t_{trans,i} = \frac{d}{v_i(t)} = \frac{d}{\mu_i \mathcal{E}} = \frac{d^2}{\mu_i U} \tag{15}$$

for the corresponding charge carriers ($i = n, p$) under the applied voltage (U).

Usually, mobilities of electrons and holes differ, resulting in a shorter transit time for the majority carrier (electrons in Figure 2.2). The photogenerated majority carrier is extracted by the electrode and due to charge neutrality, another majority carrier is replenished into the photoconductor from the opposite ohmic electrode to transit the device. The minority carrier can also be trapped in a localized state near the band edge. There, it is in thermal equilibrium with the band and can be reexcited by $k_B T$, with the Boltzmann constant (k_B) at the temperature (T). The process of majority carrier transit continues until majority and minority carrier recombine.[51, 52, 55, 56, 58] Direct charge carrier recombination of free electrons and free holes usually takes place only at high charge carrier densities. Otherwise, recombination of a free charge carrier with a carrier located in a recombination center dominates, the so-called Shockley-Read-Hall recombination. Recombination centers are localized states in the band gap, which are not in thermal equilibrium with the bands as trap states but are deep states and therefore dominated by kinetic recombination processes. The energy of the transition can be dissipated either by the emission of a photon, by transfer to phonons, or by transfer to a third charge carrier in an Auger recombination.[55, 56, 59, 63, 73]

The obtained gain depends directly on the majority carrier transit time and the minority carrier recombination time or lifetime (t_{life}), which is defined as the time the carrier is excited including the time spent in traps (thus, is usually longer than the free carrier lifetime). It ranges from 10^{-13} s up to several seconds depending on the semiconductor material and its degree of doping.[51] The gain can be calculated via:[15, 36, 51-53, 92, 103, 106]

$$G = \frac{t_{life}}{t_{trans}} \tag{16}$$

For fast photodetectors, the carrier lifetime must be short, giving rise to a trade-off between the response speed and gain. However, if different trap states of a material and their associated time constants are studied, the material composition of the detector can be optimized to selectively induce fast, shallow trap states, while avoiding all others through adapted fabrication processes. This allows gain to be preserved while speed is improved.[13-16, 107] In a special case of photoconduction, when many trap states are present in the material, the trapped charge carriers can modulate the electronic properties of the photoconductor channel as an additional gate. This is called photogating.[108, 109]

Another limitation for the speed of a photodetector is caused by the resistance (R) and the capacitance (C) of the detector and its adjacent circuit.[51] The so-called RC time defines an exponential relaxation process of the device in response to the (dis-)charging because of the illumination. The capacitance of a photoconductor, as shown in Figure 2.2a, can be calculated using the parallel-plate capacitor model with[58, 61]

$$C = \frac{\varepsilon_r \varepsilon_0 A}{d} \tag{17}$$

with detector area (A). Parasitic capacitances of the circuitry must be considered for the RC time calculation as well. Likewise, regarding the resistance, both the resistance of the detector and the load resistance of the circuitry are crucial.[92, 97, 101] For an RC limited photodetector, its 3 dB bandwidth ($f_{3dB,RC}$) can be calculated according to[8, 27, 52, 101, 103]

$$f_{3dB,RC} = \frac{1}{2\pi RC} \tag{18}$$

The slowest of these three time constants –transit time, lifetime or RC time – limits the speed of a photoconductor. While the transit time can be reduced by shortening the detector length, the capacity, thus the RC time, is increased at the same time. A simultaneous optimization of all time constants is not possible, and the optimal geometry must be found in the trade-off between transit time and RC time. Since most photoconductors exhibit internal gain, they are severely limited in speed and therefore generally cannot be used for high-speed applications.

2.1.2.2 Photodiode

In contrast to a photoconductor, a photodiode has a built-in electric field that separates the photogenerated charge carriers and accelerates them to the corresponding electrodes, while no external field needs to be applied. This is due to the diode structure with a junction formed in the device that makes these detectors typically faster than photoconductors. Photodiodes include p-n and p-i-n diodes, metal-semiconductor diodes, also called Schottky diodes, and metal-semiconductor-metal (MSM) diodes.[52, 55, 74]

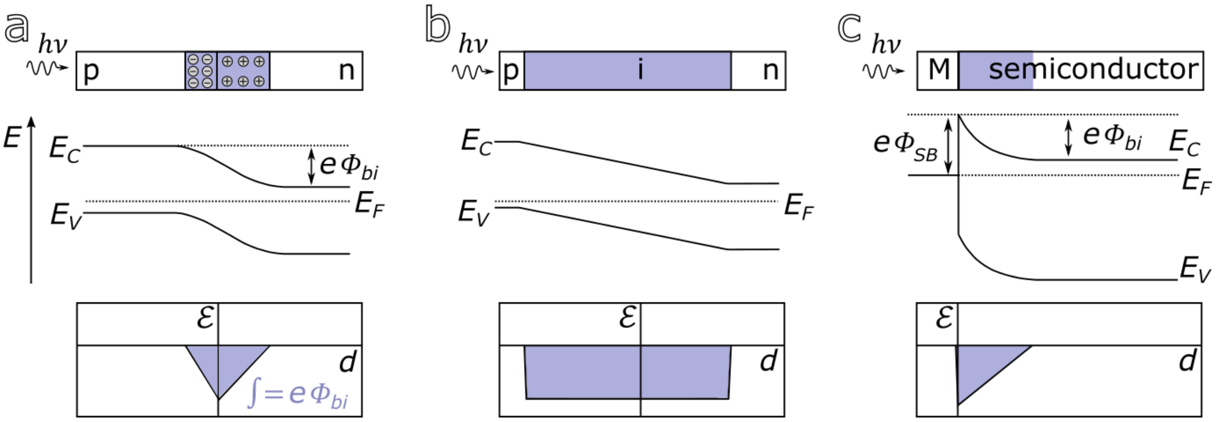

Figure 2.3. Photodiode junctions: schematic illustration, energy band diagrams and electric-field distributions (from top to bottom). a) p-n junction, b) p-i-n junction, c) metal (M) - semiconductor junction. With valence band (E_V), conduction band (E_C), Fermi level (E_F), built-in potential (Φ_{bi}), Schottky barrier (Φ_{SB}), electric field ($\mathcal{E}$), length of the device (d) and the depletion region shown in blue. Incident illumination ($h\nu$) for use of the junctions in photodetection.

The junctions exploited in a photodiode are schematically shown in Figure 2.3. At a p-n junction, an abrupt change in dopant concentration is present, switching from acceptor (p-type) to donor (n-type) impurities. Due to the concentration gradient, free electrons of the n-type semiconductor diffuse into the p-type semiconductor where they recombine with free holes, and vice versa. At thermal equilibrium, when the Fermi level is constant across the junction, there are no more free charge carriers in the junction region and the dopant atoms are charged, the acceptors negative and the donors positive. This gives rise to a so-called depletion or space-charge region with an electric field ($\mathcal{E}$) and a built-in potential (Φ_{bi}). The width of the space charge region depends on the doping concentrations of the p/n-type regions and extends the farther into the respective side the lower it is doped (as for the n-side of Figure 2.3a).[52, 55, 56, 58, 59, 62, 63, 84, 110] Therefore, if an undoped, intrinsic (i) region is embedded between p- and n-type regions in a p-i-n diode, the depletion region extends over the entire long intrinsic region, see Figure 2.3b.[51, 57, 59, 66, 101] The width of the depletion region is further modified by an applied voltage. A reverse bias extends the depletion region and enhances the electric field in the device, as it adds up to the built-in voltage, while a forward bias shortens it and decreases the electric field.[52, 59, 84]

A rectifying contact between the metal electrode and the semiconductor can be explained by a built-in Schottky barrier at the metal-semiconductor interface. Figure 2.3c shows the situation for a metal in contact with a n-type semiconductor. The electron affinity of a semiconductor (χ) is typically lower than the work function of a metal (Φ_m). When brought into contact, free electrons flow from the n-type semiconductor to the metal until equilibrium is reached (Fermi levels (E_F) lined up). This forms a depletion region with positively charged donor impurities in the semiconductor. As with a p-(i-)n diode, the dopant concentration and the applied voltage affect the width of the depletion region. The Schottky barrier height (Φ_{SB}), resulting at the metal-semiconductor interface, can be approximated using[52, 55, 111]

$$e\Phi_{SB} = e\Phi_m - e\chi \tag{19}$$

For a p-type semiconductor, a Schottky barrier forms when the work function of the metal is smaller than the work function of the semiconductor. This behavior contrasts with an ohmic contact, which occurs when the work function of the metal is smaller (larger) than the work function of the n-type (p-type) semiconductor. There are no potential barriers at the interface and electrons (holes) can pass freely from one region to the other. Therefore, ohmic contacts are used as connections to photodetectors, as already mentioned for photoconductors.[57, 63, 110] A MSM diode consists of two Schottky diodes which are connected back-to-back, which always results in one of the diodes being reverse-biased and ensures that the dark current in the system is very low.[112]

Large deviations from the calculated Schottky barrier height without a correlation to the metal work function may be encountered, if many interface states with energy levels within the band gap are present at the semiconductor surface.[113] Due to these surface states, a band bending results at the semiconductor surface, which, even after contact with the metal electrode, depends more strongly on the position and amount of surface states than on the work function of the metal.[63] This results in the so-called Fermi level pinning, that emerges energetically at the position of the highest surface state density.

The speed of response of a photodiode depends on both the RC time, emerging from resistance and capacitance of the photodiode and the adjacent circuit, and on the transit time of the charge carriers, comparable to the situation in a photoconductor.[51, 53, 86, 92, 97, 101, 105] The RC-limited bandwidth can be determined by Formula (18), in the same way as for a photoconductor. The transit time might be composed of two different time components, cf. Figure 2.4.

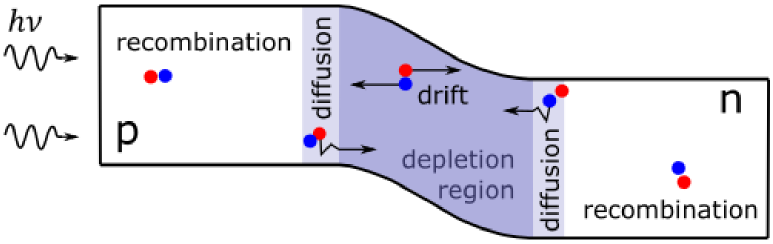

Figure 2.4. Drift and diffusion contributions occur in different areas of a photodiode, exemplarily shown for a p-n diode. Recombination losses arise far away from the junction.

In the depletion region, charge carriers drift due to the built-in electric field and the drift time (t_{drift}) can be calculated like the transit time in a photoconductor according to Formula (15), assuming a constant electric field as for p-i-n diodes.[56, 85, 114] If the photodiode is transit time-limited, its bandwidth is usually estimated approximately using[55, 66, 92, 103, 115]

$$f_{trans} \cong \frac{0.55}{t_{trans}} \tag{20a}$$

This Formula is valid if charge carriers are photogenerated uniformly over the entire depletion region and if transit times for electrons and holes are the same. For different transit times, if, e.g., holes take twice as long as electrons ($t_{trans,n}$), the bandwidth is reduced to approximately[55, 116]

$$f_{trans} \cong \frac{0.34}{t_{trans,n}} \tag{20b}$$

With a high absorption coefficient of the semiconductor at the wavelength of the incident illumination, charge carriers are generated only at the edge of the depletion region. On average, they take longer to traverse than if they are generated uniformly over the entire space-charge region. Therefore, the bandwidth is reduced in comparison to Formula (20a) to[52, 55, 66, 103, 105]

$$f_{trans} \cong \frac{0.44}{t_{trans}} \tag{20c}$$

Outside the depletion region, charge carriers move by much slower diffusion, due to the concentration gradient of the carriers.[51, 56, 62, 97, 117] The diffusion coefficient (D_i) determines how long charge carriers need to travel the diffusion length (l):[62, 63, 66]

$$t_{diff,i} = \frac{l^2}{D_i} \tag{21}$$

with the slower carrier ($i = n, p$) limiting the speed of the diffusion contributions. If charge carriers reach the depletion region before they recombine, which are those generated by less than one diffusion length away from the depletion region, they drift along the electric field. Hence, they contribute to the photocurrent and slow down the device as they generate a slow tail in the photoresponse, reducing the bandwidth accordingly.[55, 103] Shortening the field-free region in the photodiode (l in Formula (21)) to lengths smaller than the diffusion length or increasing the diffusion coefficient by enhancing the carrier mobility (according to $D_i = \frac{\mu_i k_B T}{e}$)[55-57, 62] reduces this limiting component and accelerates the diode.[55, 118]

A photodiode cannot be further slowed down by gain (under moderate fields, neglecting avalanche multiplication), as it can happen with photoconductors, since all generated photocarriers are swept by the built-in electric field towards the electrodes[57] and no unoccupied doping impurity trap states are available in the depletion region. The gain of photodiodes is one, at most.[52] Moreover, the charge carrier density is usually low enough to avoid recombination in the depletion region.[97]

Consequently, the rise time of a photodiode is composed of three time components: RC time, drift time and diffusion time. The slowest component limits the speed of the response, and the rise time is usually estimated using[84, 85, 101, 117]

$$t_{rise} = \sqrt{t_{diff}^2 + t_{drift}^2 + (2.2\tau_{RC})^2} \tag{22}$$

The RC time constant is defined by an exponential relaxation process, thus, for its incorporation into the 10 % – 90 % rise time, a factor of 2.2 must be considered (cf. Chapter 2.1.1, rise time vs response time). For the optimization of high-speed photodiodes, the diffusion of charge carriers should be avoided by designing the diode in such a way that charge carriers are generated only in the depletion region. The drift time is reduced by decreasing the channel length, but, at the same time, this increases the RC time by increasing the capacitance. Thus, comparable to photoconductors, an overall optimization must be achieved in the trade-off between drift time and RC time. For a fully depleted PbS QD photodiode, the trade-off between RC time and transit time on varying the photoactive layer thickness was demonstrated and the rise time towards square pulse illumination could be minimized.[114]

Three modes of operation for photodiodes exist: reverse-biased, also called photoconductive, open circuit, also called photovoltaic, and short circuit, cf. Figure 2.5. The speed of a photodiode is influenced due to the different effects of the operation modes towards the three time components.[51, 52, 55, 84]

For high-speed applications, a photodiode is usually operated in the photoconductive mode where it is reverse-biased. In this case, the depletion region is enhanced, the junction capacitance is reduced (cf. Formula (17)), and thus the RC time. At the same time, the drift velocity is accelerated due to the enhanced field. If the whole diode is depleted, slow diffusion is avoided and only drift processes and RC time play a role. The load resistor influences the operation points of the reverse-biased diode according to the load line. Very high reverse bias causes impact ionization of charge carriers, and gain due to avalanche multiplication occurs, but this reduces the speed of the diode and is not discussed further in this work. In the photovoltaic mode, which is typically exploited in solar cells, the generated photocarriers enhance the photovoltage across the diode with increasing photon flux (Φ). Usually, the depletion region does not extend over the entire active area of the photodiode in this mode of operation, so the diffusion time of charge carriers limits its speed. Under short circuit conditions, only the photocurrent is present in the system.

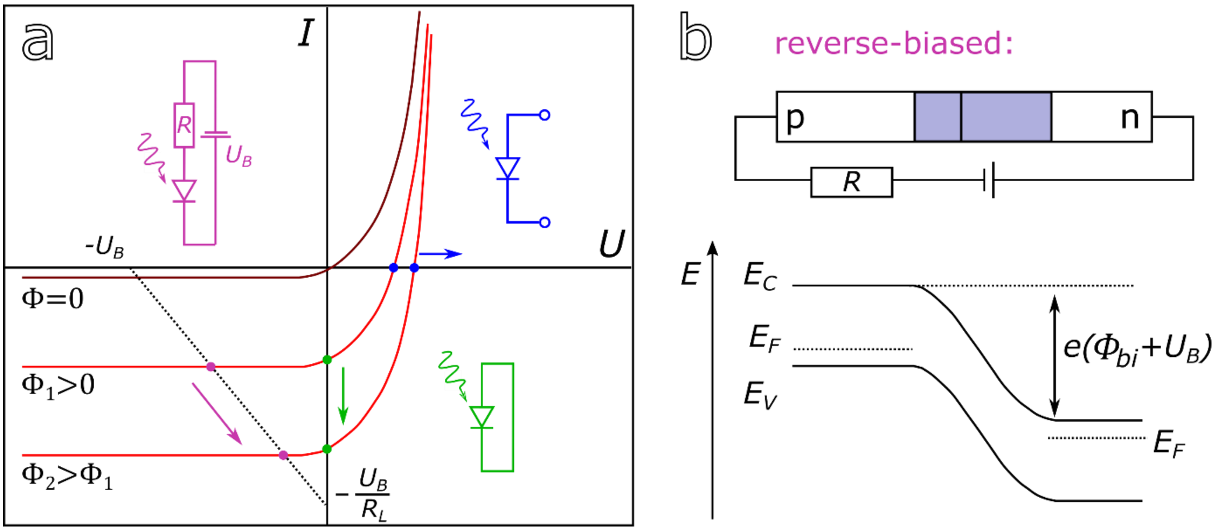

Figure 2.5. a) Photodiode modes of operation. Photoconductive mode shown in magenta, with the load line (dotted), photovoltaic mode show in blue, and short circuit shown in green. Photon flux (Φ), reverse bias (U_B), load resistance (R_L) of load resistor (R). Figure similar to Saleh and Teich.[51] b) Reverse-biased p-n junction.

Advantages of p-i-n diodes over p-n diodes.

Drift of charge carriers occurs only in areas with an electric field, i.e., in the depletion region. For p-n diodes, the depletion region is short and the associated electric field peaks directly at the interface, dropping linearly to both sides, cf. Figure 2.3a. Consequently, the drift velocity in the depletion region varies with distance and much of the incident illumination is absorbed outside the depletion region, causing diffusion of charge carriers to limit the speed of the diode.

For p-i-n diodes, on the contrary, the electric field extends over the large intrinsic region. Most photocarriers are generated in the extended depletion region, where they experience a consistently high drift velocity due to the (approximately) constant high field. Depending on the selected thickness of the intrinsic region compared to the absorption depth of the illumination $1/\alpha(\lambda)$, the slow diffusion contribution of photocarriers in the underlying material can be avoided altogether. The junction capacitance is smaller with larger depletion layer thickness, thus the RC time is reduced in p-i-n diodes as well.[51, 52, 55, 59, 101] These factors accelerate a p-i-n diode considerably compared to a p-n diode, even though the charge carriers must travel a larger distance in the enlarged depletion region.

In addition, by matching the i-region to the absorption depth of the incident illumination, the quantum efficiency of a p-i-n diode is optimized. Generation of charge carriers more than one diffusion length away from the space charge region, thus, generation of carriers that cannot contribute to the photocurrent, can be avoided.[52]

Advantages of heterostructure p-i-n over homostructure p-i-n diodes.

Photodiodes are usually constructed vertically. This causes part of the incident light being absorbed in the topmost, field-free, highly doped layer. Since charge carriers in this area slow down the speed of the photodiode due to diffusion, the top layer is made as thin as possible to minimize this effect. It must not be too thin, otherwise its sheet resistance (which is inversely proportional to the sheet thickness), and thus the RC time, will be strongly enhanced.[51, 92, 119] To reduce the diffusion limitation, the often differing diffusion coefficients of electrons and holes can be exploited, as for example in GaAs (D_n~$207\ \mathrm{cm^2/s} \gg D_p$~$11\ \mathrm{cm^2/s}$)[120]. When p-doping is chosen as top layer, the faster electron diffusion limits the speed of the device and slower hole diffusion contribution is avoided.

Diffusion processes can be eliminated completely, however, if a non-absorbing so-called window layer is selected as the top layer.[55, 56, 92, 97] This is utilized in heterostructure diodes where the high-field depletion region is embedded in a material with larger band gap and the diode response is accelerated, as for example shown for a AlGaN/GaN diode.[121] However, energy band offsets occur at the heterointerface that can inhibit charge transport, cf. Figure 2.6.[52, 59, 62, 103, 110] The accumulation of charge carriers at the created barrier of the heterointerface is called charge pile-up and can lead to slow contributions to a diode response, as for example with InGaAs/InP[105, 122, 123] heterojunctions. This effect must be reduced using laborious graded junctions.

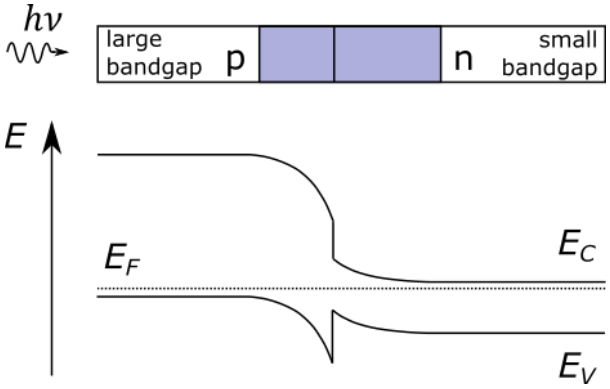

Figure 2.6. Energy band diagram of a heterostructure p-n junction with band offsets.

Some semiconductors are unipolar materials that cannot be doped easily both p- and n-type. This is the case for II-VI compound semiconductors, where, for example, p-type doping of CdS is difficult to achieve[124], whereas for ZnTe n-type doping is challenging.[125] Therefore, these materials are more easily integrated into hetero- than homostructure devices.

In addition, a window layer enhances the responsivity, especially for UV/Vis detectors having high absorption coefficients, since radiation losses due to absorption in the front layer and recombination losses at surface states are avoided.[51, 66, 92, 121]

Advantages of Schottky diodes over p-(i-)n diodes.

Another way to circumvent diffusion processes occurring in the highly doped front layer of p-(i-)n diodes is to utilize a metal / semiconductor junction instead.[51, 52, 55, 56, 86, 103] The depletion region is located directly at the surface of the semiconductor, which is especially useful for UV/Vis detection, where high absorption coefficients limit the absorption depth of photons significantly. Even though thin metal layers are needed for (semi-)transparency, this does not increase the series resistance of the diode noticeably as the resistances of metals are low. Moreover, as with heterojunction diodes, Schottky junctions can be used to integrate unipolar materials into photodiodes, which are difficult to dope both p- and n-type.

In addition to the usual excitation of charge carriers in the semiconductor across the band gap, cf. Formula (1), a Schottky diode can furthermore be operated in a second mode. In the so-called internal photoemission lower photon energies are exploited. For $e\Phi_B < h\nu < E_g$, electrons are photoexcited in the metal electrode, and those with momentum towards the semiconductor can overcome the Schottky barrier, generating a photocurrent. This allows long wavelength detectors to be fabricated without relying on low band gap semiconductors and is one possibility to measure the Schottky barrier.[52, 55, 56, 126, 127]

Advantages of MSM diodes

Figure 2.7. a) MSM interdigitated electrode geometry with b) electric field lines, device shown from the side.

In order to make the coupling of the incident illumination to the photodetector as simple and efficient as possible, large detector areas are advantageous. For vertical p-(i-)n or Schottky diodes, this enhances the capacitance, cf. Formula (17), and slows down the detector. An interdigitated electrode geometry is often employed in MSM diodes, resulting in lateral geometries, cf. Figure 2.7a. These devices can be integrated easily into existing field-effect transistor technology and, compared to a p-(i-)n or Schottky diode of comparable size and quantum efficiency, the capacitance is reduced by about a factor two to five what reduces the RC time of the device.[28, 52, 97, 112] The capacitance can be calculated via[116]

$$C = L(N-1)\varepsilon_0(1+\varepsilon_r)\frac{K(k)}{K(k')} \tag{23a}$$

with the electrode finger length (L), the number of electrode fingers (N), and the complete elliptical integral of first kind (K). With

$$k = \cos\left(\frac{\pi}{2}\left(1-\frac{w}{w+g}\right)\right) \tag{23b}$$

$$k' = \sqrt{1-k^2} \tag{23c}$$

and the width of the electrode fingers (w) and the channel length (g). With increasing channel length, the capacitance is reduced, but the transit time is enhanced, as for vertical photodetectors. A minimal finger width reduces the capacitance, but at the same time, the resistance of nanometer thin electrodes is significantly enhanced compared to bulk values due to an increase in collisions of charge carriers and the metal boundary.[128] Therefore, to optimize the speed of response of a MSM detector, an optimal finger spacing, finger number and finger width for both square and circular device geometries can be determined.[27, 28, 76, 116] Furthermore, the thickness of the active material deposited on top of the interdigitated electrodes must be limited to reduce contributions from photocarriers generated far from the electrodes, having long drift times due to the low electric field deep in the material and the large drift distances, cf. Figure 2.7b.[76, 79, 112]

Despite the use of a diode structure, gain can be observed in MSM detectors.[52, 97, 112] It is ascribed to trapped charge carriers close to the electrodes, that vary the electrostatic potential and enhance carrier tunneling into the semiconductor.[52, 92, 129]

2.1.2.3 Phototransistor

If two p-n junctions are connected back-to-back, a bipolar phototransistor results and gain is obtained, in contrast to a single p-n junction. Two configurations are possible, n-p-n or p-n-p, and the three regions are named emitter, base, and collector.

Under illumination, photocarriers are generated at the reverse-biased base-collector junction and produce a primary photocurrent due to the photogenerated electrons being transported towards the collector electrode in a n-p-n transistor, cf. Figure 2.8a. Both, drift within the depletion region and diffusion of electrons generated up to a diffusion length away from the depletion region, take place. Photogenerated holes are blocked at the emitter-base transition and accumulate in the base, lowering the emitter-base potential barrier. Enhanced injection of electrons from the emitter into the base occurs and induces the secondary photocurrent, provided that the electron transit time through the base is shorter than the recombination time. This can be achieved with a sufficiently thin base region shorter than the diffusion length of the electrons. Moreover, in case of homojunctions, a high emitter and low base doping concentration is required, while for heterojunctions, a large band gap difference using a wide band gap emitter is sufficient.[55, 63, 130] The secondary photocurrent prevails as long as the holes accumulate in the base. If they leave the base by diffusion or recombination, the potential barrier increases again and the secondary photocurrent ceases.[63]

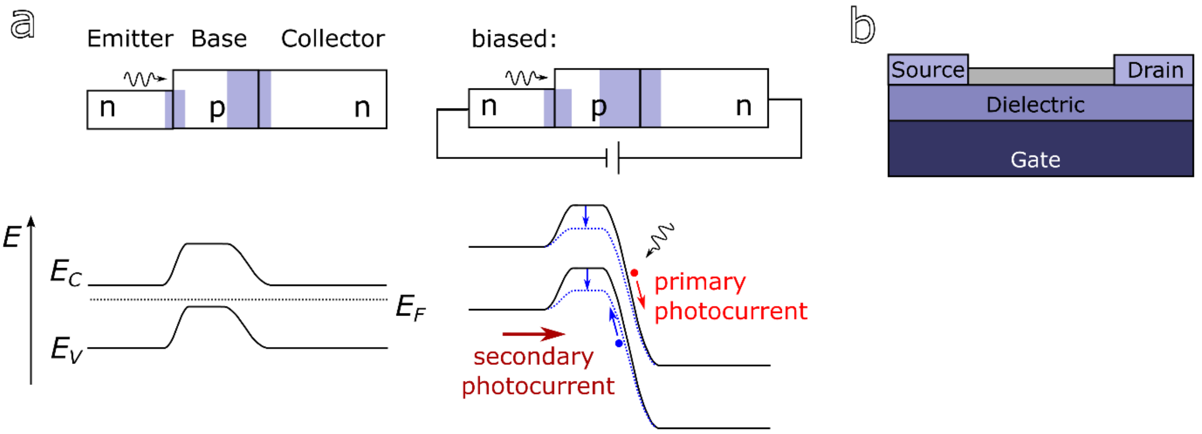

Figure 2.8. Phototransistor. a) homojunction bipolar transistor, unbiased and under operating conditions. Red: photogenerated electron, primary photocurrent; blue: photogenerated hole and hole accumulation induced lowering of the emitter-base potential barrier. Brown: secondary photocurrent. b) photo-field effect transistor.

The speed of the phototransistor can be determined according to:[52, 55, 130]

$$\tau = \beta_0 \left(\frac{k_B T}{e I_E} (C_E + C_C) + R_L C_C + \tau_B \right) \tag{24}$$

The first two terms describe the charging times of the emitter-base and collector-base junctions with their corresponding capacitances (emitter-base junction capacitance (C_E) and the collector-base junction capacitance (C_C)), the load resistance of the adjacent circuit (R_L) and the current gain (β_0). Usually, this is the limiting factor for a phototransistor. As it can be seen, the response time depends on the emitter current (I_E), and by that, on the power of the incident illumination. The higher the current under illumination, the faster the transistor. The second contribution to the speed of the phototransistor is the time constant of the minority carrier transit through the base (τ_B). For many conventional semiconductors (like Ge, Si, GaN, GaAs, InP, …), electrons have higher mobilities than holes[63], hence, the n-p-n configuration with the current being conducted by electrons in the base is faster than the p-n-p configuration, which is limited by slow hole transport.[131]

A second device geometry is often referred to as a phototransistor and is shown in Figure 2.8b. The photoactive material is provided with source and drain electrodes and is deposited on a thin insulating layer on top of a third electrode, the gate electrode. The semiconductor in the channel is therefore controlled not only by the incident light but also electronically by the gate.[17, 20, 21, 23, 96, 111, 132-137] It is therefore comparable to a photoconductor or a MSM photodiode (depending on the contact of the semiconductor with the electrodes) but with an additional electronic possibility to tune the active material.

2.1.3 Measurement Techniques

Commonly used test signals for (opto-)electronic devices are a delta function (impulse response), a Heaviside step function (square pulse response) and a sinusoidal function. In this work, the first two optical excitations are used and are shortly introduced in this Chapter.

2.1.3.1 Response towards Impulse Illumination

The transient photocurrent response caused by impulse illumination usually shows an initial exponential decay. This is attributed to charge carrier recombination and initial trapping.[138] A slower decay follows which obeys a power law behavior[25, 139-144], depicted in Figure 2.9a. Sometimes a kink can be observed in the slow tail when the log-log plot is presented.[145-147] The slow power law tail can be attributed to a large number of trap states present in highly disordered crystals or amorphous solids and is explained within the multiple trapping and release model.[139, 146, 148-152]

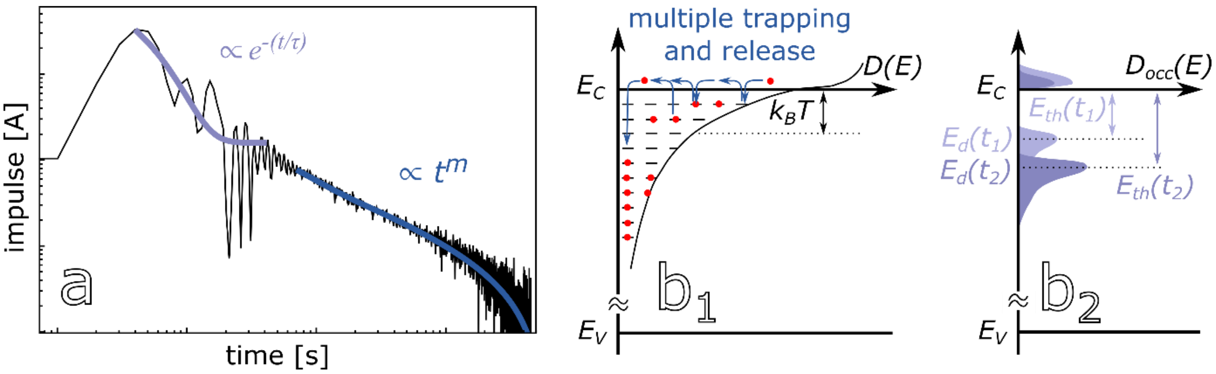

Figure 2.9. a) Impulse photocurrent with an initial exponential decay ($\propto e^{-\frac{t}{\tau}}$), followed by slow power law behavior (t^m). b) Multiple trapping and release model for electron conduction (b₁) with the schematic of the carrier distribution and the evaluation of the thermalization energy (b₂). Adapted from Adhikari et al.[139] with the permission of AIP Publishing, 2018, and modified. Valence band (E_V), conduction band (E_C), density of states $D(E)$, occupation density ($D_{occ}(E)$), thermalization energy ($E_{th}(t)$ with $t_2 > t_1$).

Charge carriers are transported in the corresponding band by an electric field but can be trapped quickly in localized states within the band gap, where they are immobile and cannot contribute to the photocurrent, cf. Figure 2.9b₁ for electron conduction. Assuming that all trap states have the same capture cross section, initially, all traps are occupied uniformly. At a time delay (t_1) after the trapping time, there are two groups of states. Charge carriers from shallow trap states are reexcited into the band by k_BT, thus, those trap states are occupied according to a Boltzmann distribution and are thermalized. Carriers in deep trap states have not yet been excited thermally but are constantly occupied at the time delay (t_1). From the band, mobile charge carriers can then be recaptured and since this is again equally likely to be distributed across all trap states, the deep trap states become occupied more and more over time (delay $t_2 > t_1$). The occupation density of the localized states in the band gap can be calculated via the product of the density of trap states and the time-dependent mean occupation number. With an exponentially decreasing density of trap states into the band gap, a charge carrier package results and the maximum occupation density is at the time-dependent demarcation energy ($E_d(t)$). It separates thermalized and non-thermalized carriers and the thermalization energy ($E_{th}(t)$, for electron trap states: $E_{th}(t) = E_C - E_d(t)$, cf. Figure 2.9b₂) increases with time according to[148, 151]

$$E_{th}(t) = k_BTln(\upsilon t) \tag{25}$$

with the attempt-to-escape frequency (υ). Therefore, the package moves deeper into the gap with time. This stops when steady state is reached, where the mean occupation density follows the Fermi distribution and the occupation density of the deep levels reaches one, thus, the carrier package cannot move lower in energy.[149, 152]

For an exponentially decreasing density of trap states into the band gap, the photocurrent decreases due to the incremental filling of deep trap states according to[145, 146, 149-151, 153]

$$I_{Photo} \propto t^{-1+\alpha} \tag{26a}$$

$$\alpha = \frac{k_B T}{E_U} \tag{26b}$$

with the energy (E_U) describing the exponential trap distribution. An exponential decrease of the absorption coefficient below the band gap energy has already been found in many semiconductors with both indirect[154] and direct[155] band gap and is usually attributed to such a decreasing density of states extending into the band gap.[154, 156] The corresponding energy, the measure of the width of the absorption edge, is named Urbach energy (E_U).

On longer timescales, when the photogenerated charge carriers transit the entire channel length of the photodetectors and are extracted at an blocking electrode (i.e., without replenishment of an additional charge carrier into the device by the other electrode), a kink in photocurrent is visible as the power law behavior changes towards[145, 149, 150]

$$I_{Photo} \propto t^{-1-\alpha} \tag{27}$$

This formula also applies if, instead of carrier transit, monomolecular recombination takes place.[146, 149] Monomolecular recombination occurs when the amount of initially generated charge carriers is small compared to the number of trap states (e.g., electron trap states), so that only a small amount of free minority carriers (electrons) is available for recombination and limits it. Thus, the trapped charge carrier package moves deeper into the band gap due to multiple trapping and release, cf. Formula (26), until the carriers are either removed by the electrode (t_{trans}) or recombine ($t_{life,mono}$), cf. Formula (27) (and before steady state is reached).

If, on the other hand, the amount of initially generated charge carriers is high in comparison to the number of trap states, then both carrier types are equally available and influence the recombination. This is called bimolecular recombination and, as soon as it starts, the photocurrent follows[149]

$$I_{Photo} \propto t^{-1} \tag{28}$$

until the charge carrier concentration is strongly reduced and the course of the photocurrent changes to the monomolecular case according to Formula (27).

2.1.3.2 Response towards Square Pulse Illumination

The square pulse photoresponse is often used to verify that the investigated photodetector offers a fast, repeatable, and long-time stable switching behavior.[23, 32, 38, 44, 157-163] Rise and fall times are extracted from the measurements[18, 44, 100, 114, 158, 159, 164] or the data is fitted with an exponential function to evaluate the response time[107, 137, 160, 165] or with a multiple exponential decay if fast and slow components are present.[26, 42, 45, 102, 163, 166] If persistent photoconductivity is observed, a stretched exponential relation is displayed but the physical significance of the stretching exponent is still unclear.[167]

Square pulse illumination is regularly used to investigate if variations in the photodetector fabrication speed them up, especially with regard to a tuning of the active material[13-15, 107, 164, 165, 168, 169] but also with regard to the choice of metal electrodes[20, 24, 26] or the device geometry[114]. Based on the measured rise / response times, possible limitations concerning the speed of response of the photodetectors are discussed since the slowest time constant present in the device can be detected. A missing voltage dependence of the response time indicates that the detector is not limited by the carrier transit time.[168] On the other hand, if the transit time strongly affects the rise time, this can be detected by the consistency of the measured rise time with the theoretically expected transit time and slow components present in the speed of response are ascribed to carrier diffusion.[118] Furthermore, by comparing the response time with the estimated RC time, an RC limitation can be detected.[170] The trade-off between transit time and RC time was investigated with a thickness variation of the active material of a photodetector and an optimized thickness was established.[114]

2.2 Nanostructured Materials

2.2.1 3D – 2D – 1D – 0D Materials

In the bulk, charge carriers can move freely in all dimensions, assuming a free electron gas. Quantum confinement occurs when charge carriers are constricted in space, that is, when the size of the matter is limited in at least one dimension to lengths less than the Bohr exciton radius[171], cf. Formula (3). If confined in one dimension, a charge carrier can be described in this dimension as a particle in a 1D box with length (L), where the potential is zero inside the box and infinite otherwise.[61, 172] Solving the 1D Schrödinger equation[110]

$$-\frac{\hbar^2}{2m}\frac{\mathrm{d}^2\psi}{\mathrm{d}x^2} = E\psi \tag{29}$$

of a particle in a box in the direction (x), with the reduced Planck's constant ($\hbar$), the mass of the particle (m), and wave function (ψ), gives the energy levels (E)[61, 172]

$$E = \frac{h^2 n^2}{8mL^2} \tag{30}$$

with the principal quantum number (n). The number of energy levels ($dN(E)$) per energy interval (dE) gives the density of states ($D(E)$):

$$D(E) = \frac{dN(E)}{dE} \tag{31}$$

With varying degrees of freedom for the carriers, the densities of states differ. Assuming unit length of the confined box, the energy dependence of the density of states is given according to:[59, 61, 110, 172]

$$D^3(E) = \frac{1}{2\pi^2}\left(\frac{2m}{\hbar^2}\right)^{3/2}\sqrt{E} \tag{32a}$$

$$D^2(E) = \frac{m}{\pi\hbar^2} \tag{32b}$$

$$D^1(E) = \frac{1}{\pi\hbar}\sqrt{\frac{2m}{E}} \tag{32c}$$

$$D^0(E) = \sum \delta(E) \tag{32d}$$

for a 3D bulk system ($D^3(E)$), for a 2D system ($D^2(E)$) named quantum well, for a 1D system ($D^1(E)$) named quantum wire, and for a 0D system ($D^0(E)$) named quantum dot. This is shown in Figure 2.10.

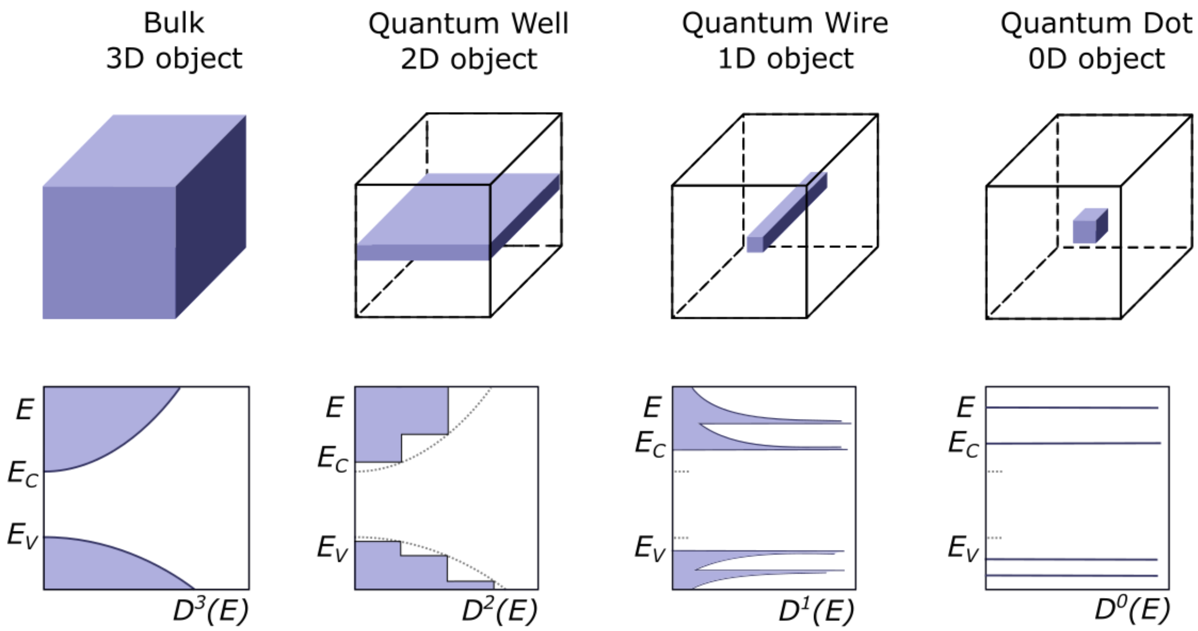

Figure 2.10. Effects of confinement. Structure and density of states for bulk material (3D), quantum well (2D), quantum wire (1D) and quantum dot (0D). Adapted with permission from Saleh and Teich[59] and modified. Copyright 1991, John Wiley & Sons, Inc.

2.2.2 CdSe Quantum Dots

The solution processed synthesis of semiconducting CdSe QDs is well studied and optimized and a narrow size distribution can be achieved.[173-175] The ligands used in the synthesis of QDs are usually insulating long-chain organic molecules that stabilize the particles colloidally. In order to obtain conductive CdSe QD films for use in optoelectronic devices, these ligands must be exchanged either for short ones, varying the tunnel barrier width[98, 102, 175-177], or by ones where an energy level alignment of ligand and QD leads to coupled nanostructures, varying the tunnel barrier height[178-181]. By tuning the ligand shell, high charge carrier mobilities in the QD films can be achieved.[182, 183] Since film fabrication from solution does not rely on epitaxial growth, QDs can be deposited on all kinds of substrate materials. Furthermore, QDs feature high extinction coefficients[184] making them ideal candidates for optoelectronic devices.[75, 182, 185]

The band gap of QDs is tunable by their size, with an increasing gap with decreasing particle diameter (cf. particle in a box, Formula (30)).[186-188] Bulk CdSe has a band gap of 1.74 eV[187], which increases to approx. 3.3 eV for 2 nm sized CdSe QD.[187] The exact energetic positions of the energy levels of a QD are influenced by the ligand shell.[187-190] Moreover, the ligands have a major impact on trap states at the QD interface[13, 16] due to surface passivation of dangling bonds. Thus, they influence the photoluminescence of QDs.[180, 191-194] While CdSe QDs are susceptible to surface oxidation and degradation[195], surface ligands can enhance their photostability.[196]

All these aspects offer a wide tunability of one and the same QD material for use in photodetectors. The QDs are adjustable for specific absorption requirements and band tuning can optimize the energy level alignment with the detector electrodes. For wurtzite CdSe QDs capped with iodide and interlinked with zinc β-tetraaminophthalocyanine (Zn4APc), the absorption of a thin film reaches into the first telecommunication window, cf. Figure 2.11 depicted in orange. This can be explained by an excitation of Zn4APc with subsequent carrier separation and transfer towards the QDs.[197] Thus, this material is applicable for both visible light communication and telecommunication and will be investigated in detail in this work.

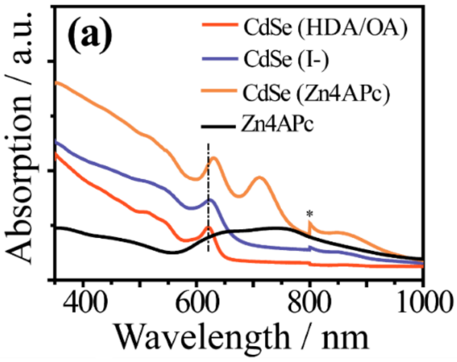

Figure 2.11. Absorption spectra of thin films of CdSe QDs with different ligands, deposited on glass. CdSe QDs with native ligand shell depicted in red, after ligand exchange with iodide given in blue, cross-linked with Zn4APc depicted in orange. Reprinted with permission from Kumar et al.[197] Copyright 2019, American Chemical Society.

2.2.3 WSe_2

Transition metal dichalcogenides MX_2, M = metal, X= chalcogen, are layered materials of the monolayer units X – M – X, where weak van der Waals interactions between the layers allow for scotch tape exfoliation of thin flakes from bulk crystals and an easy application on any substrate is achievable using viscoelastic stamps.[198-200] Their high mechanical stability[201, 202] renders TMDCs optimal materials for applications on flexible substrates.

The electronic properties of TMDCs range from metallic to semiconducting[203, 204] and when exploited in electronic devices, semiconducting TMDCs, like WSe_2, offer high charge carrier mobilities and high on / off ratios in field-effect transistors.[200, 205-208] Moreover, TMDCs offer a tunable, layer dependent band gap in the visible range with a gradual shift from an indirect to a larger, direct gap in the monolayer.[209-212] The band gap of a WSe_2 monolayer on Si/SiO_2 arises to approx. 1.6 eV[206, 211, 213-215] and for the bulk crystal, values of approx. 0.9 eV[213, 216] to 1.2 eV[206, 211, 214, 215, 217] are reported in literature. The band gap can further be influenced by strain, intercalation and alloying.[203, 209, 216, 218] The transport property of WSe_2 is tunable by the layer thickness and n-type conductance is usually observed for thick bulk-like crystals, which changes via ambipolar to p-type conductivity for thin flakes.[206, 213, 219] This can further be modified by external factors like the choice and fabrication of metal electrodes or surface doping.[206, 208, 213, 220, 221]

Both optical and electrical properties of TMDCs are influenced by excitons, biexcitons and charged excitons, so-called trions (two electrons and one hole or one electron and two holes), which are stable at room temperature due to excitonic binding energies larger than $k_B T = 25.7\text{ meV}$.[64, 216, 222-224] In the bulk, the exciton binding energy arises to approx. 60 meV.[222, 225] Interactions between charges in a semiconducting thin film increase when the film thickness decreases and become significant if the distance between charges is equal to, or larger than the film thickness.[65] This leads to a pronounced increase of the exciton binding energy[226, 227] for thinner layers, which is visible for a WSe_2 monolayer on top of Si/SiO_2 having an exciton binding energy of 0.79 eV.[64] The corresponding trion binding energy is approx. 30 meV[222] and is reported to be similar for both positive and negative trions[228], or larger for the negative trion.[229, 230] The binding energy of biexcitons in monolayer WSe_2 on top of Si/SiO_2 is measured to be 52 meV.[224] The lifetime of trions is larger than for excitons and is further enhanced when going from the monolayer to multilayers.[231]

This large tunability makes TMDCs an attractive class of materials for application in optoelectronic devices. WSe_2 flakes are investigated in this work as absorber in photodetectors using different substrate materials.

2.3 Dielectric Effects

With solution-processability and exfoliation procedures, the method of epitaxial growth can be avoided for the preparation of both CdSe QD and WSe_2 photodetectors. Many different substrates can be used in their development, which differ significantly in their dielectric properties. An electric field displaces permanent dipoles and causes induced dipoles, with the dielectric constant as a measure of the polarizability of matter. The dielectric constant connects the electric displacement field (D) and the electric field ($\mathcal{E}$) via[110, 172]

$$D = \varepsilon_0 \mathcal{E} + P = \varepsilon_0 \varepsilon_r \mathcal{E} \tag{33}$$

with the polarization (P), the vacuum permittivity (ε_0) and the relative permittivity or dielectric constant (ε_r). Due to the polarization of matter, the electric field of a charge is screened by $1/\varepsilon_r$ compared to the electric field in vacuum. Thus, the dielectric constant affects the interaction between charge carriers and therefore the optoelectronic properties of a material.

To the best of my knowledge, no detailed study exists that investigates the influence of the dielectric constant of the substrate on the speed of response of a photodetector. Nevertheless, many effects of the surrounding dielectric on both QDs and layered TMDCs are known, and a brief impression is provided in this Chapter.

2.3.1 On Quantum Dots

An enhanced dielectric constant of the environment increases the excitonic ground state energy of QDs[232, 233] and influences the photoluminescence of the material and its dynamics.[234-236] Moreover, the chosen substrate has an impact on the photostability of CdSe QDs due to a possible charge separation and transfer after the excitation.[237] In the specific application of QDs as active material in photodetectors, their characteristics are fundamentally determined by the charge carrier flow through the particle film. Charge transport depends on three factors: the charging energy (E_C), the transfer integral (β), and the energetic disorder ($\Delta\alpha$).[75, 171, 177, 181, 238-241] The charging energy is the energy it takes to add an electron onto an electrically neutral QD, the transfer integral describes the tunneling of charge carriers when QDs are in close proximity and their wave functions overlap and the energetic disorder is induced by variations of the QDs in size, shape and composition, leading to a dispersion of energy levels. The interplay of these three parameters decides whether an insulating or conducting structure is present. A large charging energy and a large energetic disorder inhibit carrier transport, while it is supported by a large transfer integral.

The dielectric constant influences the charging energy substantially. Not only the static dielectric constant of the QD (ε_{QD}) but also of its surrounding (ε_M) have to be considered and the charging energy can be calculated according to the Laikhtman-Wolf model:[181, 241, 242]

$$E_C = \frac{e^2}{2(C_S + nC_M)} \tag{34a}$$

via the self-capacitance (C_S) of the QD[243] and the mutual capacitance (C_M) of a QD and its (n) nearest neighbors:[177, 240, 241]

$$\frac{1}{C_S} = \frac{1}{4\pi\varepsilon_0 r}\left(\frac{\varepsilon_{QD} - \varepsilon_M}{\varepsilon_{QD}\varepsilon_M} + \frac{0.94(\varepsilon_{QD} - \varepsilon_M)}{\varepsilon_{QD}(\varepsilon_{QD} + \varepsilon_M)}\right) \tag{34b}$$

$$C_M \approx 2\pi\varepsilon_0 r \frac{\varepsilon_{QD}\varepsilon_M}{\varepsilon_{QD} - \varepsilon_M} \cdot \ln\left(\frac{2r + d}{d}\right) \tag{34c}$$

with the QD radius (r) and the inter-particle distance (d).

The charging energy is reduced for an increasing dielectric constant of the environment.[240, 244] This is calculated, e.g., for PbSe QDs of different sizes, with the largest variations in charging energy occurring for dielectric constants of the surrounding material smaller than ten, see Figure 2.12.[244]

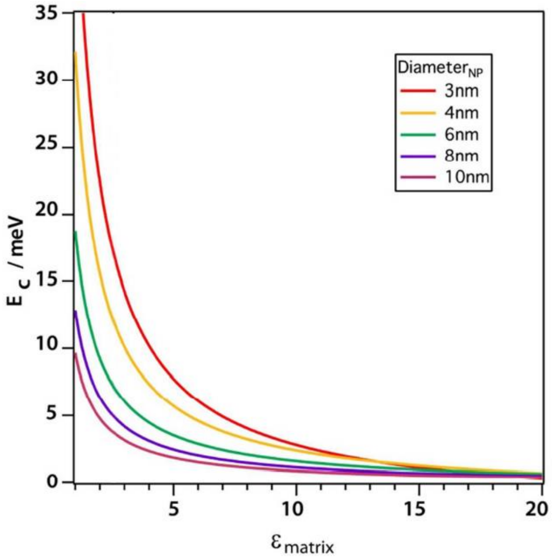

Figure 2.12. Effect of the dielectric constant of the surrounding environment (ε_{matix}) on the charging energy of quantum dots. Reprinted with permission from Scheele et al.[244] Copyright 2013, American Chemical Society.

The charging energy affects the transfer integral, which is consequently influenced by the dielectric constant of the environment as well. The transfer integral can be gauged according to[181, 238]

$$\beta \approx 2E_a e^{-\frac{E_a}{k_B T}} e^{-2\sqrt{\frac{2m^*\Delta E}{\hbar^2}}\Delta x} \tag{35}$$

with the activation energy (E_a) containing both the charging energy and the energetic disorder[181, 238, 244], using the tunnel barrier height (ΔE) and width (Δx), and the charge carrier effective mass (m^*).

In summary, charge transport in a QD film depends significantly on the dielectric constant of the medium surrounding the QDs. My hypothesis is that not only the ligands exert a strong impact on the QD film, but also the substrate on which the QDs are deposited. It can be assumed that the QDs directly attached to the substrate are most strongly affected. I expect that the influence of the substrate can alter the performance of a photodetector. Therefore, in this work, I examine identical CdSe QD based thin films on different substrates using bottom-contact electrodes and focus on the speed of response of these photodetectors.

2.3.2 On Transition Metal Dichalcogenides

On top of Si/SiO$_2$ substrates, the charge carrier mobilities in thin TMDC flakes are quite low.[22, 245, 246] They can be improved by using high-κ-dielectrics, that reduce the scattering of free charge carriers from ionized impurities (Coulomb scattering),[19, 207, 212, 247, 248] and also diffusion constants are affected.[249] The dielectric environment furthermore tunes the band gap of TMDCs, with a decreasing gap for high dielectric constants.[227, 250, 251] This can be exploited to build a heterojunction within a homogeneous TMDC monolayer if two different substrates are utilized in one device.[250, 252]

In addition, the excitonic properties of TMDCs are strongly affected by the surrounding dielectric constant. An increased dielectric constant enhances the lifetime of both trions and excitons and decreases their ratio (trions / excitons), as shown for a MoS$_2$ monolayer influenced by different nonionic organic solvents.[253] This ratio depends on the optical power of the laser.[254] In monolayers, excitons are frequently described by the distance-dependent electrostatic potential ($V(r)$) between two charges, originally given by Keldysh:[65, 228, 255-257]

$$V(r) = -\frac{e^2}{8\varepsilon_0 r_0}\left[H_0\left(\frac{\kappa r}{r_0}\right) - Y_0\left(\frac{\kappa r}{r_0}\right)\right] \tag{36a}$$

$$\kappa = \frac{\varepsilon_b + \varepsilon_t}{2} \tag{36b}$$

with the characteristic screening length ($r_0 = 2\pi\chi$), related to the 2D polarizability of the monolayer material (χ), and the Struve function (H_0) and Bessel function (Y_0) of second kind. The influence of the dielectric environment is included by the average dielectric constant of the surrounding material (κ), which is calculated via the dielectric constants of both the top and the bottom layer around the monolayer ($\varepsilon_t, \varepsilon_b$), respectively. This formula is valid for $\kappa < \varepsilon_{r,TMDC}$. With that, the exciton binding energy (E_B) was calculated to depend on the dielectric constant of the surrounding dielectrics according to[228, 253, 255]

$$E_B = \frac{E_B(\kappa = 1)}{\kappa^\alpha} \tag{37}$$

with the empirical scaling factor $\alpha \approx 0.7 - 0.95$.[228, 253, 255] The trion binding energy scales similarly but with a smaller scaling factor.[253] Thus, both exciton and trion binding energies decrease for increasing dielectric constant of the surrounding.[227, 251, 254] This is also reflected in an enlarged exciton radius.[255] Interactions between charges in a semiconducting thin film increase when the film thickness decreases[65], therefore, these effects are often investigated for TMDC monolayer systems.

Due to the strong influences that dielectrics have on the optoelectronic properties of TMDCs, I assume that photodetectors based on these materials also exhibit significant variations depending on the dielectric environment like the substrate material. Therefore, in this work, I study WSe_2 flakes on different substrates using bottom-contact electrodes and I check for variations in their speed of photoresponse.

3

Methods and Materials

3.1 Time-Resolved Photocurrent Measurements

Optoelectronic investigations were performed at room temperature in a *Lake Shore Cryotronics CRX-6.5K* probe station and measurements were taken under vacuum, nitrogen, or atmosphere. The photodetector electrodes were contacted using 50 Ω impedance matched tungsten probes (*Lake Shore Cryotronics ZN50R DC/RF*) and coaxial RF cables (*RG 58 ALL*) chosen as short as possible. In case of the homebuilt photodetectors, the photoresponse was preamplified by a *FEMTO DHPCA-100* current amplifier, converting the current signal into an amplified voltage (transimpedance amplifier). This signal was measured by a *Zurich Instruments UHFLI* lock-in amplifier with 1 MΩ input impedance. Using the Periodic Waveform Analyzer Function, signals were typically averaged over 2G samples, and a bias was applied to the photodetectors using the auxiliary output of the lock-in amplifier (max. ±10 V). For examination of the commercial photodetectors, the preamplifier was removed due to very high photocurrents and an input impedance of the lock-in amplifier of 50 Ω was chosen. All signals were background corrected. The time resolution of the setup is restricted by the lock-in amplifier to 600 MHz, i.e., to about 1.7 ns. The schematic of the setup is shown in Figure 3.1a. The *UHFLI* amplifier was implemented into the setup with the specialist advice of Claudius Riek (Application Scientist at Zurich Instruments).

Two measurement techniques were established for the time-resolved examination of photodetectors, cf. Figures 3.1b and 3.1c: Steady state measurements using square pulse illumination and non-steady state measurements using impulse illumination. Square pulse illumination was performed using a *PicoQuant FSL500* fast switchable laser driver with a laser rise time of < 0.5 ns together with a 635 nm (1.95 eV) laser diode with an output power of 4 mW / 12 mW. Repetition rates of ≥ 3 MHz can be triggered internally, all slower repetition rates used were triggered externally with a *Hewlett Packard 33120A arbitrary waveform generator*. Impulse illumination was executed using a *PicoQuant Taiko PDL M1* picosecond pulsed laser driver together with 636 nm (1.95 eV) and 779 nm (1.59 eV) laser diodes with a full width half maximum of the pulse of < 0.5 ns. For the examination of commercial photodetectors, repetition rates of 3 MHz and 20 kHz were selected with average output powers of ≤ 80 µW and 249 nW, respectively. For the homebuilt photodetectors, repetition rates of 100 kHz and 1 MHz were chosen with average output powers of 22 µW and 220 µW, respectively. The given output laser powers were attenuated because of inefficient coupling into the optical fibers, scattering, decollimation of the beam, etc. The laser spot is not focused to illuminate the whole electrode area and to prevent heating and damage of the detectors. The bandwidths of the photodetectors are determined via the power spectrum, by fast Fourier transformation FFT of the impulse response according to Formula (4).

I performed the time-resolved photocurrent investigations shown in this work by myself, with some of the studies of the CdSe/I^-/Zn4APc detectors on glass performed in close collaboration with Fabian Strauß.

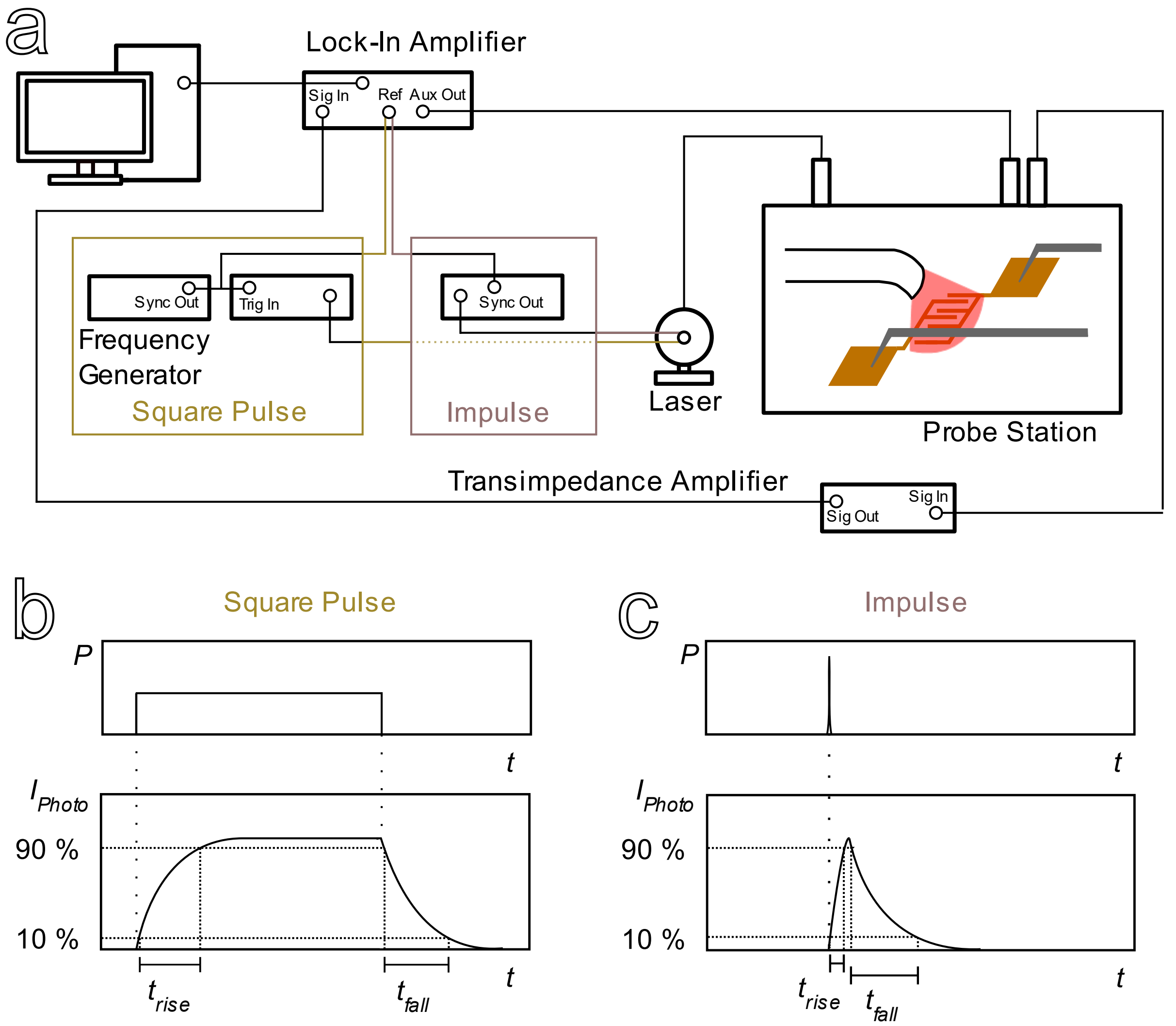

Figure 3.1. Schematic of the time-resolved photocurrent investigations. a) Setup with the established b) square pulse and c) impulse illumination technique.

3.2 Conductivity Measurements

Electrical measurements were executed in a *Lake Shore Cryotronics CRX-6.5K* probe station at room temperature using a *Keithley 2634B System Source Meter*. The device electrodes were contacted with tungsten two-point probes.

3.3 Impedance Spectroscopy

Impedance Spectroscopy was performed using a *CH Instruments Electrochemical Analyzer / Workstation Model 760E* with the specialist advice of Dr. Alexandru Oprea and Kai Wurst. The device electrodes were contacted using tungsten two-point probes. One was connected to the working electrode of the potentiostat and the other to both, reference electrode and counter electrode of the potentiostat. Typical measurements were performed in the frequency range from 10^5 Hz to 10^{-1} Hz (10^{-3} Hz). There was no constant bias applied, and the measurement amplitude was set to 500 mV, resulting in powers P < 0.5 μW and preventing the sample from heating during measurement. Automatic sensitivity scale setting was chosen, and 12 points / decade frequency were measured with 1 cycle per decade. Fourier transformation (FT) measurement mode was used for frequencies above 100 Hz and switched automatically to single frequency mode for lower frequencies.

The equivalent circuit of our detectors was assumed to be a parallel circuit of constant phase element (Y_0, n) and resistor (R), similar to Livache et al.[133] The spectra were fitted using the impedance package for python[258] and the effective capacitance was calculated using $C_{eff} = (Y_0 \cdot R^{1-n})^{\frac{1}{n}}$.[259]

3.4 Atomic Force Microscopy

Atomic force microscopy (AFM) images were taken with a *Bruker MultiMode 8-HR* in contact mode, with some of the measurements being performed by Pia Kohlschreiber.

3.5 Scanning Electron Microscopy

Scanning electron micrographs were taken using a *HITACHI model SU8030* by Elke Nadler and Dr. Andre Maier and using a *Philips FEI XL-30* (with *XENOS pattern generator* for electron beam lithography) by Fabian Strauß.

3.6 Photodetectors

3.6.1 Commercial Photodetectors

Commercially available photodiodes and phototransistors were investigated to verify the time-resolved measurement setup. BPW 34[260] and SFH 203 P[261] photodiodes and BPX 81-3[262] phototransistor by *Osram Opto Semiconductors* and SDP8406[263] phototransistor by *Honeywell* were used. They are shown in Figure 3.2.

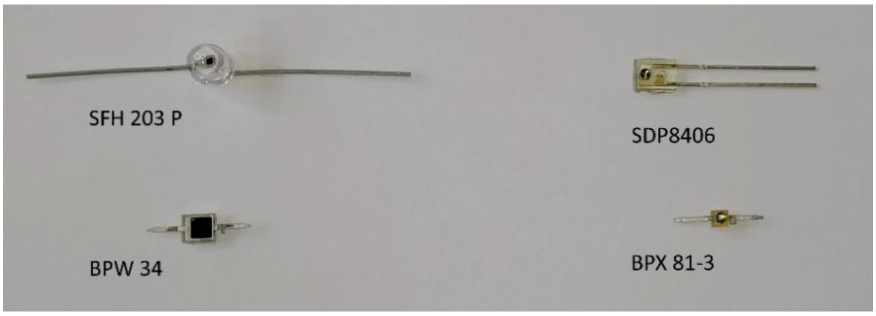

Figure 3.2. Commercial photodetectors investigated. Photodiodes on the left, phototransistors on the right.

3.6.2 Substrates Used

Cf. Chapter 5.1. Commercially available bottom-gate bottom-contact Si-FET substrates (n-doped silicon, $n = 3 \cdot 10^{17}\ \mathrm{cm}^{-3}$) with 230 nm or 770 nm thermal oxide and interdigitated electrodes (10 nm ITO / 30 nm Au, 20 µm finger width) of varying channel length (2.5 µm, 5 µm, 10 µm, 20 µm) and 10 mm channel width of the Fraunhofer Institute for Photonic Microsystems, Dresden, Germany were investigated.

Used in CdSe/I$^-$/Zn4APc thin film studies, cf. Chapter 6. Interdigitated electrodes (3 nm Ti / 20 nm Au, 20 µm finger width) with various channel lengths (2.5 µm, 5 µm, 10 µm, 20 µm) and 10 mm channel width were photolithographically prepared on glass (Duran Wheaton Kimble; 76×26 mm; soda-lime glass), coated with hexamethyldisilazane (HMDS), and on 0.125 mm polyimide foil (DuPont™ Kapton® HN) by Dr. Andre Maier and Fabian Strauß. Furthermore, interdigitated electrodes (4 nm Ti / 20 nm Au, 85 nm finger width) of 350 nm, 500 nm channel length and 10 mm channel width were prepared using electron beam lithography by Fabian Strauß. Details of the preparation procedures are described elsewhere.[49] Characterization of the substrates is given in Figure 3.3.

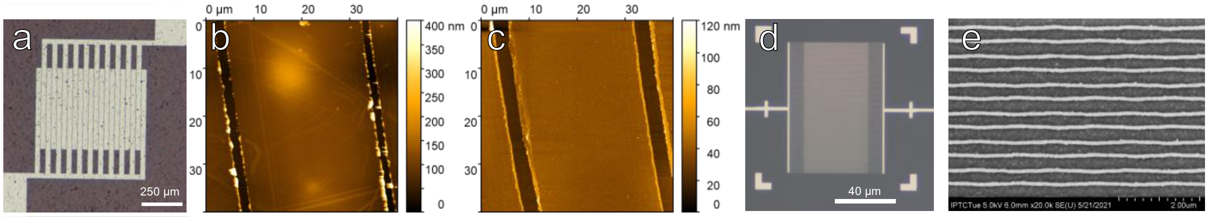

Figure 3.3. Substrates used. a) Light microscope image of 2.5 µm × 10 mm electrode geometry, example on polyimide foil. Characterization of the 2.5 µm gap electrodes on b) polyimide and c) glass, using AFM. d) Light microscope image of a 350 nm × 10 mm electrode on glass with the characterization of the gap by e) SEM measurements. Adapted with permission from Schedel et al.[49] and modified. Copyright 2021, American Chemical Society.

Used in WSe$_2$ photodetector examinations, cf. Chapter 7. Gold electrodes (2 nm Ti / 8 nm Au, 10 µm finger width) with 2.5 µm, 5 µm channel length and 80 µm channel width were photolithographically prepared on glass (Duran Wheaton Kimble; 76×26 mm; soda-lime glass), coated with HMDS, and on 0.125 mm polyimide foil (DuPont™ Kapton® HN) by Fabian Strauß, as described elsewhere.[50] Characterization of the substrates is given in Figure 3.4.

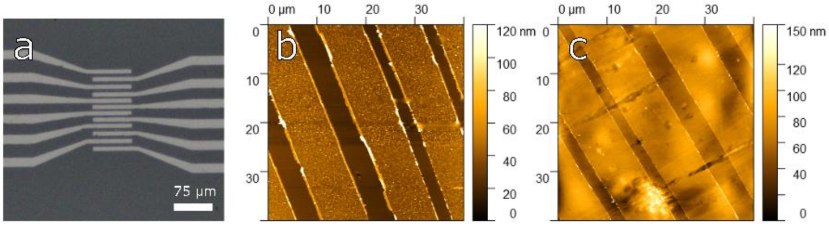

Figure 3.4. a) Light microscope image of 2.5 µm, 5 µm × 80 µm electrode geometry on glass with the characterization of the electrode gaps on b) glass and c) polyimide using AFM.

3.6.3 CdSe/I$^-$/Zn4APc Thin Film Preparation

CdSe QDs used were synthesized by Patrick Tim Michel following a procedure of Sayevich et al[175] and described elsewhere.[49] A size of 4.5 ± 0.4 nm was achieved, cf. Figure 3.5.

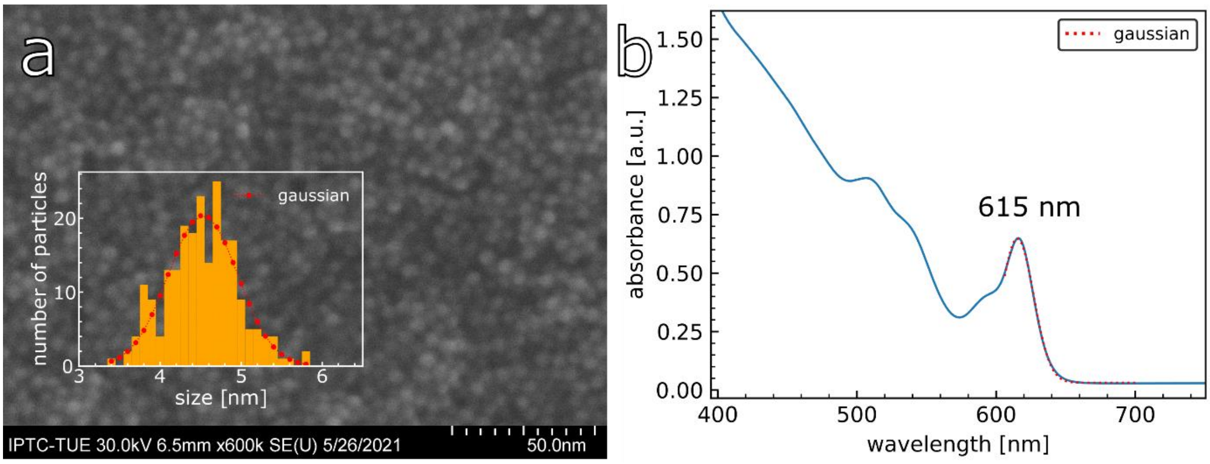

Figure 3.5. CdSe QDs used. a) SEM image with size distribution of the quantum dots of 4.5 ± 0.4 nm, b) UV/Vis spectrum of the quantum dots with native ligand shell in hexane, indicating 5.3 nm sized particles according to Yu et al.[184] Adapted with permission from Schedel et al.[49] and modified. Copyright 2021, American Chemical Society.

A typical film preparation procedure was developed by Dr. Krishan Kumar and performed under nitrogen atmosphere as described elsewhere.[197] In short, 45 µL of a 88 µM solution of 4.5 nm sized CdSe/I$^-$ QDs in N-methylformamide and ~ 65 µL of a saturated solution of zinc β-tetraaminophthalocyanine (Zn4APc) in dimethylsulfoxide were deposited on a substrate. A CdSe/I$^-$/Zn4APc film formed over-night and remaining solvent was spun-off the substrate (10 rps for 60 s, then 30 rps for 30 s, finally 70 rps for 20 s). The film was washed with acetonitrile to remove unbound Zn4APc and annealed at 190°C for 30 min. Using a home-built transfer arm, cf. Figure 3.6, the films were transferred into the probe station under nitrogen and the devices were investigated under vacuum.

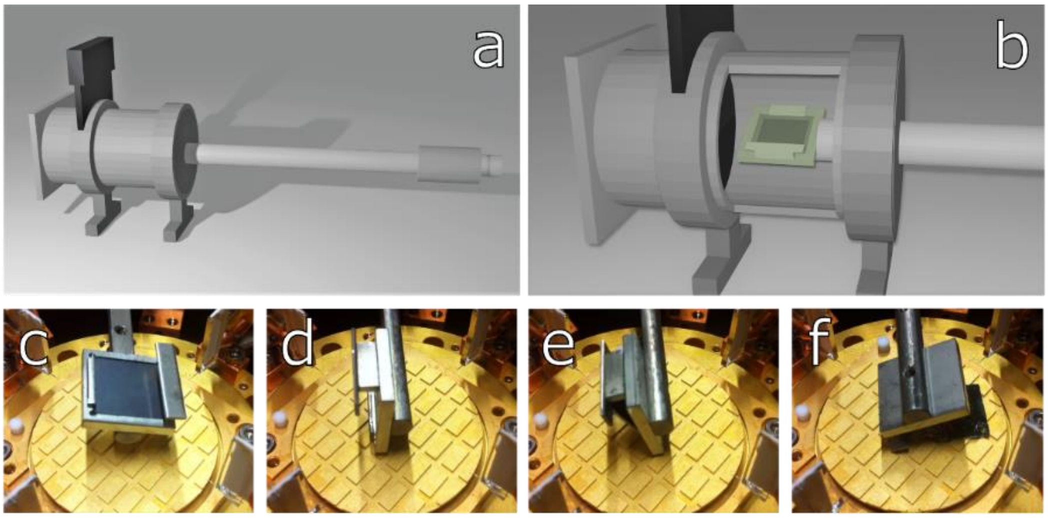

Figure 3.6. Home-built transfer arm, developed with the specialist advice of Hilmar Adler. a) Complete transfer arm, b) view into the air-tight transfer chamber with the home-built sample holder. c-f) Sequence of sample dropping from the sample holder: The sample lies upside down on the frame of the sample holder. By rotating the magnetic transfer arm, the sample is ejected from the sample holder with the top side up.

Exemplary light microscope images of the CdSe/I^-/Zn4APc films are shown in Figure 3.7, revealing thin and thick regions. The film morphology is comparable on both substrates, as characterized by AFM and profilometer measurements (the latter taken by Fabian Strauß). The thin areas of the film have a surface roughness of 149 ± 13 nm and 306 ± 24 nm on polyimide and glass, respectively. The cracks in the thick areas reveal a maximum thickness of the films of approx. 3.5 µm.

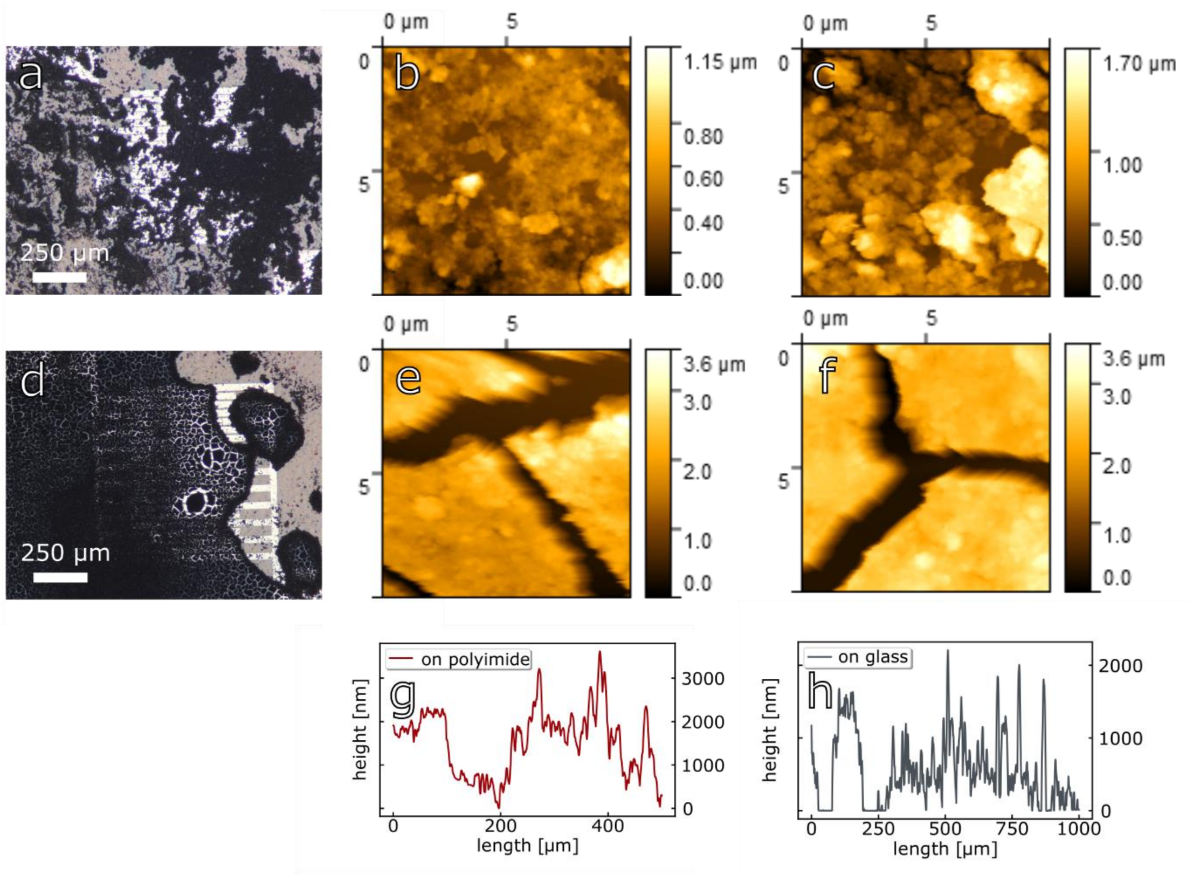

Figure 3.7. CdSe/I^-/Zn4APc film on polyimide (a, b, d, e, g) and glass (c, f, h). a) Light microscope image of a typical ”thin” area of the film, exemplarily shown for a 5 µm channel length device prepared on polyimide, with AFM characterization of these areas on top of b) polyimide (root mean square roughness of 149 ± 13 nm) and c) glass (root mean square roughness of 306 ± 24 nm). d) Light microscope image of a typical thick area with cracks, exemplarily shown for a 10 µm channel length device on top of polyimide, with AFM characterization of these thick areas deposited on e) polyimide and f) glass. Profilometer measurements of the CdSe/I^-/Zn4APc film on g) polyimide and h) glass. Adapted with permission from Schedel et al.[49] and modified. Copyright 2021, American Chemical Society.

3.6.4 WSe_2 Exfoliation and Stamping Procedure

WSe_2 flakes were mechanically exfoliated from a WSe_2 crystal (2Dsemiconductors Inc., USA) using scotch tape (Scotch Magic™ Tape), adopting the procedure of Castellanos-Gomez et al.[198] The procedure is shown in Figure 3.8. Under ambient conditions, flakes were exfoliated from the WSe_2 crystal and transferred to a polydimethylsiloxane (PDMS) stamp (PF Gel Film®, Teltec GmbH). Flakes were selected using an optical microscope and excess flakes were removed by cutting the PDMS stamp with a scalpel. The flake to be examined was transferred to the chosen substrate by bringing the PDMS stamp in contact with the substrate and then slowly pulling it off, using the micromanipulator screws of the light microscope setup. The light microscope setup for TMDC exfoliation and stamping was built by Olympia Geladari.

The thickness of the exfoliated flakes was investigated via AFM, cf. Figure 3.9. The light micrographs of the WSe_2 flakes on top of the electrodes and their corresponding AFM images, including their height profiles, are shown in Figure 3.9. The flakes on glass have a thickness of approx. 30 – 50 nm, and on polyimide, both a 50 nm thick flake and significantly thicker flakes of 120 – 200 nm have been investigated.

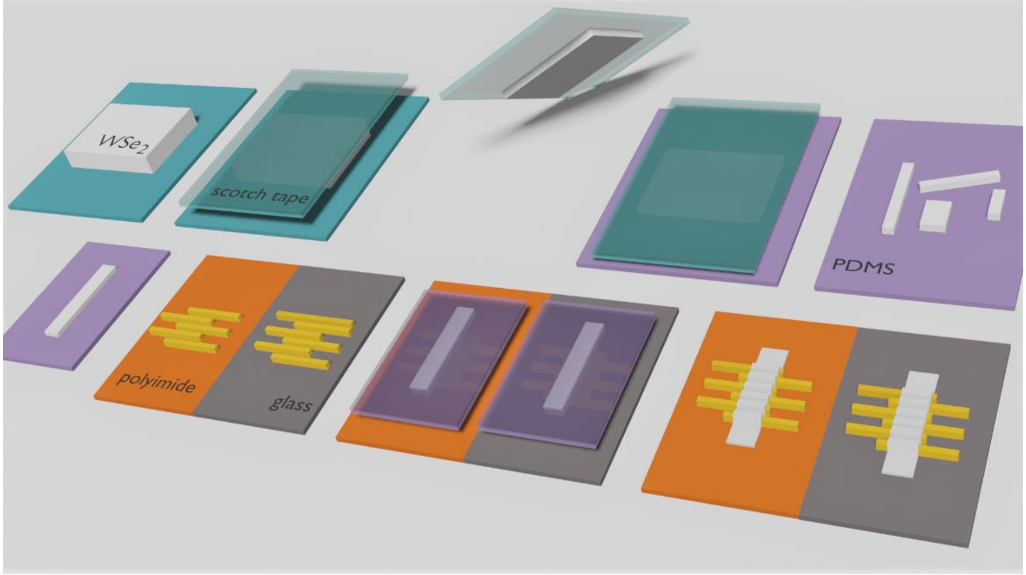

Figure 3.8. WSe_2 exfoliation and stamping procedure. Adapted with permission from Schedel et al.[50] and modified. Copyright 2022, the Royal Society of Chemistry (PCCP Owner Societies).

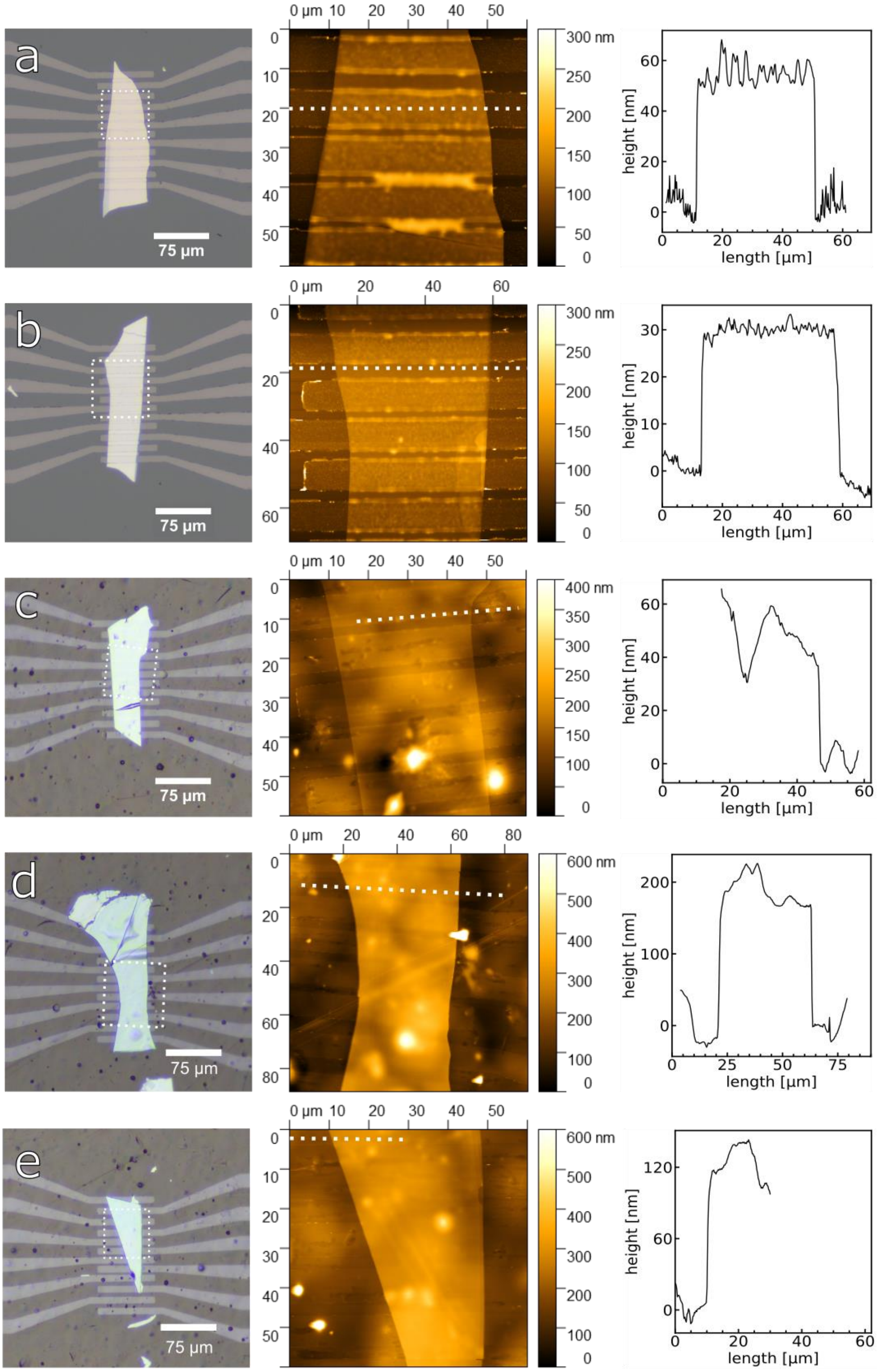

Figure 3.9. Light microscope and AFM images of the investigated WSe_2 flakes on (a, b) glass and (c-e) polyimide. White boxes indicate corresponding AFM cutouts, white lines display the position of the line cuts for height profile measurements. Adapted with permission from Schedel et al.[50] and modified. Copyright 2022, the Royal Society of Chemistry (PCCP Owner Societies).

4

Proof of Concept: The Time-Resolved Photocurrent Setup

Related Talk

- ‘Time-Resolved Photocurrent Measurements‘, *714. WE-Heraeus-Seminar: Resolving the Full Picture: Complementary Spectroscopic Approaches to Explore Dynamics in Physical and Chemical Systems*, **2020**, Bad Honnef, Germany.

Related Article

- Schedel, C.; Strauß, F.; Scheele, M., Pitfalls in Determining the Electrical Bandwidth of Nonideal Nanomaterials for Photodetection. *J. Phys. Chem. C* **2022,** *126* (32), 14011-14016.

In this Chapter, the two commercial silicon p-i-n photodiodes BPW 34 and SFH 203 P and the two commercial silicon n-p-n phototransistors SDP8406 and BPX 81-3 are examined regarding their speed of response to verify the functionality of the established setup for time-resolved photocurrent measurements. The photodetector rise and fall times (10 % – 90 %) towards square pulse illumination are given in the respective data sheets and are compared to the photoresponses measured. Besides square pulse illumination reaching steady state photocurrent, impulse illumination, hence, the non-steady state condition, is investigated.

4.1 Confirmation of Rise Times

The investigated photodiodes (BPW 34, SFH 203 P) are specified in the data sheets with rise times of a few nanoseconds and the phototransistors (SDP8406, BPW 81-3), the slower devices, with rise times of a few microseconds. In Table 4.1, the rise times given in the data sheets are listed together with the parameters required to achieve these values. In addition, the parameters I used for the measurements are given. They partly show deviations from the ones used for the specification of the detectors in the data sheet, so I gauged the expected rise times according to them.

Table 4.1. Specifications of the investigated photodetectors.

photodetector	rise time data sheet	parameters data sheet	parameters applied	rise time expected
BPW 34 [260]	20 ns	$U = 5\text{ V}$ $R_L = 50\ \Omega$	$U = 5\text{ V}$ $R_L = 50\ \Omega$	20 ns
SFH 203 P [261]	5 ns	$U = 20\text{ V}$ $R_L = 50\ \Omega$	$U = 10\text{ V}$ $R_L = 50\ \Omega$	> 5 ns
SDP8406 [263]	~ 2.8 µs	$U = 5\text{ V}$ $R_L = 50\ \Omega$ $I_E = 1\text{ mA}$	$U = 5\text{ V}$ $R_L = 50\ \Omega$ $I_E = 5.4\text{ mA}$	< 2.8µs
BPX 81-3 [262]	6 µs	$U = 5\text{ V}$ $R_L = 1\text{ k}\Omega$ $I_E = 1\text{mA}$	$U = 5\text{ V}$ $R_L = 50\ \Omega$ $I_E = 0.6\text{ mA}$	< 6µs

The diode BPW 34 could be examined under the conditions given in the data sheet, therefore, the 20 ns rise time of the data sheet is expected to be measurable with the setup. The developed setup is limited to a maximum applicable bias of 10 V, thus, the SFH 203 P diode could not be tested under 20 V reverse bias (U) and a slightly slower response than 5 ns is expected for 10 V bias applied. For both phototransistors, the current under illumination (I_E) could not be set exactly to 1 mA what gives rise to minor deviations from the values given in the data sheets. Due to the higher current, SDP8406 is expected to be faster than 2.8 µs, whereas a slowdown is to be expected for the BPX 81-3 transistor, cf. Formula (24).

However, BPX 81-3 is also measured under significantly reduced load resistance (R_L), which in turn suggests a considerable acceleration of the device according to Formula (18). Therefore, I expect a rise time faster than 6 µs.

The normalized photoresponses of both photodiodes and phototransistors towards 635 nm square pulse illumination and 636 nm impulse illumination are shown in Figure 4.1. A 3 MHz laser repetition rate (using 100 ns pulse width for square pulse illumination) was chosen for the examination of the photodiodes since the expected rise times are a few nanoseconds. Phototransistors with their microsecond responses were investigated under 20 kHz laser repetition rate (using 25 µs pulse width for square pulse illumination).

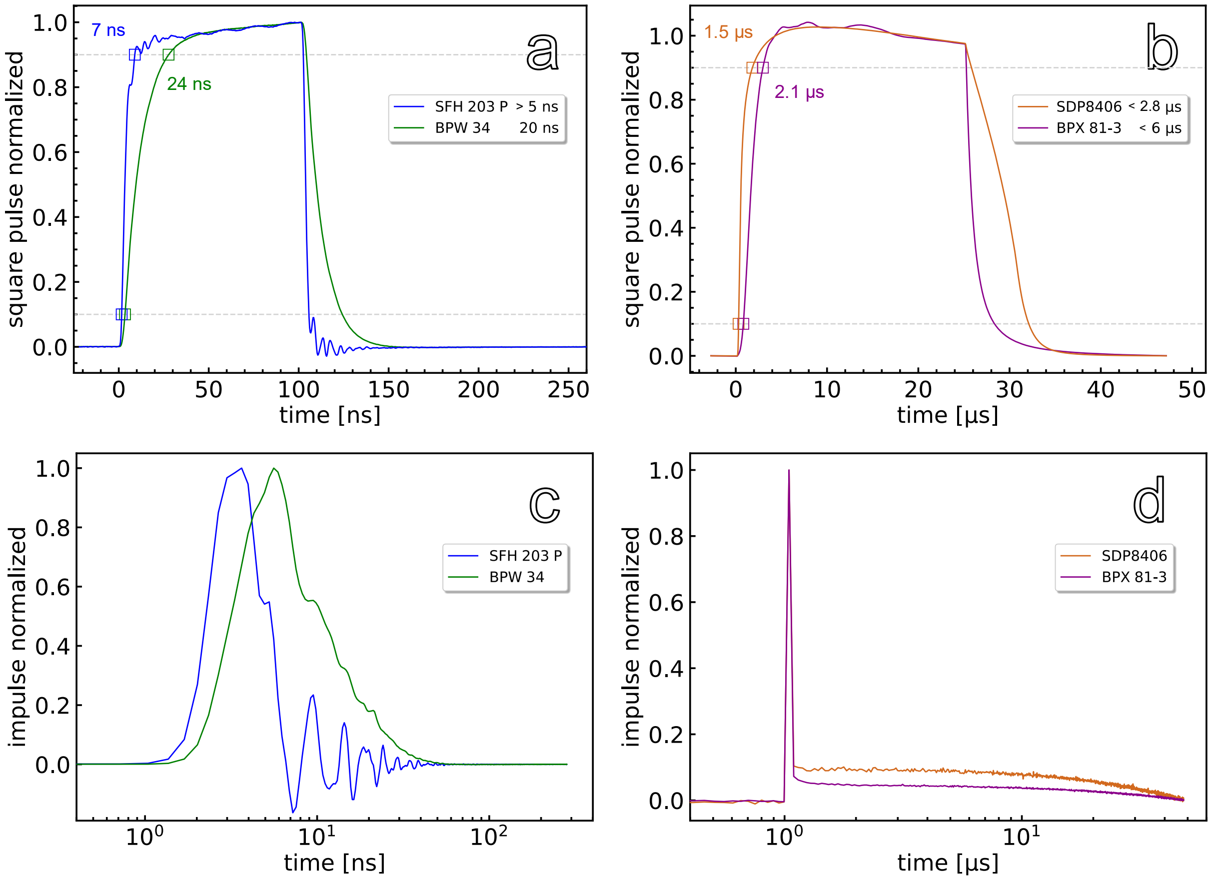

Figure 4.1. Normalized time-resolved photoelectrical responses of (a, c) the two commercial photodiodes (SFH 203 P and BPW 34) and (b, d) the two commercial phototransistors (SDP8406 and BPX 81-3) under (a, b) 635 nm square pulse illumination with pulse widths = 100 ns and 25 µs, respectively, and (c, d) 636 nm impulse illumination with pulse width ≤ 500 ps.

As can be seen from Figure 4.1a, the rise times of the photodiodes BPW 34 and SFH 203 P under square pulse illumination are 24 ns and 7 ns, respectively. They fit perfectly to the expected values of 20 ns and > 5 ns, cf. Table 4.1. The phototransistors SDP8406 and BPX 81-3 show values of 1.5 µs and 2.1 µs, respectively, see Figure 4.1b, and by that, are in the expected ranges of < 2.8 µs and < 6 µs, respectively, cf. Table 4.1. Hence, for all four commercial photodetectors the correct rise times towards square pulse illumination are obtained, verifying the applicability of the setup for time-resolved photocurrent examinations.

The normalized impulse photoresponses of the same commercial photodetectors are shown in Figures 4.1c and 4.1d. Photodiodes show a very fast nanosecond response with the SFH 203 P diode being faster than the BPW 34, which fits to the speed of response under square pulse illumination. The SFH 203 P photodiode exhibits ringing, which occurs in photodiodes whose photoresponse is optimized for the frequency domain, not the time domain, thus enabling large bandwidths.[264-266] Both phototransistors are significantly slower than the photodiodes, as expected, and show slowly decaying long tails that last for microseconds.

4.2 Confirmation of Non-Steady State ("Impulse") Data

To confirm the accuracy of the non-steady state or impulse measurements, their photoresponses are compared to the square pulse photoresponses. Impulse measurements require a short, delta-shaped light pulse and square pulse illumination starts with an abrupt, step-shaped switch from the dark towards continuous wave illumination of a device. Since the delta function is the derivative of the Heaviside step function, the photoresponse of a photodetector to a laser impulse is related to its corresponding turn-on photoresponse under square pulse illumination. The integration of the impulse photoresponse should be comparable to the first half of the measured square pulse photoresponse. This is exemplarily shown in Figure 4.2 for the photodiode BPW 34. Integrated impulse response and the turn-on of the square pulse photocurrent match very well and thus validate the impulse studies.

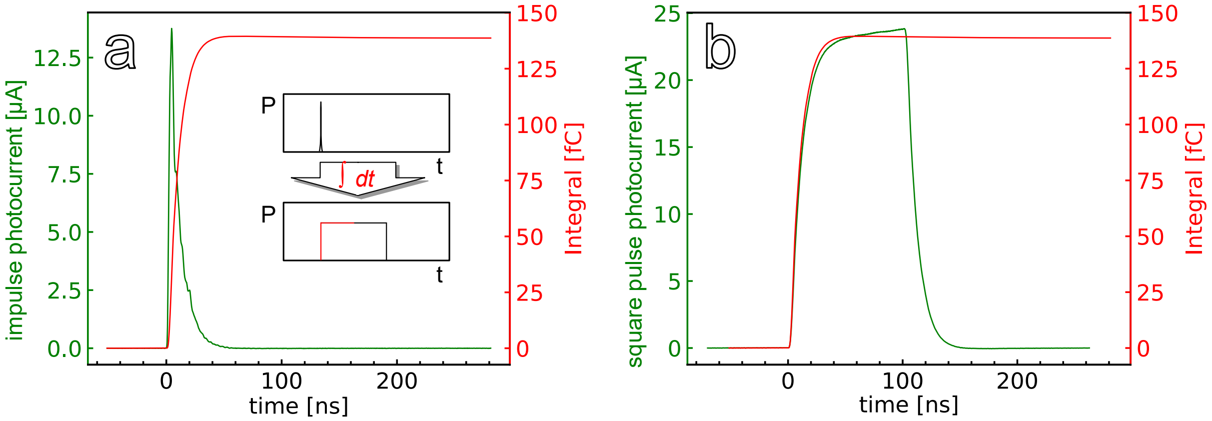

Figure 4.2. a) Impulse response (green) and the corresponding trapezoidal integral (red) of the photodiode BPW 34. b) Comparison of the integrated impulse response (red) of BPW 34 with its square pulse response.

4.3 Bandwidth Estimation

Both the square pulse and the impulse photocurrent data can be used to characterize the speed of a photodetector in terms of bandwidth. As specified in Chapter 2.1.1, the bandwidth of a detector can be calculated from the impulse response using fast Fourier transformation, cf. Formula (4). Plotted in logarithmic dB scale with $\mathrm{dB} = 10log_{10}\frac{P(\omega)}{P_1}$, this is shown for the BPW 34 photodiode in Figure 4.3 using the impulse photoresponse shown in Figure 4.1c. The 3 dB bandwidth can be extracted and amounts to 17.8 MHz. When using the rise time of the square pulse photoresponse data, the 3 dB bandwidth can be approximated using Formula (4) and gives a value of 14.6 MHz. This is comparable to the bandwidth calculated via the impulse response data.

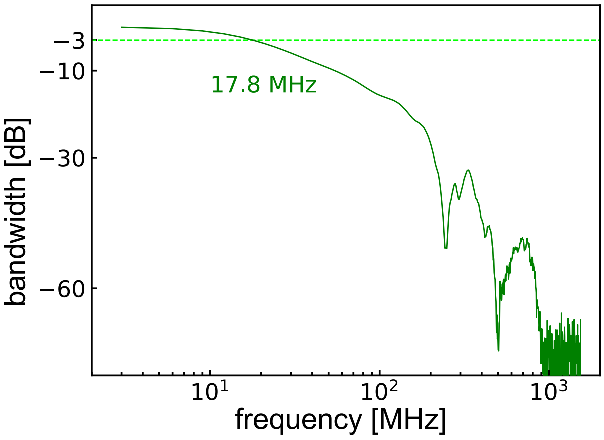

Figure 4.3. Bandwidth spectrum of the photodiode BPW 34 with its 3 dB bandwidth of 17.8 MHz.

4.4 Photoconductive and Photovoltaic Mode

The highest applicable voltage of 10 V limits the examination of the photodiode SFH 203 P which is characterized under a reverse bias of 20 V in the data sheet. The voltage dependence of the diode response towards both square pulse and impulse illumination is thus examined and shown in Figure 4.4. Without any biasing, in the photovoltaic mode, the rise and fall times are slowest and can be accelerated with increasing reverse bias, i.e., in the photoconductive mode.

As outlined in Chapter 2.1.1.2, this acceleration of the diode with increasing electric field can be attributed to a reduction of the RC time, an elimination of slow diffusion processes and to a shortened transit time: If the diode is not-fully depleted under photovoltaic conditions, its capacitance decreases with increasing reverse bias as the depletion width is extended. This also prevents diffusion processes. If charge carriers do not already travel at saturation velocity, it moreover accelerates their drift velocity. For a fully depleted diode, the acceleration of the diode with increasing applied field might arise if charge carriers are not yet travelling with saturation velocity, meaning that they can drift faster in a higher electric field.

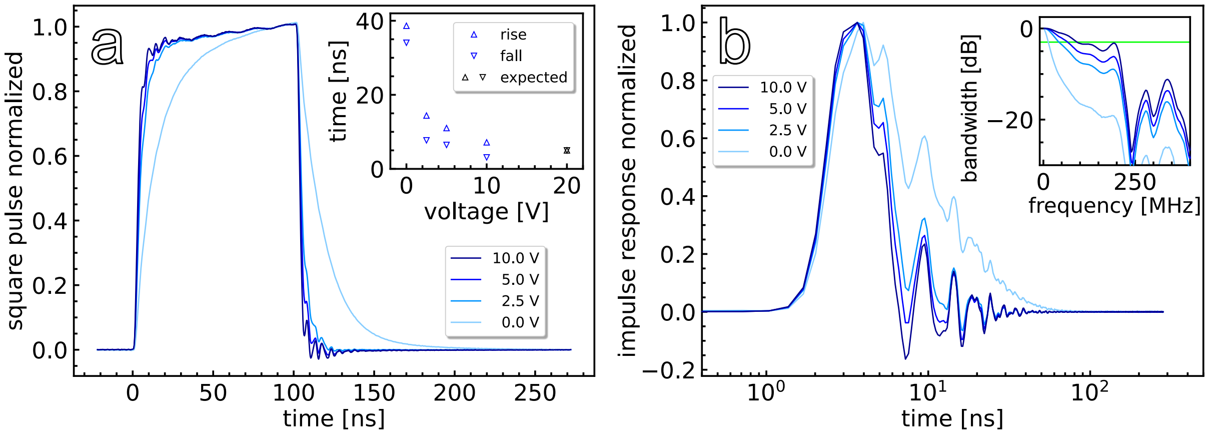

Figure 4.4. Voltage dependent rise and fall times of the commercial photodiode SFH 203 P under a) 635 nm 3 MHz square pulse illumination, pulse width = 100 ns, b) 636 nm 3 MHz impulse illumination, pulse width ≤ 500 ps. Inset: Corresponding bandwidth spectra.

5

Substrate Selection

Related Article

- Schedel, C.; Strauß, F.; Kumar, K.; Maier, A.; Wurst, K. M.; Michel, P.; Scheele, M., Substrate Effects on the Bandwidth of CdSe Quantum Dot Photodetectors. *ACS Appl. Mater. Interfaces* **2021,** *13* (40), 47954-47961.

Photodetectors are manufactured on a wide variety of substrates. Regularly used is a silicon wafer with insulating SiO_2 layer on top (Si/SiO_2)[17-20, 22, 23, 38, 134-136, 163, 246, 249, 267], including my own first experiments[197]. This allows for an electrical gating of the active material via the bottom silicon gate, cf. Chapter 2.1.2.3. Sometimes, hexagonal boron nitride[21, 230, 268] is applied additionally or another insulating layer instead of SiO_2, e.g. AlN[24], Al_2O_3[69, 111] or Si_3N_4[269], is utilized. In addition, glass[41, 90, 100, 102, 107, 133, 138, 144, 270], sapphire[33, 42, 161, 249, 271] and quartz[139] are used as substrates. For the design of flexible photodetectors, PET[38, 42, 140, 141, 271, 272], PEN[41, 42], polycarbonate[31] or polyimide[36] are reported.

However, hardly any study deals with the influence of the substrate material on the performance of a photodetector, especially with regard to its speed of response. [19, 22, 38, 41-43] In some cases, the substrate material used is not even specified,[13, 45] emphasizing how little attention has been devoted to this aspect in the development of photodetectors to date.

5.1 Si/SiO_2

I started investigations of photodetectors based on Si/SiO_2[197] wafers and planned to exploit the possibility of an electrical gating of the devices in addition to optical gating with laser illumination. However, when examining a bare silicon wafer with 230 nm oxide (Si/SiO_2(230 nm)) and interdigitated gold electrodes on top, a signal towards both, vis square pulse and vis impulse illumination, can be detected as shown in Figure 5.1. Under 635 nm square pulse illumination, a response of the bare substrate towards the on- and off-switching of the laser is visible in both source-drain current (I_{SD}) and leakage current (I_{SG}), when the wafer is investigated with a system source meter, cf. Figure 5.1a. The exact, time-resolved photoresponse measured with the setup developed in this work towards both 635 nm square pulse and 636 nm impulse illumination shows a significant photocurrent response lasting up to microseconds, cf. Figures 5.1b and 5.1c, respectively. In contrast, no measurable photoresponse is present in studies using 1310 nm square pulse illumination, cf. Figure 5.1d.

These photoresponses can be attributed to an absorption of the incident illumination by the underlying silicon. Silicon has a high absorption coefficient in the visible range (about $10^4 - 10^5$ $\mathrm{cm^{-1}}$), while it hardly absorbs at all when excited below its band gap of 1.1 eV. This is still the case when it is n-doped with a concentration of $3 \cdot 10^{17}$ $\mathrm{cm^{-3}}$ (cf. Chapter 3.6.2).[273-275] A recommendation that a silicon wafer should not be used as substrate material for photodetectors because of its absorption is also given in the thesis of C. Livache.[276]

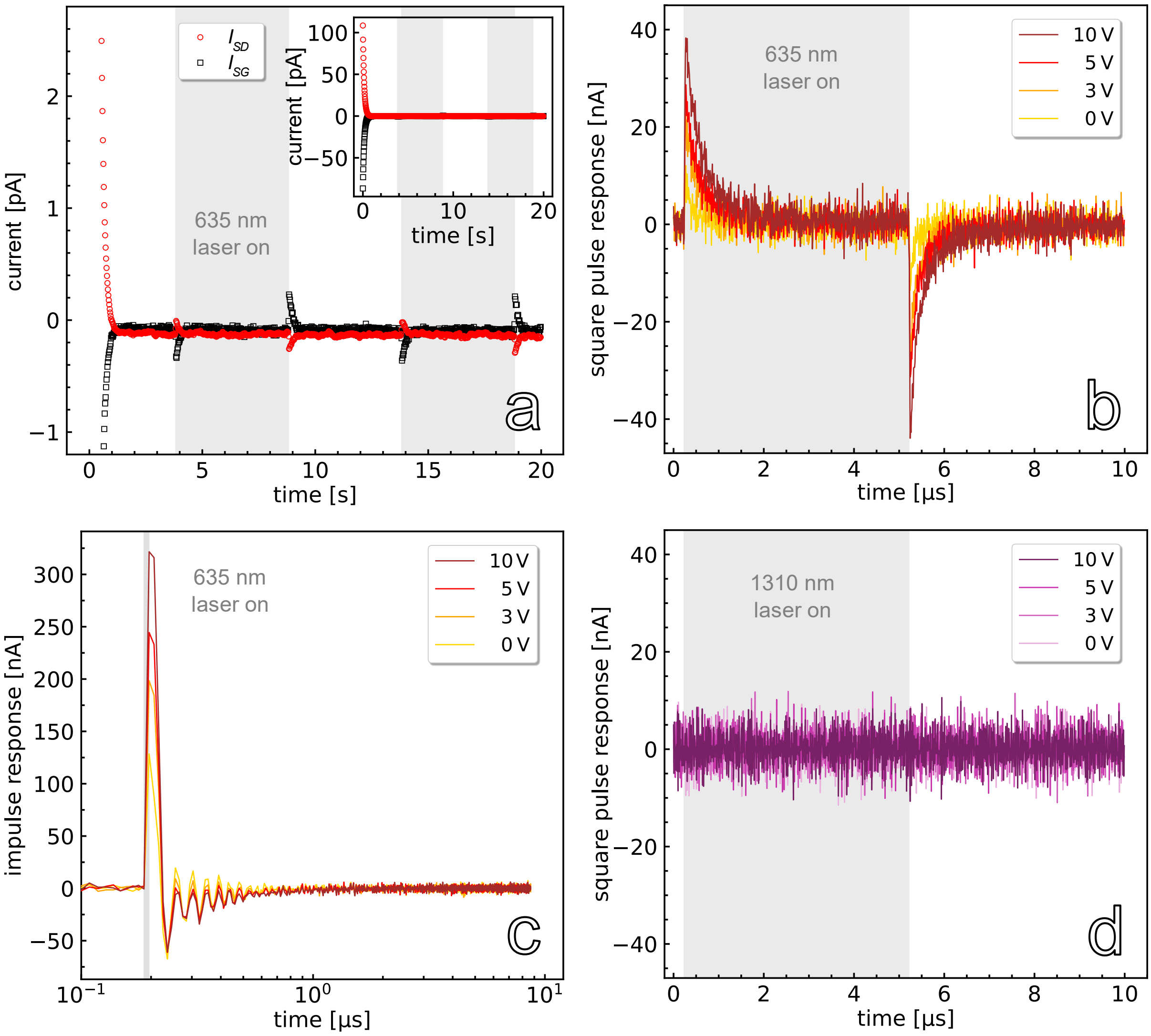

Figure 5.1. Typical photoresponse of a bare Si/SiO2(230 nm) substrate with interdigitated gold electrodes on top (here: 2.5 µm × 10 mm). a) Source-drain current (I_{SD}) and leakage current (I_{SG}) measured with a system source meter for 200 mV applied under 635 nm 0.1 Hz square pulse illumination. Inset: full response, including the capacitive drop at the beginning of the measurement. More detailed investigation with the time-resolved measurement setup: b) Square pulse photoresponse upon 635 nm 100 kHz illumination, under different voltages applied. Adapted with permission from Schedel et al.[49] and modified. Copyright 2021, American Chemical Society. c) Impulse photoresponse upon 636 nm 100 kHz illumination, under different voltages applied. Adapted with permission from Schedel et al.[49] and modified. Copyright 2021, American Chemical Society. d) Square pulse photoresponse upon 1310 nm 100 kHz illumination, under different voltages applied. Grey boxes indicate laser illumination.

To investigate if this silicon signal is significant compared to the photoresponse of an entire photodetector with an active material deposited on top of the silicon substrate, CdSe/I$^-$/Zn4APc thin films on Si/SiO2(230 nm) were investigated. Both empty substrates and CdSe/I$^-$

/Zn4APc coated substrates were studied with 636 nm 500 kHz impulse illumination (≤ 110 µW average power) and different biases applied. They are compared concerning the magnitude of their photoresponse, shown in Figure 5.2. The voltage dependent maximum photocurrent towards the impulse illumination is given and no differentiation between silicon substrates with (blue) and without (red) photoactive material is possible. Therefore, the photoresponse of a Si/SiO$_2$(230 nm) substrate cannot be neglected and seems to dominate the measurement.

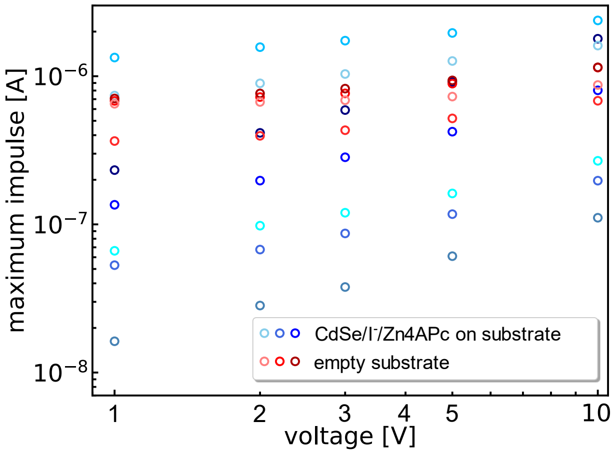

Figure 5.2. Comparison of the voltage dependent maximum impulse photocurrent of a Si/SiO$_2$(230nm) wafer with 2.5 µm × 10 mm electrode geometry without (red, one color = one device) and with (blue, one color = one device) CdSe/I$^-$/Zn4APc thin film on top.

A thicker dielectric layer should protect the gold electrodes more effectively from charging effects induced by photogenerated charge carriers in the underlying silicon. Therefore, silicon substrates with an extemely thick oxide layer, Si/SiO$_2$(770 nm), have been examined, cf. Figure 5.3. While the empty substrate does not feature any photoresponse towards square pulse illumination, see Figure 5.3a, charging effects are observed again in the leakage current of a WSe$_2$ photodetector based on Si/SiO$_2$(770 nm), see Figure 5.3b. Detailed investigations are performed with the time-resolved measurement setup and three exemplary measurements, that reflect the possible magnitudes of the effect, are given in Figure 5.3c. Depending on the applied electric field, the magnitude of the leakage current (I_{SG}) varies and it can be as high as the measured photocurrent. With that, it has a strong impact on the temporal performance of the detector when switching the laser on and off.

Since this thesis focuses on the speed of response of photodetectors and the measurement of time-resolved photocurrents under visible and NIR illumination, the use of Si/SiO$_2$ substrates is avoided.

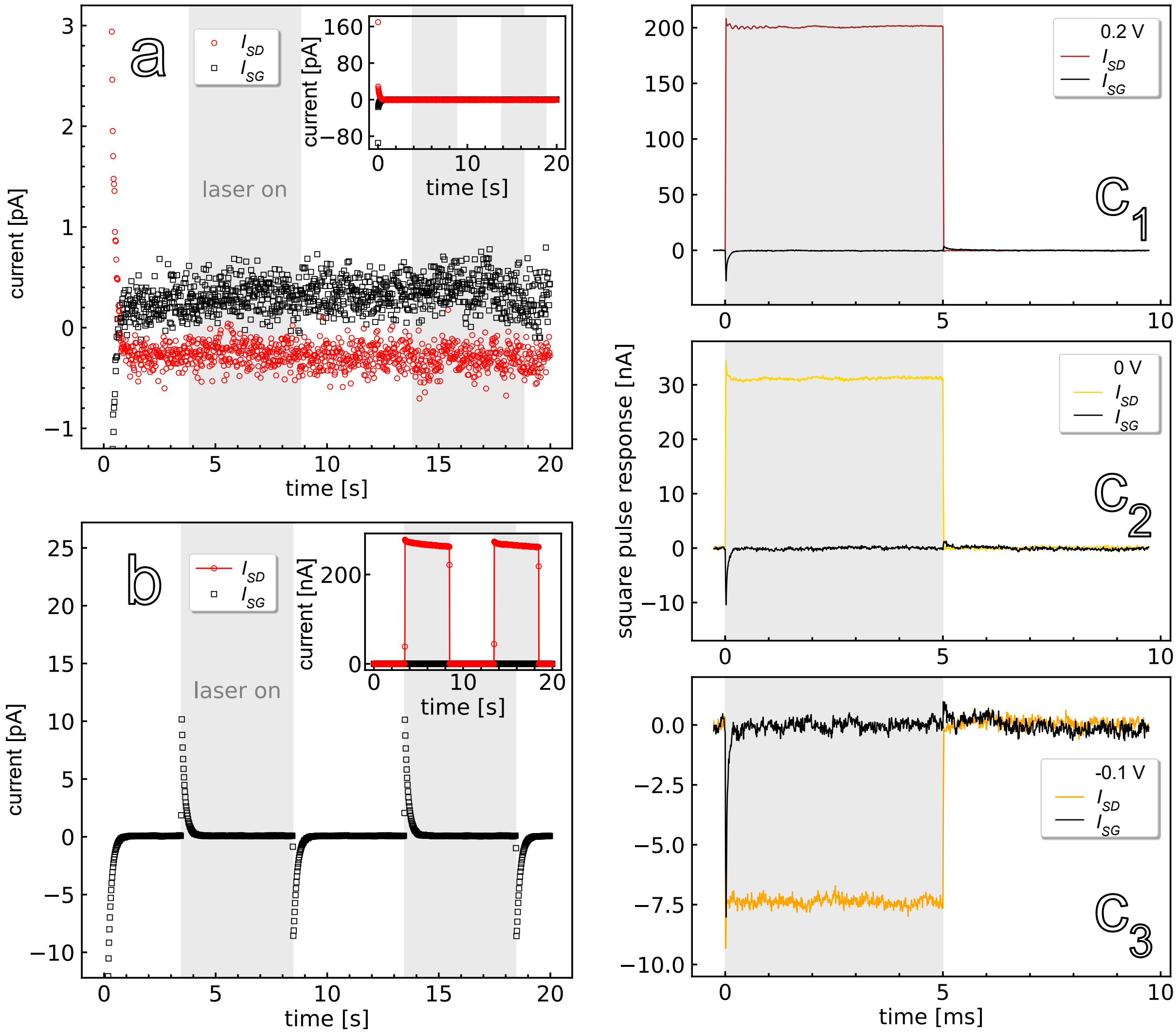

Figure 5.3. Typical Si-substrate signal for a Si/SiO$_2$(770 nm) substrate with gold electrodes on top under 635 nm square pulse illumination. a) Bare substrate with 2.5 µm × 10 mm interdigitated gold electrodes, examined with the system source meter under 200 mV bias applied, 0.1 Hz illumination. Inset: full response, including the capacitive drop at the beginning of the measurement. b) Leakage current (I_{SG}) of a WSe$_2$ photodetector based on Si/SiO$_2$(770 nm) with 2.5 µm × 80 µm gold electrodes, examined with the system source meter for 200 mV bias applied, 0.1 Hz illumination. Inset: full photoresponse. c) Detailed study of the same sample as in (b) with the time-resolved measurement setup, under different voltages applied at 100 Hz illumination.

5.2 Glass and Polyimide

There are many insulating materials that do not absorb in the vis (636 nm) and NIR (779 nm, 1310 nm) range and that could be used as substrates. Glass with a high dielectric constant of 4.5-8[277] is utilized frequently. For the fabrication of electrodes via optical lithography, the surface of glass must be modified with an adhesion promoter. Hexamethyldisilazane (HMDS) is used and minimizes the density of silanol groups at the surface, preventing electron trapping and scattering at the interface between glass and photoabsorber.[182, 278-280] A representative of flexible substrates is poly(4,4'-oxydiphenylene pyromellitimide), a polyimide, which has a low dielectric constant of 3.5-3.7[281, 282]. The dependence of the dielectric constant on the frequency in the range of 50 Hz up to 1 MHz is very small for both glass[277] and polyimide[281], and the dielectric constant is therefore assumed to be constant in this range in the following investigations. The surface of HMDS treated glass and the utilized polyimide, also called Kapton® HN, are shown in Figure 5.4.

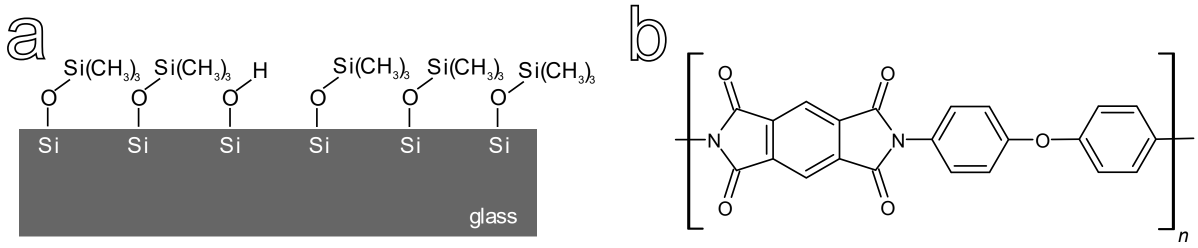

Figure 5.4. a) HMDS treated glass surface, b) chemical structure of the polyimide Kapton® HN.

The largest differences in the charging energy of QDs occur for a dielectric constant of the matrix of up to approx. ten, as shown in the case of PbSe QDs, cf. Figure 2.12.[244] A similar trend regarding the influence of the substrate can be expected and the dielectric constants of the two substrates with 4.5-8 for glass vs 3.5-3.7 for polyimide fit perfectly to this range.

In order to confirm that glass and polyimide can be used as substrate materials in the development of photodetectors, they are investigated like Si/SiO_2 before. This is shown in Figure 5.5. Neither on glass nor on polyimide there is a leakage current in the photoresponse of WSe_2 detectors, both for an investigation with the system source meter and for the detailed investigations with the developed time-resolved photocurrent setup. Therefore, these two materials are used as substrate materials in the following time-resolved photocurrent studies.

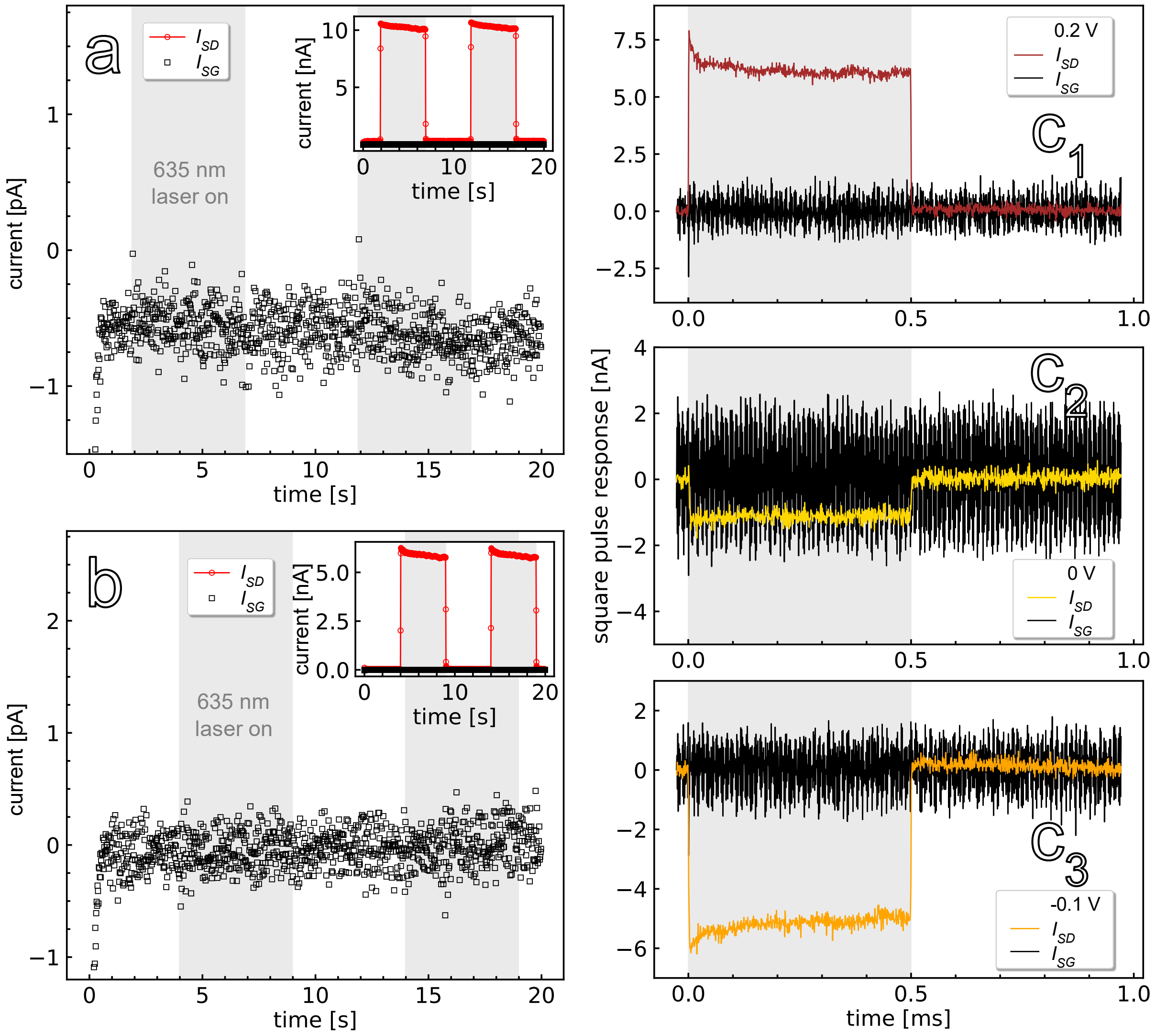

Figure 5.5. Typical leakage currents of WSe_2 flakes on top of 5 µm × 80 µm gold electrodes on a) glass and b) polyimide, under 635 nm 0.1 Hz square pulse illumination and 200 mV bias applied, examined with the system source meter. Insets: Corresponding photocurrents. c) Detailed investigation of the same sample as in (b) with the time-resolved measurement setup for varying biases applied under 635 nm 1 kHz illumination.

The root mean square surface roughness (RMS roughness) of both substrates is investigated with atomic force microscopy, shown in Figure 5.6. HMDS treated glass slides show a smooth surface with a roughness of 5.5 ± 0.8 nm. On the contrary, polyimide shows large elevations and scratches are present which presumably originate from manufacturing and package of the foil. It has a higher surface roughness of 30.7 ± 12.9 nm.

The characteristics of glass and polyimide are listed in Table 5.1 for comparison.

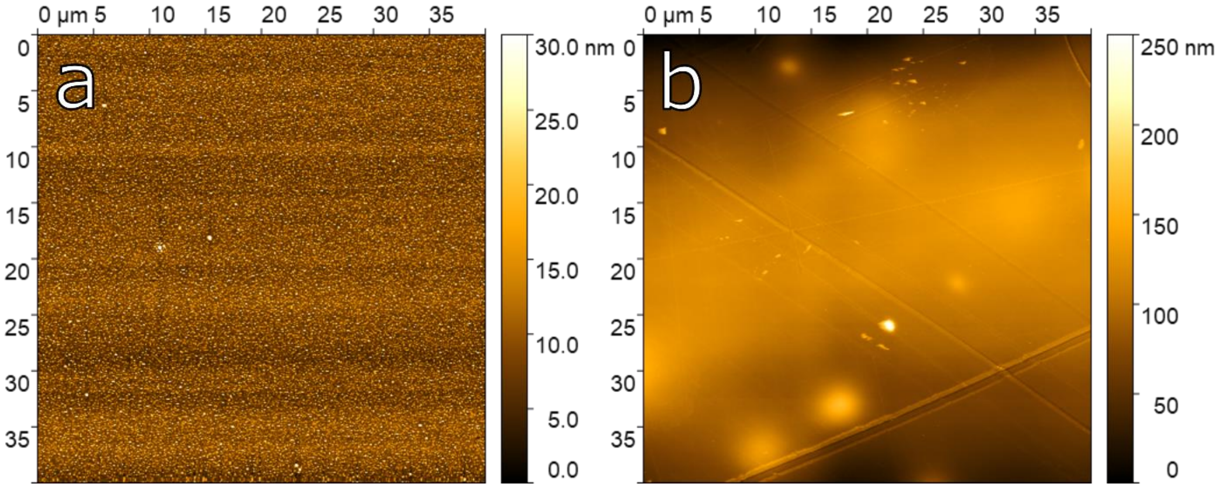

Figure 5.6. AFM image of bare a) glass slide, b) polyimide foil.

Table 5.1. Characteristics of glass and polyimide.

	glass	**polyimide**
surface roughness	5.5 ± 0.8 nm	30.7 ± 12.9 nm
dielectric constant	4.5-8 [277]	3.5-3.7 [281, 282]

6

Substrate Effects on the Bandwidth of CdSe Quantum Dot Photodetectors

Related Article

- Schedel, C.; Strauß, F.; Kumar, K.; Maier, A.; Wurst, K. M.; Michel, P.; Scheele, M., Substrate Effects on the Bandwidth of CdSe Quantum Dot Photodetectors. *ACS Appl. Mater. Interfaces* **2021,** *13* (40), 47954-47961.

In this Chapter, the time-resolved photoresponse of iodide capped CdSe QD thin films, sensitized with the dye zinc β-tetraaminophthalocyanine, (CdSe/I$^-$/Zn4APc) on both glass and polyimide substrates is examined. Both 636 nm and 779 nm impulse illumination and 635 nm square pulse illumination are investigated. The transient, non-steady state photocurrent response of a detector under impulse illumination gives information about its application in fast optical switches for optical communication, where very short, delta-shaped laser impulses are exploited for data transmission. The photocurrent response towards a square pulse illumination reaching steady state photocurrents can be used to examine if geometry related (dis-)charging limits the speed of the detector.

For the same thin films, the use of polyimide as substrate for CdSe/I$^-$/Zn4APc photodetectors enables the larger bandwidth of 85 kHz vs. 67 kHz when glass is utilized. As is evident from the transient response to an impulse illumination, the initial carrier trapping and recombination within about 2.7 ns is identical on both substrates, whereas a long tail caused by multiple trapping events is more pronounced on glass, thus reducing the bandwidth. For the steady state investigations, no difference is observed in the decay for either substrate, which indicates that all trap states are saturated during the long illumination time, thus, a comparable decay behavior emerges. All devices are RC limited and to improve the bandwidth, the photoresistance of the QD thin film must be reduced.

6.1 Non-Steady State ("Impulse") Investigations

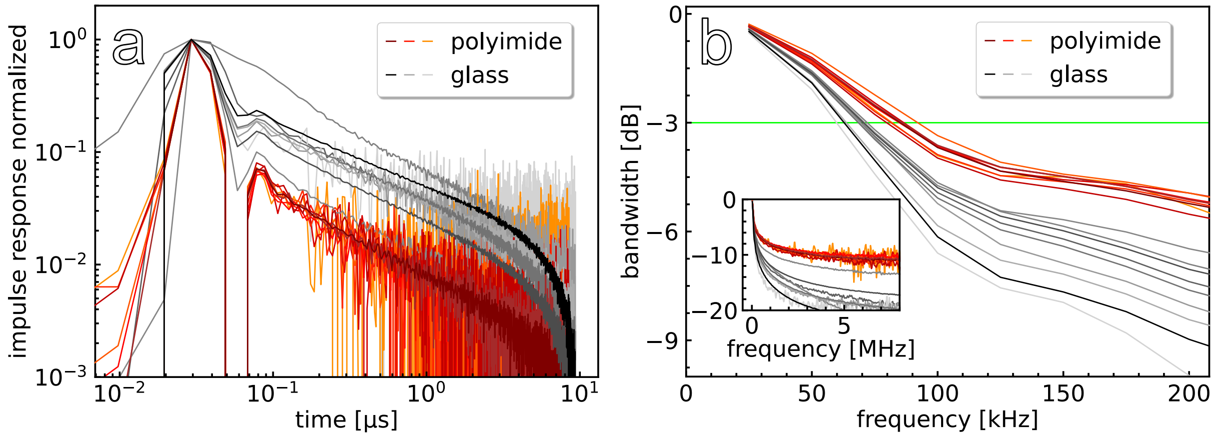

Figure 6.1. a) Normalized transient photocurrent responses of CdSe/I$^-$/Zn4APc thin films with µm-spaced electrodes on glass (black) and polyimide (red) under 636 nm 100 kHz illumination with 10 V bias applied (one color = one device). The 100 kHz measurement window corresponds to a 9.8 ns time / point resolution. b) Corresponding bandwidth spectra of the impulse responses given in (a) calculated via Formula (4). Zero-padding is applied to the impulse measurements to convert the 100 kHz data into quasi 25 kHz data. The bandwidth is approx. 67 ± 4 kHz on glass and 85 ± 4 kHz on polyimide. Inset: larger section of the bandwidth spectra. Adapted with permission from Schedel et al.[49] and modified. Copyright 2021, American Chemical Society.

The speed of response of the CdSe/I$^-$/Zn4APc photodetectors are first investigated using impulse illumination. The normalized impulse photocurrent responses of CdSe/I$^-$/Zn4APc thin films on µm spaced electrodes on glass, depicted in black, and on polyimide, depicted in red, are shown in Figure 6.1a for 636 nm 100 kHz illumination (≤ 22 µW average output power). A distinct difference is visible in the long tail of the transient response. The tail current is significantly enhanced on glass compared to polyimide and a fall time (90 % – 10 %) of 160 ± 128 ns on glass vs. 18 ± 3 ns on polyimide is observed. According to Formula (4), these impulse responses translate into 3 dB bandwidths of 67 ± 4 kHz on glass and 85 ± 4 kHz on polyimide, cf. Figure 6.1b.

Regardless of the applied voltage and the channel length (electrode geometry: 2.5 µm, 5 µm, 10 µm, 20 µm × 10 mm), the normalized photoresponses are the same on glass and polyimide, see Figure 6.2. This is true for both 636 nm and 779 nm illumination with a reduction of the photocurrent response under NIR illumination of 50 % – 80 % compared to the photocurrent induced by 636 nm illumination. The lack of dependence of the signal on bias or channel length opposes the behavior observed for an organic photodetector by Punke et al.[77] It implies that the CdSe/I$^-$/Zn4APc detectors are not transit time limited, where an increasing electric field accelerates charge carrier drift and a shorter channel length leads to reduced drift times, both effects speeding up the photoresponse, cf. Formula (15).

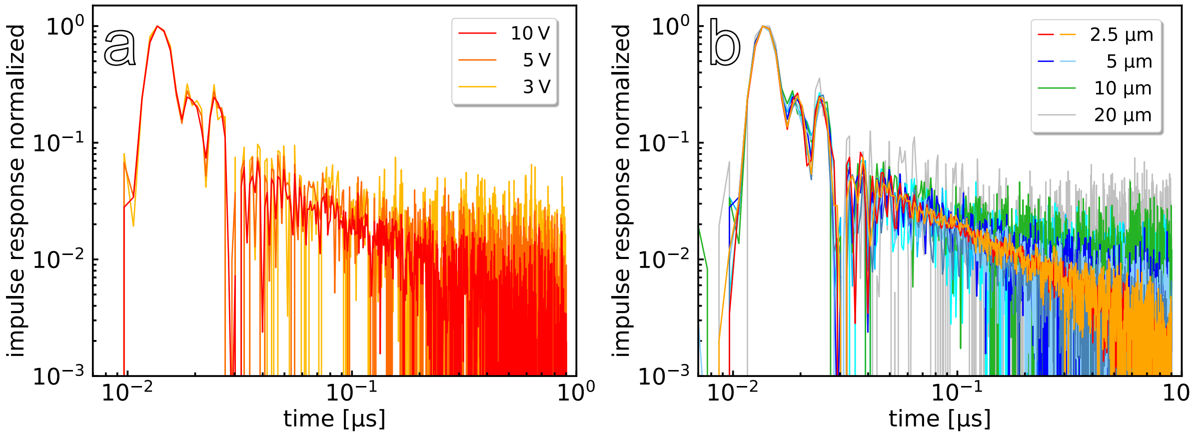

Figure 6.2. Normalized impulse responses of a typical CdSe/I$^-$/Zn4APc thin film on polyimide upon 636 nm 1 MHz illumination with a) different electric fields applied (5 µm channel length), and with b) different channel lengths under 10 V bias applied. Adapted with permission from Schedel et al.[49] and modified. Copyright 2021, American Chemical Society.

The decay of the impulse response can give insights into the decay mechanisms of photoinduced charge carriers in the QD film and two models can be applied, cf. Chapter 2.1.3.1. On short timescales for the fast initial decrease, an exponential decay ($\propto e^{-\frac{t}{\tau}}$) can be attributed to charge carrier recombination and initial trapping. This is followed by a slower decay following a power law ($\propto t^m$) according to a multiple trapping and release mechanism.

Both mechanisms are observable in the transient photocurrent decay of the CdSe/I⁻/Zn4APc thin films, similar to previous reports[25, 139-144], and exemplary fits can be seen in Figure 6.3.

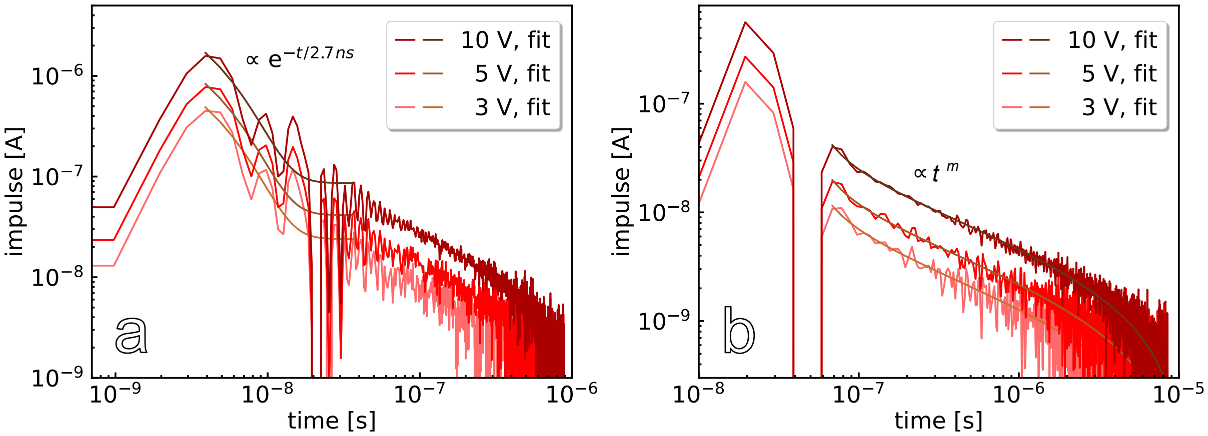

Figure 6.3. Impulse response of a typical polyimide detector under 636 nm illumination (channel length: 2.5 µm). a) Initial decay of the photoresponse shown for 1 MHz repetition rate data with exponential fits ($\propto e^{-\frac{t}{2.7\,\mathrm{ns}}}$) and b) power law fits ($\propto t^m$, $m_{10\mathrm{V}} = -0.47 \pm 0.01$, $m_{5\mathrm{V}} = -0.47 \pm 0.02$, $m_{3\mathrm{V}} = -0.49 \pm 0.03$) of the long tail carried out at 100 kHz illumination for a better visualization of the tail. Adapted with permission from Schedel et al.[49] and modified. Copyright 2021, American Chemical Society.

The exponential fit ($\propto e^{-\frac{t}{\tau}}$) of the first decay gives a time constant (τ) of 2.7 ns for all devices on both polyimide and glass regardless of the applied bias and the channel length, cf. Figure 6.3a. This time constant fits to both the thin film photoluminescence data and to the theoretical hopping time. According to previous results[197], the photoluminescence decay is estimated to be 3.1 ns or faster, depending on the film thickness. The hopping time (τ) expected for such QDs is about 2.1 ns, calculated with $\tau = \frac{ed^2}{6\mu kT}$,[98, 238, 283] using the mobility $\mu = 10^{-3}\ \mathrm{cm}^2/\mathrm{Vs}$ as previously determined on a Si/SiO₂ wafer[197] and the QD diameter (d). Therefore, I attribute the first exponential decay to charge carrier recombination and initial trapping.

The initial exponential decay is followed by a slower decay that obeys a power law behavior ($\propto t^m$). This corresponds to the characteristic encountered for multiple trapping and release of charge carriers, and the Urbach energy (E_U) gives an estimate for the distribution of the trap states being incrementally filled. For all samples, the exponent of the power law fit (m) is $-0.6 \leq m \leq 0$, thus, the Urbach energy is estimated according to $E_U = \frac{k_B T}{m+1}$, cf. Formula (26).[140, 145, 146, 149-151, 153] For the polyimide devices, the mean of the Urbach energies is about 50 meV and on glass it is about 44 meV, see Figure 6.4. A trend towards decreasing Urbach energy with increasing electric field seems to exist, although most variations are within the standard deviation. The enhanced tail currents for the detectors on glass lead to improved signal to noise ratios, explaining the smaller standard deviation of the glass detectors compared to the polyimide devices.

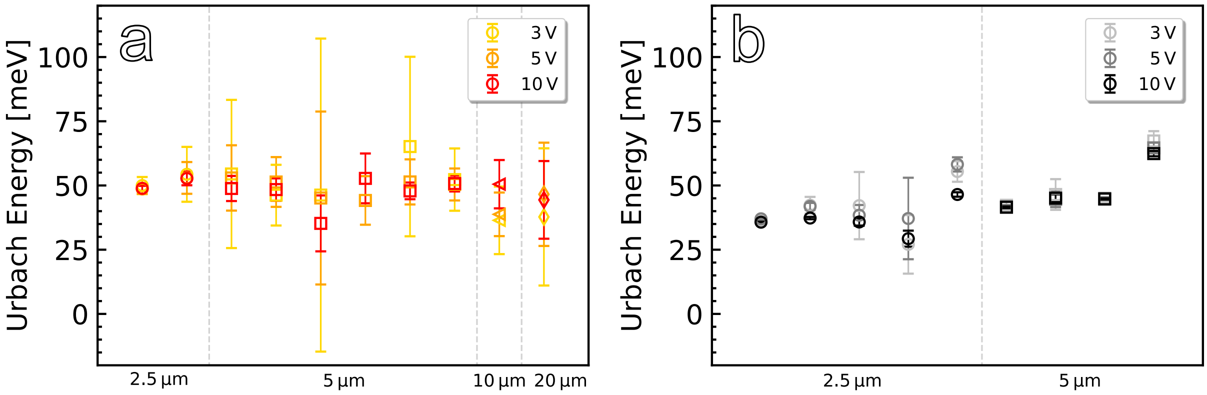

Figure 6.4. Urbach energies of a) polyimide and b) glass photodetectors, x-axis: electrode gap (2.5 µm, 5 µm, 10 µm, 20 µm × 10 mm), contacts listed. Adapted with permission from Schedel et al.[49] Copyright 2021, American Chemical Society.

Previously reported values of the Urbach energy for CdSe QDs are approx. 20 – 80 meV, depending on the chosen surface ligand and film preparation.[99] They are in accordance with the values measured in this work. Taking into account the standard deviation, the Urbach energies on glass and polyimide are approximately the same, thus, this aspect cannot explain the distinct differences in the tail of the photocurrent. Instead, I attribute it to a larger number of accessible trap states of similar energy at the QD – substrate interface for glass detectors compared to polyimide devices. The dielectric constant of technical glass with 4.5-8[277] influences the charging energy of the QDs close to the substrate, cf. Formula (34), where the enhanced dielectric screening shields trapped charge carriers more effectively compared to the situation on polyimide with a small dielectric constant of 3.5-3.7[281, 282]. Thus, more QD trap states near the interface can be occupied on glass, enhancing the tail current due to the more pronounced multiple trapping and release process.

6.2 Steady State ("Square Pulse") Investigations

The photoresponse of a typical CdSe/I$^-$/Zn4APc thin film on polyimide with µm-sized electrode gaps towards 635 nm 10 Hz square pulse illumination (≤ 12 mW) is shown in Figure 6.5. The same stable photocurrents are observed at longer illumination times, e.g., under 0.1 Hz illumination, thus, steady state conditions are achieved. No difference between glass and polyimide detectors is observed, contrary to E et al.[42] The rise times (10 % – 90 %) range mostly from 0.4 ms to 4.8 ms, cf. Figure 6.8, and fall times vary between 0.2 ms to 4.2 ms. The scattering arises due to inhomogeneities in the morphology and the thickness of the films, which are up to about 3 – 4 µm thick, cf. Chapter 3.6.3.

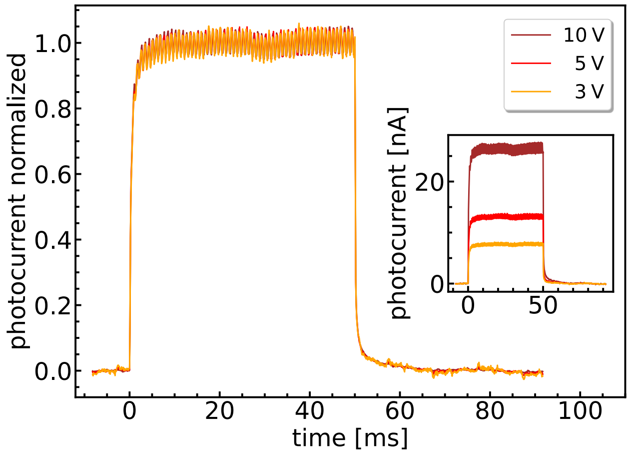

Figure 6.5. Normalized square pulse photocurrent response of a typical CdSe/I$^-$/Zn4APc thin film towards 635 nm 10 Hz illumination at different applied voltages. Exemplary device on polyimide with 5 µm channel length. Inset: absolute photocurrent. Adapted with permission from Schedel et al.[49] Copyright 2021, American Chemical Society.

I ascribe the comparable decay behavior to the long illumination times during which all trap states are saturated, and detectors based on glass and polyimide can no longer be distinguished from each other. Identical to impulse illumination, there is neither a measurable field nor channel length dependence of the rise and fall times. This argues against a transit time limitation of the devices since drift should be accelerated by an increased electric field. According to Formula (15), the theoretically expected drift times for the four geometries with 2.5 µm, 5 µm, 10 µm or 20 µm channel length, using $\mu = 10^{-3}\mathrm{cm}^2/\mathrm{Vs}$[197] and 10 V bias applied, are 6.3 µs, 25 µs, 100 µs and 400 µs, respectively, values that are significantly lower than the measured rise times. Moreover, diffusion processes should be accelerated with an enhanced electric field as well. Therefore, this behavior hints towards an RC limitation of the detectors.

To verify the assumed RC limitation, I conducted impedance spectroscopy on the photodetectors on polyimide to estimate the RC time and compared it with the measured rise times. An exemplary impedance spectrum is shown in Figure 6.6 for a 2.5 µm channel length device. The data is fitted assuming a parallel circuit consisting of a constant phase element and a resistor, similar to Livache et al.[133]

The resistances extracted from the impedance measurements are identical to the ones measured via two-point measurements, as shown in Figure 6.7a. For the two-point measurements, an ohmic behavior of the devices was observed up to ± 10 V. I checked the measured capacitances with the theoretically expected values calculated according to Formula (23): $C = L(N-1)\varepsilon_0(1+\varepsilon_r)\frac{K(k)}{K(k')}$,[116] using the dielectric constant of CdSe QDs ($\varepsilon_r = 6.2$)[187, 232], the number of electrode fingers ($N = 21$), the length of the electrode fingers ($L = 500$ µm), and the width of the electrode fingers (w = 20 µm). With that, I assume the device capacitance to be about 1.3 pF, 1.0 pF, 0.8 pF and 0.6 pF for the channel lengths of 2.5 µm, 5 µm, 10 µm, and 20 µm, respectively. These calculated values are compared to the values determined via impedance measurements in Figure 6.7b and show a good agreement.

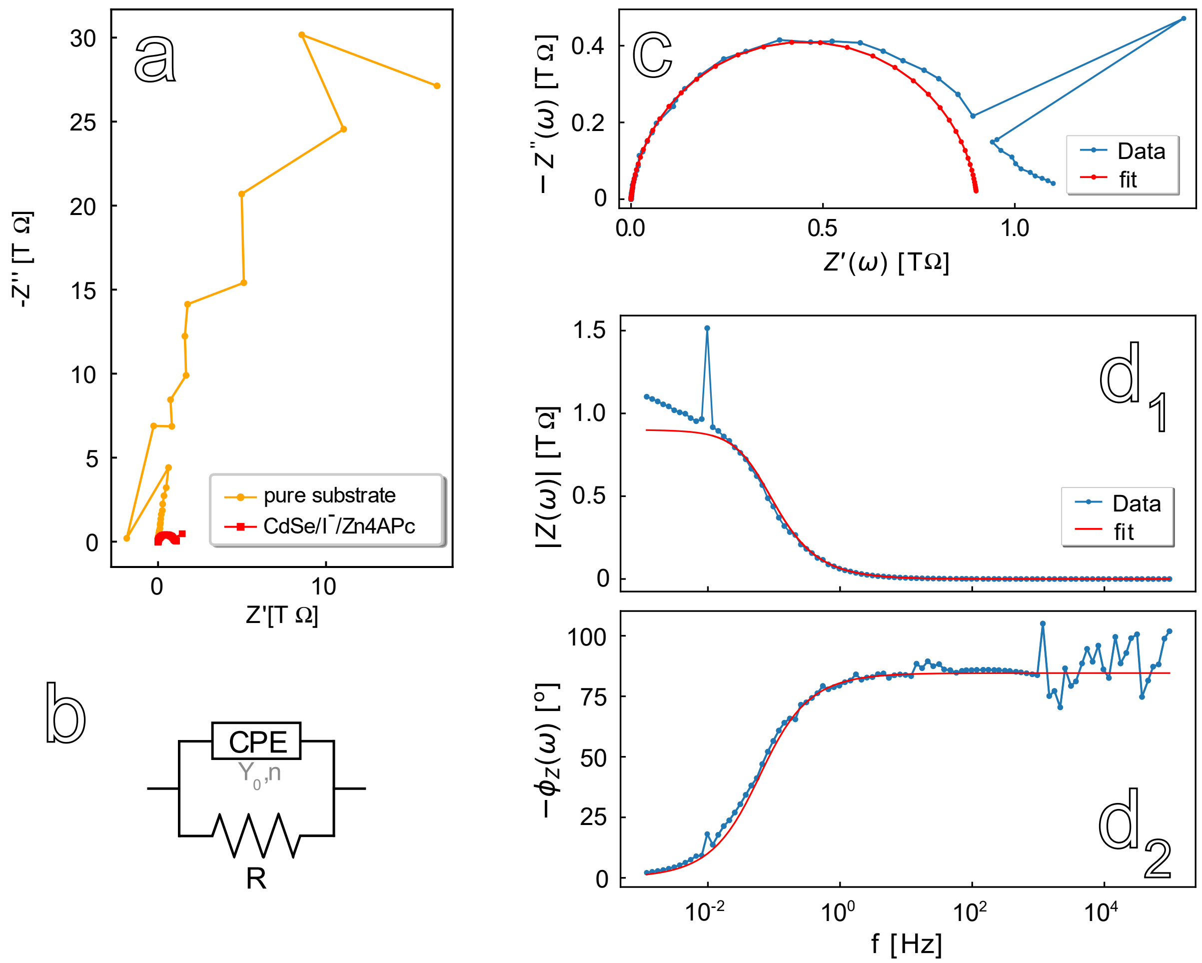

Figure 6.6. Exemplary impedance spectra of a polyimide detector with 2.5 µm channel length. a) Cole-Cole plot of an uncoated (orange) vs. CdSe/I$^-$/Zn4APc coated (red) polyimide substrate. b) Assumed equivalent circuit: parallel circuit of a constant phase element (Y_0, n) and a resistor (R). c) Cole-Cole plot of the CdSe/I$^-$/Zn4APc thin film on polyimide shown in (a) with the corresponding fit assuming the equivalent circuit given in (b). $R = 9.0 \cdot 10^{11}\ \Omega, Y_0 = 2.73 \cdot 10^{-12}\frac{s^n}{\Omega}, n = 0.94 \rightarrow C_{eff} = 2.89 \cdot 10^{-12}$ F. d) Corresponding Bode plots of the data shown in (c), including the fits. Adapted with permission from Schedel et al.[49] and modified. Copyright 2021, American Chemical Society.

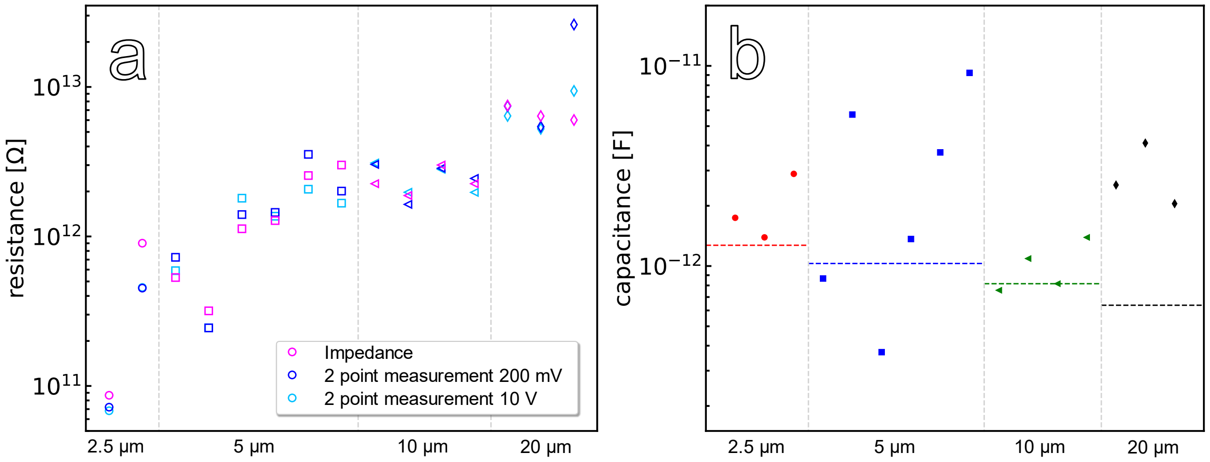

Figure 6.7. a) Resistances of the polyimide detectors determined via both impedance (magenta) and two-point measurements (blue, for two different voltage regimes). b) Capacitances of the devices. Theoretically calculated values are shown by dashed lines, measured values of the polyimide devices are shown with markers. x-axis: electrode gap (2.5 µm, 5 µm, 10 µm, 20 µm × 10 mm), contacts listed. Adapted with permission from Schedel et al.[49] and modified. Copyright 2021, American Chemical Society.

Based on that, the RC times are calculated and compared to the measured rise times in Figure 6.8. The RC time evaluated by impedance spectroscopy in the dark (magenta) is several orders of magnitude slower than the measured rise times (red) under all voltages applied. An excellent agreement of RC time and rise time, on the other hand, is obtained when the photoresistance (R_{illum}) is used for the calculation of the $R_{illum}C$ time (blue).

The necessity to consider the photoresistance in the determination of the RC time can be understood assuming that the resistance adapts very quickly under illumination. With that, the $R_{illum}C$ time is closer to the time constant actually present in the film at any time of the measurement. The capacitances of 1 – 10 pF are very small but due to the high QD film resistances the RC time becomes significant. Therefore, the observed rise times of all detectors of hundreds of microseconds to several milliseconds are not an intrinsic property of the material but are due to capacitive (dis-)charging of the device.

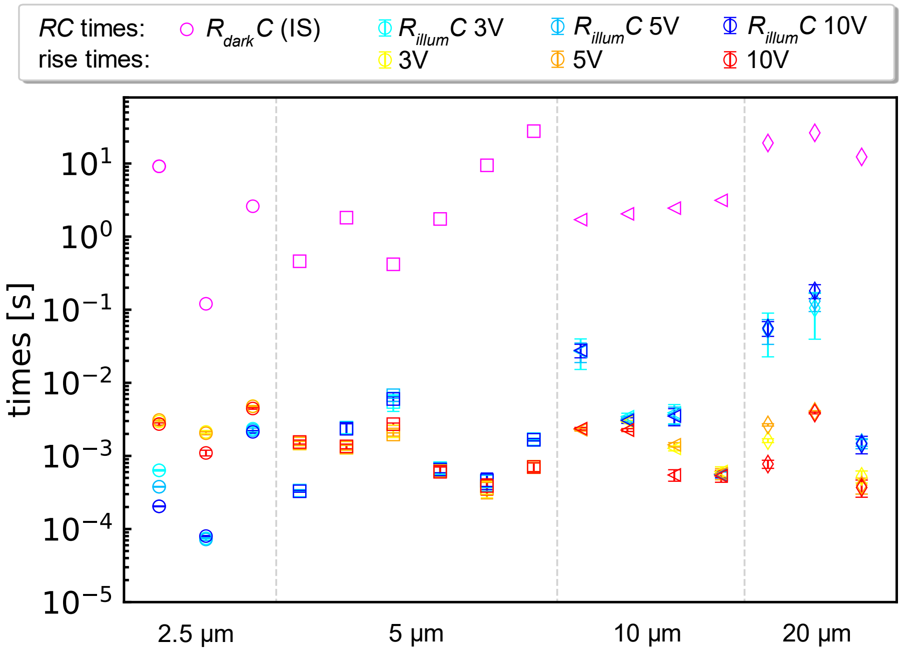

Figure 6.8. Time constants of the CdSe/I⁻/Zn4APc thin films on polyimide. Comparison of the RC time evaluated by impedance spectroscopy (IS) in the dark (magenta) with the $R_{illum}C$ time of the devices under illumination (blue) and the measured rise times (red). x-axis: electrode gap (2.5 µm, 5 µm, 10 µm, 20 µm × 10 mm), contacts listed. The three devices with significantly higher $R_{illum}C$ times compared to the corresponding rise times can be considered outliers since they showed very low photocurrents leading to an uncertainty in the evaluated data. Adapted with permission from Schedel et al.[49] and modified. Copyright 2021, American Chemical Society.

6.3 *RC* time reduction

To accelerate the photodetectors, the RC time must be reduced. With a shortened channel length of 350 nm and 500 nm the dark resistance is improved to approx. $10^{9} - 10^{11}\Omega$, see Figure 6.9. Glass detectors with this electrode geometry (350 nm, 500 nm × 10 mm), from now on referred to as "nm glass" devices, are investigated and compared to the first two categories discussed so far, referred to as "µm polyimide" and "µm glass" devices.

For the nm glass devices, rise times of the square pulse photoresponse down to 24 µs can be achieved due to a reduced photoresistance. The correlation between the rise time and the photoresistance is shown in Figure 6.10a for both µm and nm glass devices, depicted in black and blue, respectively: The rise time is accelerated with a smaller photoresistance. A trend of faster rise times for the nm devices compared to the µm devices is visible with the same rise times for both groups of detectors when the same photoresistance is obtained. In Figure 6.10b, the photoresponse of a typical CdSe/I⁻/Zn4APc thin film with varying absolute photocurrents upon 635 nm 100 Hz square pulse illumination is shown, using a 350 nm channel length glass substrate. The lower photoresistance caused by the higher photocurrent leads to the faster speed of response of the device under otherwise identical conditions.

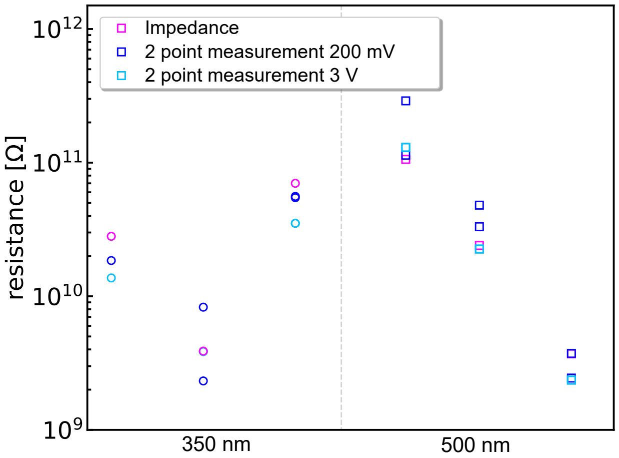

Figure 6.9. Resistances of the nm glass detectors determined via both impedance (magenta) and two-point measurements (blue, for two different voltage regimes), x-axis: electrode gap (350 nm, 500 nm × 10 mm), contacts listed. Adapted with permission from Schedel et al.[49] and modified. Copyright 2021, American Chemical Society.

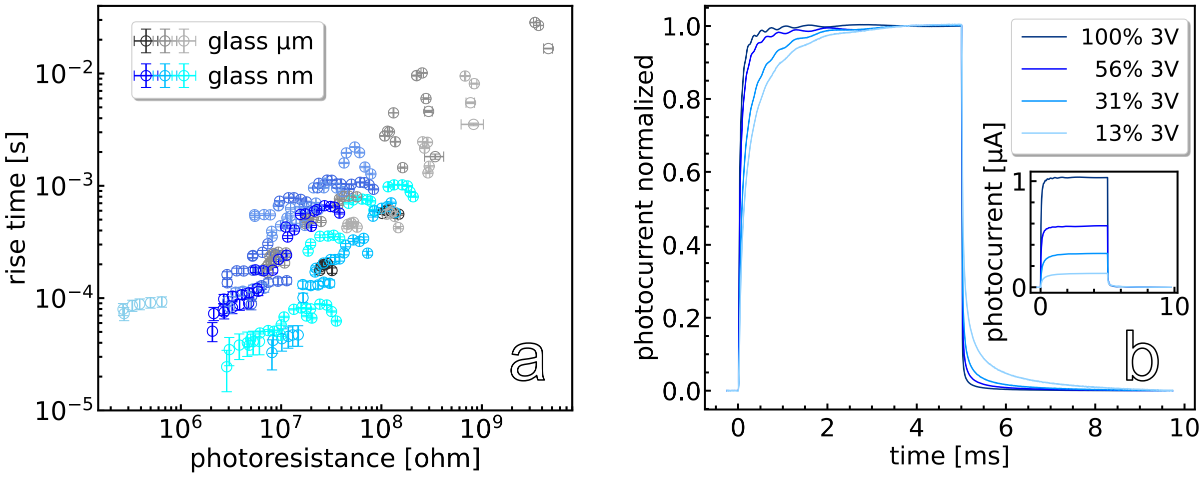

Figure 6.10. a) Correlation between rise time and photoresistance of both µm- and nm-spaced CdSe/I⁻/Zn4APc photodetectors on glass (one color = one device). b) Typical normalized photoresponse of a device on glass for 3 V bias applied towards 635 nm 100 Hz square pulse illumination with different laser intensities, thus, different absolute photocurrents (350 nm channel length). Inset: Absolute photocurrent. Adapted with permission from Schedel et al.[49] Copyright 2021, American Chemical Society.

These results imply that the devices are still RC limited, which is confirmed as the nm devices do not show a field dependence of the rise times (analogous to Figure 6.5 for the µm devices) and the calculated RC times using impedance data are in accordance with the measured rise times (analogous to Figure 6.8 for the µm devices). For further improvement of the photodetectors, the high resistance of QD films must be significantly reduced and much work is already conducted to improve the mobilities of such films for a better applicability in optoelectronic devices.[283, 284]

Using non-steady state illumination, the bandwidth of the nm CdSe/I$^-$/Zn4APc photodetectors is evaluated and compared to the data of the µm devices. Figure 6.11 shows both the normalized impulse photoresponses and the corresponding bandwidth spectra of all three types of detectors (µm polyimide, µm glass and nm glass, depicted in red, black, and blue, respectively). A reduced tail of the photoresponse in the nm glass devices compared to the µm glass devices is visible, which improves the device performance and results in the bandwidth spectra of the nm glass devices being less attenuated than the ones of µm glass devices for high frequencies. However, they are still slightly more attenuated than the ones for µm polyimide devices. The 3 dB bandwidth is approximately the same for nm and µm glass devices. I attribute the reduced tail in the impulse photoresponse of nm glass devices compared to µm glass devices to the active area being diminished to about 10 %, reducing the number of trap states per device.

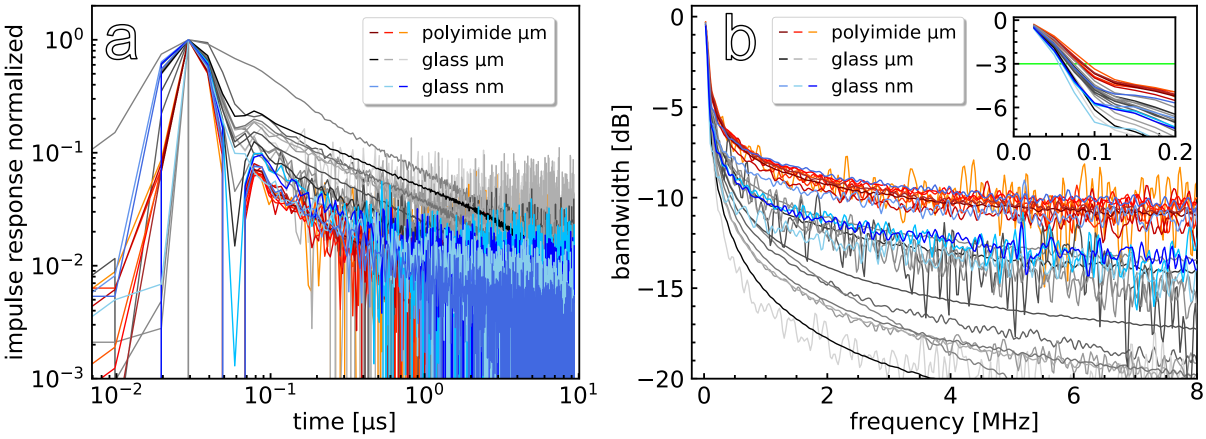

Figure 6.11. Photoresponses of CdSe/I$^-$/Zn4APc thin films on µm polyimide (red), µm glass (black) and nm glass (blue) substrates towards 636 nm 100 kHz illumination under 10 V bias applied for the µm devices and 1 V bias applied for the nm glass devices (one color = one device). a) Normalized transient photocurrent. b) Corresponding bandwidth spectra, calculated via Formula (4) and using zero-padding to convert the 100 kHz impulse responses into quasi 25 kHz data. Inset: enlarged view on the 3 dB bandwidth. Adapted with permission from Schedel et al.[49] and modified. Copyright 2021, American Chemical Society.

The impulse response of the nm glass devices can be described with the same two models as applied for the µm devices. A first exponential decay with a time constant of 2.5 ns ($\propto e^{-\frac{t}{2.5\,\mathrm{ns}}}$) independent of the applied electric field and the chosen channel length indicates the same initial carrier recombination and hopping as for the µm detectors. This drop is followed by a slower decay, which obeys a power law, as in the case of the µm detectors. Under the same electric field strengths, the Urbach energies determined are identical to the Urbach energies of the µm glass detectors, cf. Figure 6.12. Up to 40 kV/cm, Urbach energies of about 40 – 50 meV are evaluated, which decrease to approx. 25 meV for higher field strengths up to 86 kV/cm.

The decrease of the Urbach energy with increasing electric field can be explained with the increased probability of excitation of charge carriers from the trap states back into the band with the help of the field. As a result, the occupation density of the trap states is closer to the band edge at higher fields.

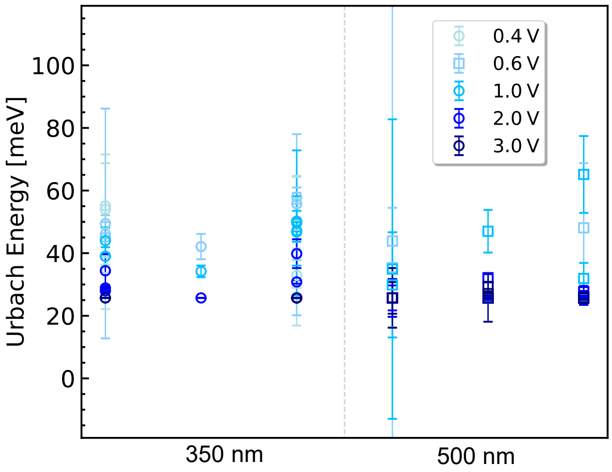

Figure 6.12. Urbach energies of the nm glass devices with different voltages applied. x-axis: electrode gap (350 nm, 500 nm × 10 mm), contacts listed. Adapted with permission from Schedel et al.[49] Copyright 2021, American Chemical Society.

6.4 Conclusion

The speed of response of a CdSe/I^-/Zn4APc QD photodetector on both glass and polyimide substrates was investigated. The high dielectric constant of glass gives rise to a more pronounced multiple trapping and release mechanism in the transient photocurrent decay compared to the same photodetectors on polyimide that has a smaller dielectric constant. The bandwidth on glass is therefore reduced to 67 kHz, whereas it is 85 kHz for the polyimide-based detectors. The generally high resistances in QD thin films challenge the development for high-speed QD photodetectors because they impose an RC limitation on the devices. For further enhancement of the electrical bandwidth, a significant reduction in the photoresistance has to be achieved.

7

Substrate Effects on the Speed Limiting Factor of WSe_2 Photodetectors

Related Article

- Schedel, C.; Strauß, F.; Kohlschreiber, P.; Geladari, O.; Meixner, A. J.; Scheele, M., Substrate Effects on the Speed Limiting Factor of WSe_2 Photodetectors. *Phys. Chem. Chem. Phys.* **2022,** *24* (41), 25383-25390.

To accelerate photodetectors that utilize nanostructured materials as photoabsorber, the photoresistance of this film has to be improved in order to reduce the RC time. The resistances of the CdSe detectors studied in the last Chapter were very high because of a limited charge carrier mobility. Due to their significantly higher mobilities, layered materials such as transition metal dichalcogenides are a promising class of materials for application in photodetectors.

In this Chapter, the influence of the two substrates glass and polyimide towards the speed of the photoelectric response of otherwise identical WSe_2 photodetectors is examined. Time-resolved photoresponses are investigated under both 635 nm square pulse illumination, reaching steady state photocurrent, and 636 nm and 779 nm impulse illumination, operating under non-steady state conditions. WSe_2 detectors on glass are accelerated by applying a bias and the bandwidth can be increased to about 2.6 MHz. In contrast, an applied electric field does not affect the speed of the detectors on polyimide. Those devices on polyimide are limited by capacitive (dis-)charging (RC limited), whereas the ones on glass are limited by slower excitonic diffusion processes. I ascribe this to the higher dielectric screening of glass with a large dielectric constant compared to polyimide with a small one, resulting in a shortened depletion layer width at the metal electrode / WSe_2 interface on top of glass. Thus, the change of substrate material alters the mechanism that limits the speed of the photoresponse of the otherwise identical WSe_2 detector.

The investigated WSe_2 flakes were typically 30 – 50 nm thick, cf. Figure 3.9 in Chapter 3.6.4, however, when attached to polyimide, they provided very low photocurrents under both square pulse and impulse illumination. Therefore, thicker crystals of about 100 – 200 nm had to be investigated on polyimide to achieve a sufficient signal-to-noise ratio. As all crystals have at least 40 layers,[208, 214, 215, 222] a bulk behavior can be assumed for the detector except for the top and bottom layers which are in direct contact with the surrounding media, namely the substrate and the atmosphere.

For low power dissipation, a small dark current of a photodetector is required. In Figure 7.1a, the dark currents under atmospheric conditions of the detectors on glass, depicted in black, and on polyimide, depicted in red, are shown. For both substrate materials, the typical, non-ohmic behavior of a MSM diode with Schottky junctions is observed. The dark current for the devices on polyimide is strongly reduced, which is promising to achieve high on / off ratios $\frac{on}{off} = \frac{I_{Photo}}{I_{dark}}$ during photodetection. A variation in dark current for different substrates was also shown for a BeZnO alloy on top of sapphire, PET and PEN[42] and can be ascribed to enhanced scattering of charge carriers on rough surfaces (surface roughness: 30.7 ± 11.6 nm on polyimide, vs 5.5 ± 0.7 nm on glass, cf. Chapter 5.2 with Figure 5.6).[247, 285] Isolating, atomically flat hexagonal boron nitride is often used as surface on which 2D optoelectronic materials are deposited to avoid this scattering and it increases charge carrier mobility considerably.[21, 230, 285] Moreover, the high dark current on glass indicates an effective minimization of silanol groups by surface modification with HMDS, cf. Chapter 5.2 with

Figure 5.4, which would otherwise act as electron traps and represent strong Coulomb scattering centers at the substrate / semiconductor interface.[245, 279, 280]

The steady state photocurrent under several applied biases from – 200 mV to 200 mV is shown in Figure 7.1b. A nonlinear dependence of the applied bias is observed, as already reported for WSe_2 photodetectors.[21, 286]

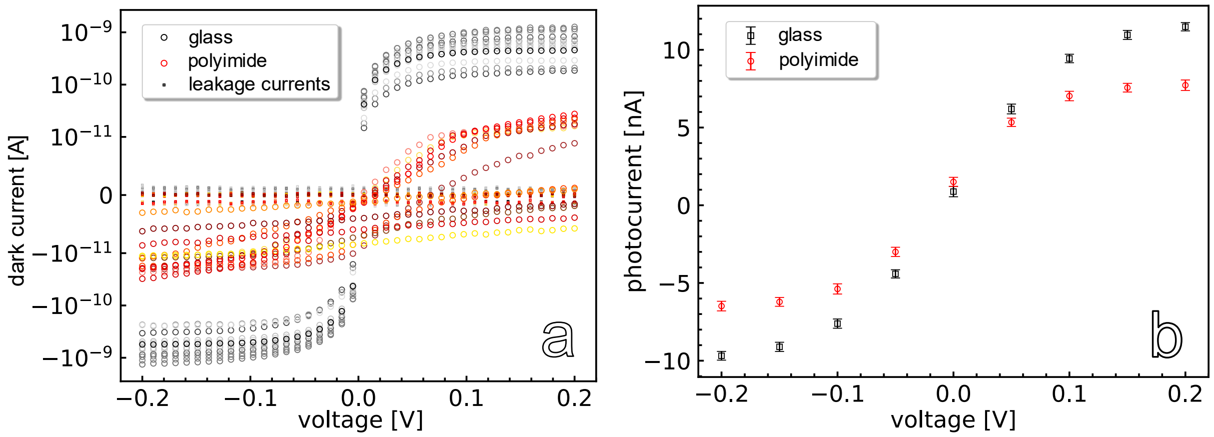

Figure 7.1. Dark currents of all WSe_2 MSM photodetectors on glass (black) and polyimide (red). b) Steady state photocurrent under different applied biases for a typical 5 µm channel length detector on glass (black) and a typical 2.5 µm channel length detector on polyimide (red) under 635 nm illumination (≤ 12 mW). Adapted with permission from Schedel et al.[50] and modified. Copyright 2022, the Royal Society of Chemistry (PCCP Owner Societies).

7.1 Steady State (“Square Pulse”) Investigations

The time-resolved photocurrent response of one typical WSe_2 crystal on polyimide and one on glass towards 635 nm 10 kHz square pulse illumination (≤ 12 mW) for different applied biases and under atmospheric conditions is shown in Figures 7.2a and 7.2b, respectively. With comparable absolute photocurrents, the speed of the response on polyimide detectors differs significantly from glass devices. On polyimide, the photoresponse rise and fall times (10 % – 90 %) are independent of an increasing electric field and last for about 500 ns to 1 µs regardless of the applied bias and channel length, cf. Figures 7.2e and 7.2f. In contrast, on glass, the rise and fall times depend on the applied voltage, taking about 6 µs when only ± 50 mV is applied and accelerating to about 1 µs when ± 200 mV is applied, see Figures 7.2c and 7.2d. There is no channel length dependence observable. With these switching speeds, the WSe_2 detectors in this work are among the fastest TMDC based photodetectors reported to date[21, 109, 246, 268, 286-289] and those detectors are indeed significantly faster than the ones based on CdSe/I^-/Zn4APc, presented in the last Chapter.

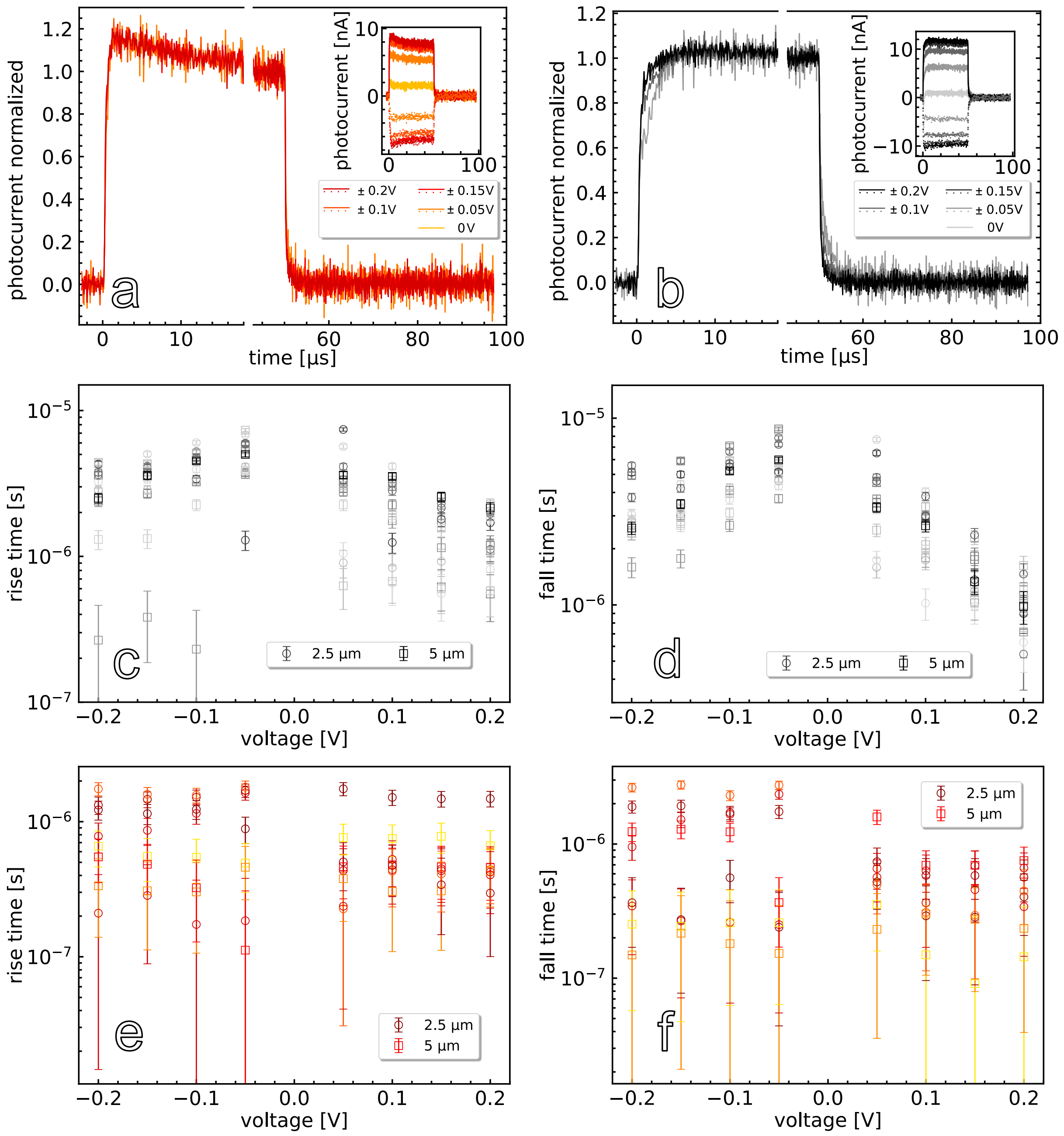

Figure 7.2. Normalized photoresponse of one typical WSe_2 photodetector on a) polyimide (channel length: 2.5 µm) and b) glass (channel length: 5 µm) towards a 635 nm 10 kHz square pulse illumination at different voltages. Insets: absolute photocurrents. Correlation of measured rise times (c, e) and fall times (d, f) vs. the applied biases for all glass detectors (c, d) and all polyimide devices (e, f). One color = one sample. Adapted with permission from Schedel et al.[50] and modified. Copyright 2022, the Royal Society of Chemistry (PCCP Owner Societies).

For the photodetectors on glass, the dependence of the rise time on the applied electric field seems to suggest a transit time limitation, for which mobile charge carriers are transported at higher velocity through the channel length as the field strength increases, assuming that saturation velocity is not reached, see Formula (15). In addition, this transit time limitation would cause a square dependence on the channel length. However, for all the detectors on both glass and polyimide, there is no measurable dependence of the rise / fall times on the examined channel lengths of 2.5 µm and 5 µm, cf. Figures 7.2c – 7.2f, arguing against a transit time limitation.

The lack of electric field dependence of the rise / fall times for the polyimide devices indicates an RC limitation, as described in Chapter 6. To verify this, I checked the RC time of all detectors and compared them with the corresponding measured rise times, see Figure 7.3. Therefore, I calculated the capacitances theoretically according to Formula (23): $C = L(N-1)\varepsilon_0(1+\varepsilon_r)\frac{K(k)}{K(k')}$,[116] using the in-plane dielectric constant of WSe_2 for 1.95 eV incident photon energy ($\varepsilon_r = 20$)[290, 291], the number of electrode fingers ($N = 2$), the length of the electrode fingers ($L = 80$ µm), and the width of the electrode fingers (w = 10 µm). With that, I assume the device capacitance to be about 24 fF and 19 fF for channel lengths of 2.5 µm and 5 µm, respectively. The photoresistances have been calculated directly from the measured steady state photocurrents for different applied biases. As can be seen in Figure 7.3a, for polyimide devices, the calculated $R_{illum}C$ times fit perfectly to the measured rise times and verify the RC limitation of these devices.

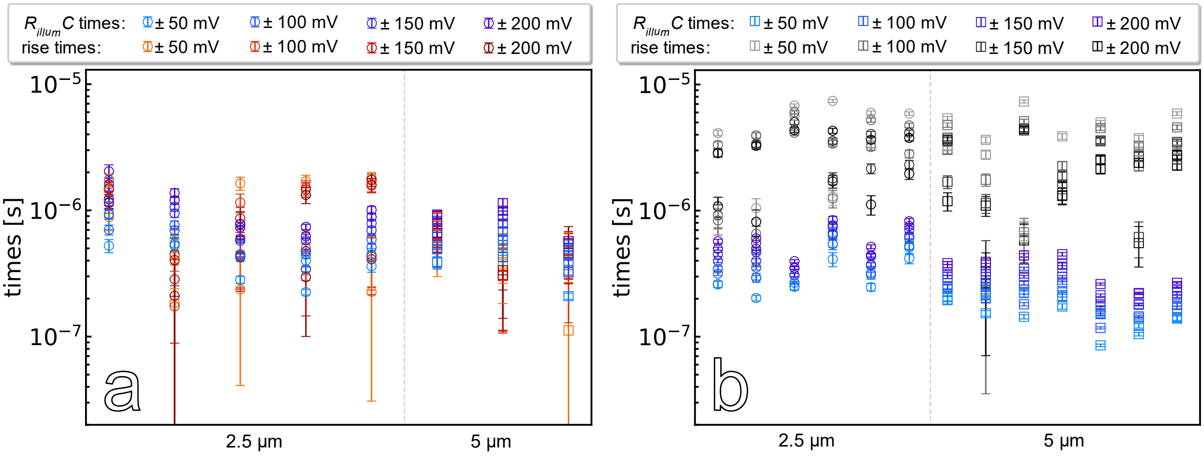

Figure 7.3. Comparison of measured rise times and calculated $R_{illum}C$ times for all devices on a) polyimide and b) glass. x-axis: electrode gap (2.5 µm / 5 µm × 80 µm), contacts listed. Adapted with permission from Schedel et al.[50] and modified. Copyright 2022, the Royal Society of Chemistry (PCCP Owner Societies).

On glass, on the contrary, the calculated $R_{illum}C$ times are expected to be faster than the actual measured rise times, see Figure 7.3b. Together with the present field strength dependence of the rise time, this argues against an RC limitation for those detectors. This assumption is supported further by the fact that the rise / fall times are also independent of the photoresistances (R_{illum}), controlled by the photocurrent level. This is depicted in Figure 7.4.

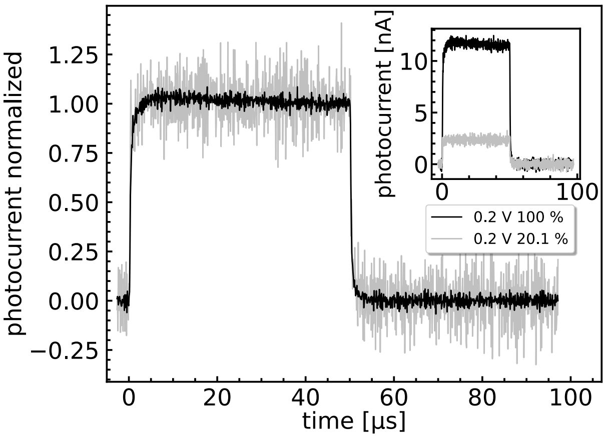

Figure 7.4. Normalized photoresponse of a typical WSe_2 detector on glass (channel length: 5 µm) towards 635 nm 10 kHz square pulse illumination for different laser intensities. Inset: absolute photocurrents. Adapted with permission from Schedel et al.[50] Copyright 2022, the Royal Society of Chemistry (PCCP Owner Societies).

Therefore, another process must limit the speed of response of the WSe_2 photodetectors on glass. The dark currents of the detectors indicate a Schottky barrier at the metal / WSe_2 interface, cf. Figure 7.1a, which is an important factor in the performance of TMDC photodetectors.[21, 111, 136, 286, 288, 292, 293] Photocurrent is primarily generated in the depletion region at the Schottky junction because of efficient exciton dissociation due to the built-in electric field. The depletion region extends over several micrometers into the TMDC and can be tuned by an applied gate voltage.[21, 136] This allows the Schottky junctions for both trilayer[286] and multilayer[292] WSe_2 to be reduced from several tens of meV to approximately 0 eV in an ohmic contact by applying an appropriate gate voltage.

Glass has a higher dielectric constant of 4.5-8[277] compared to polyimide with 3.5-3.7[281, 282], which, as I suggest, results in a shortened depletion region on glass due to an enhanced dielectric screening and a stronger polarization. For a depletion width shorter than a 2.5 µm channel length, hence, when the channel is not fully depleted, excitonic diffusion has to be considered. The rich excitonic features of WSe_2 include trions[231, 254, 269], which behave in an electric field like free charge carriers but with an enhanced effective mass.[294, 295] Thus, trion diffusion is accelerated with an increasing electric field and the speed of response of the detector on glass is increased. While excitons in WSe_2 of several 10 nm thickness (comparable to the crystals investigated in this work) have a diffusion length of 380 nm[296] at room temperature, the trion diffusion length is expected to be shorter.[297, 298] Therefore, it influences all devices similarly, and no channel length dependence arises. However, detailed spatial studies of the photoresponse are beyond the scope of this work.

The influence of the substrate towards the responsivity of a photodetector is known in literature.[38, 42] Using the steady state photoresponse, the on / off ratio of WSe_2 crystals on polyimide can be observed to be about 325. It shows a high scattering with values as high as 3603, but also 24 has been measured once. The on / off ratio is significantly lower on glass with 18 ± 10 (median and standard deviation, highest on / off ratio of 44), which can be ascribed to the higher dark currents of WSe_2 crystals on glass compared to polyimide.

7.2 Non-Steady State (“Impulse”) Investigations

The normalized transient photocurrent response of a typical WSe_2 crystal on glass at different applied biases towards 636 nm 100 kHz impulse illumination ($\leq$ 22 µW average output power) under atmospheric conditions is shown in Figure 7.5a. The photocurrent response is accelerated considerably with increasing field strength, enabling a tunable 3 dB bandwidth, see Figure 7.5b. The bandwidth is 2.57 ± 1.55 MHz when 200 mV is applied and typical values of 132 ± 53 kHz are observed for 50 mV bias applied. I attribute this to slowly diffusing trions, which are accelerated by an applied electric field in a not fully depleted WSe_2 channel on top of glass, as for the situation under square pulse illumination.

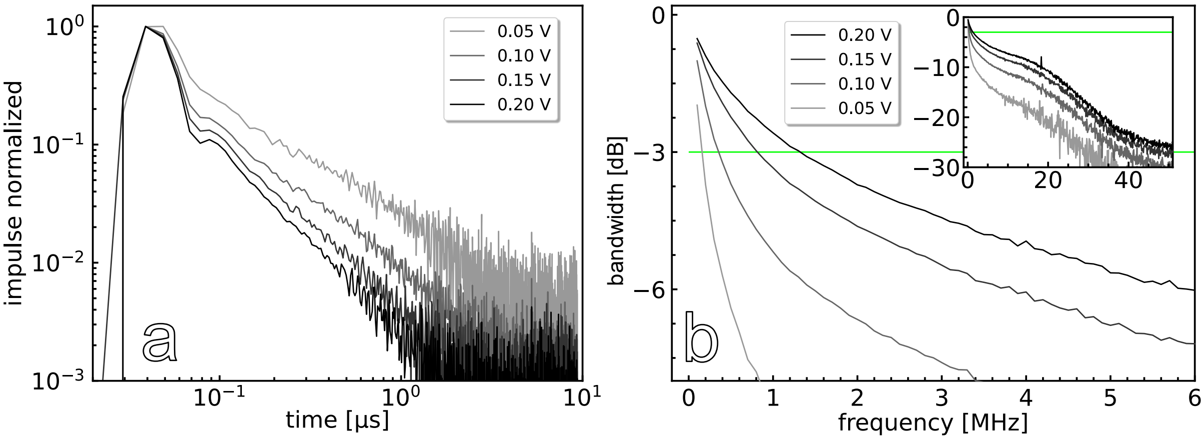

Figure 7.5. a) Typical, normalized impulse photoresponse of a WSe_2 photodetector on glass (5 µm channel length) for different applied voltages under 636 nm 100 kHz impulse illumination. b) Corresponding bandwidth spectra of the impulse spectra shown in (a). The bandwidth increases from 160 kHz for 50 mV applied to 1.32 MHz for 200 mV applied. Inset: Full range of the bandwidth spectrum. Adapted with permission from Schedel et al.[50] Copyright 2022, the Royal Society of Chemistry (PCCP Owner Societies).

In contrast, the WSe_2 photodetectors on polyimide do not exhibit a field dependence, see Figure 7.6a. This can be explained by the RC limitation of the polyimide devices. The 3 dB bandwidth is calculated to 619 ± 365 kHz, regardless of the applied bias. The reduced signal to noise ratio is due to the lower absolute photocurrents of the detectors on polyimide compared to the ones on glass and causes the high standard deviation, cf. Figure 7.6b. For some of the polyimide devices, there is no measurable impulse photoresponse at all. This contrasts with their high on / off ratio under steady state conditions. It can be explained with the effect the dark current has on the on / off ratio, which is not considered in the time-resolved studies where only the photocurrent is measured. The normalized photoresponse under both 636 nm and 779 nm impulse illumination is the same for otherwise identical conditions, as shown in Figure 7.6c.

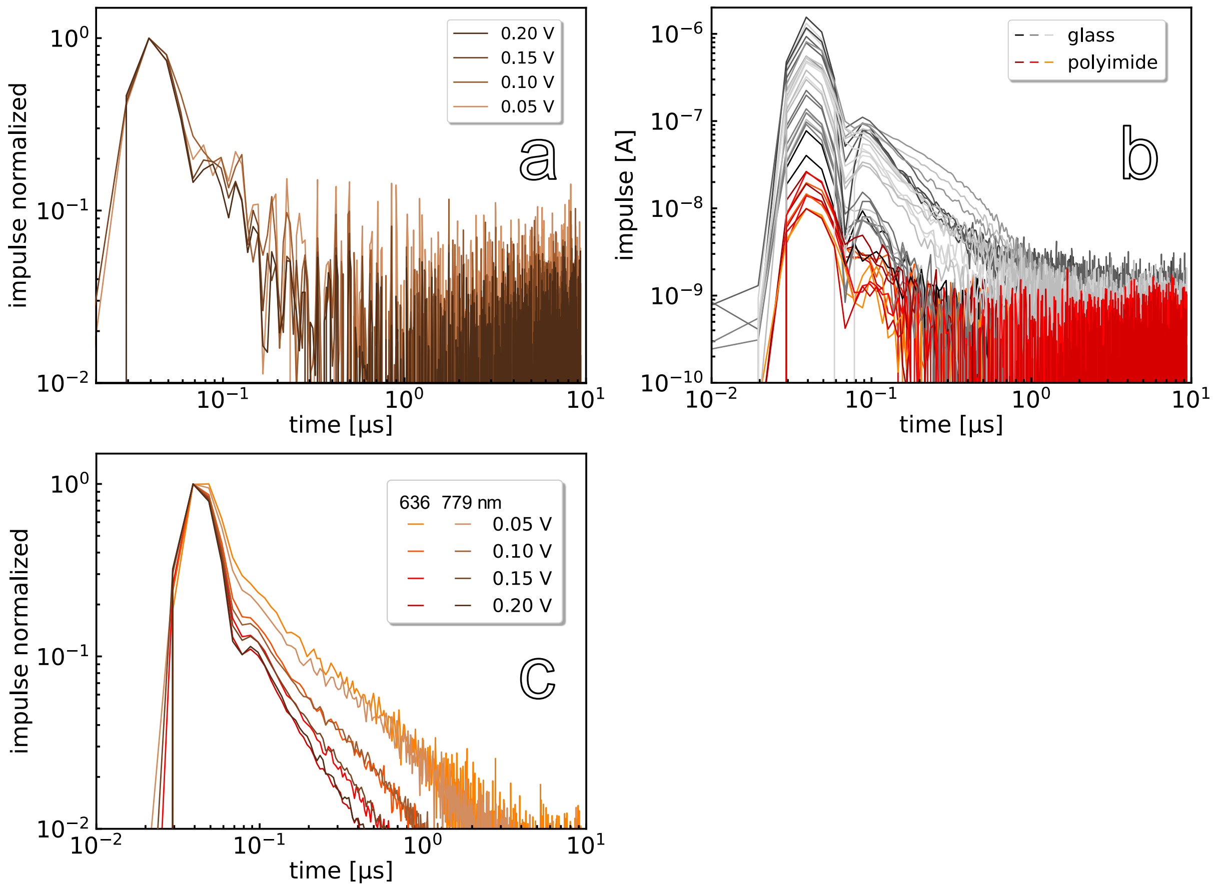

Figure 7.6. a) Normalized photoresponse of a WSe_2 crystal on polyimide (2.5 µm channel length) under 779 nm 100 kHz impulse illumination with different biases applied. b) Absolute impulse photoresponses of all WSe_2 detectors on glass (black) and polyimide (red) under 779 nm 100 kHz illumination with 200 mV applied. c) Normalized photoresponse under both 636 nm and 779 nm 100 kHz impulse illumination, exemplarily shown for a WSe_2 crystal on glass (5 µm channel length). Adapted with permission from Schedel et al.[50] and modified. Copyright 2022, the Royal Society of Chemistry (PCCP Owner Societies).

As for the dark current, the photocurrent on polyimide is inhibited by dangling bonds, impurities, charge traps, a reduced dielectric screening and surface roughness, thus, efficient carrier transport is prevented.[19, 245, 247, 285] Moreover, the excitonic binding energy in TMDCs decreases with increasing dielectric constant of the surrounding.[227, 228, 251, 253-255] This enables a more efficient exciton / trion separation and photocurrent generation in the very short time scale of the laser impulse on glass with its higher dielectric constant than polyimide. The reduced photocurrent on polyimide devices limits their application in fast optical switches for data transmission.

7.3 Atmospheric Influences

Surface adsorbed oxygen and water can dope transition metal dichalcogenides and influence their conductivity.[220, 253, 299] Therefore, not only the substrate material but also the contact with the atmosphere must be considered. When the photodetectors are prepared under atmosphere and measured under nitrogen, a strong increase in conductivity is observed for the glass devices, which lasts for several hours and is reversible upon contact with atmosphere again, see Figure 7.7a. In contrast, the conductivity is roughly constant for the WSe_2 crystals attached to a polyimide foil.

For the flake thicknesses of the investigated WSe_2 crystals exceeding 30 nm, I assume n-type conductance based on previous reports.[206, 213] The electron mobility decreases upon contact with oxygen and water[206] and lowers the conductivity of the WSe_2 flakes under atmosphere in comparison to investigations under nitrogen. Oxygen most likely desorbs continuously over several hours when the photodetectors are placed under nitrogen, explaining the long-term increase in conductivity of the detectors on glass. For WSe_2 crystals on polyimide, this effect can hardly be observed. I attribute this to the higher surface roughness of polyimide with 30.7 ± 11.6 nm compared to glass with 5.5 ± 0.7 nm, giving rise to air inclusions between polyimide and WSe_2. Exchange with nitrogen is not possible for these inclusions trapped at the interface and they dominate the conductance of the crystals.

In order to have comparable situations for both types of detectors with constant dark currents, I therefore decided to perform the measurements under atmosphere and not under nitrogen or in vacuum. Moreover, the electron mobility and the photoresponse are enhanced due to chemisorbed oxygen. It saturates chalcogen vacancies at the WSe_2 surface and by that removes electron trap states and carrier scattering centers.[300] In addition, oxygen doping inducing surface oxidation has already been shown to accelerate the photoresponse of ambipolar WSe_2 towards square pulse illumination.[17] Therefore, I made sure to keep the atmospheric conditions as similar as possible.

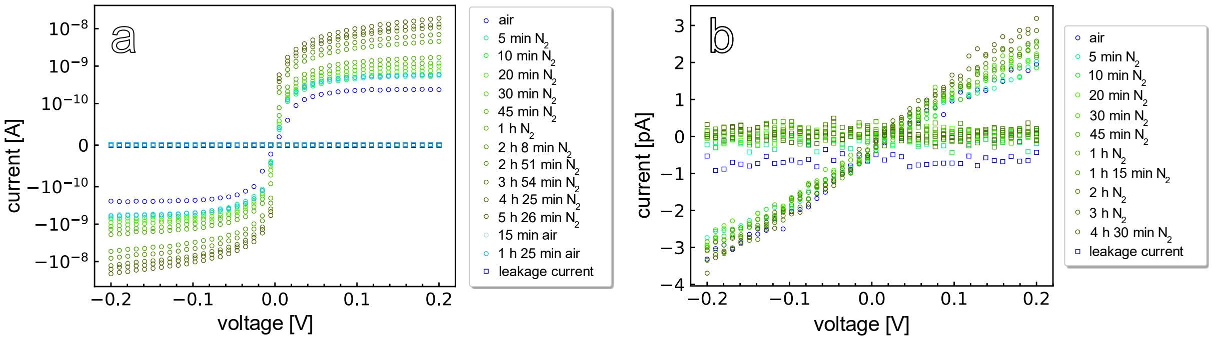

Figure 7.7. Dark current under atmosphere and for a specific time under nitrogen for typical WSe_2 crystals on a) glass and b) polyimide (5 μm channel lengths), with the reversibility shown on glass. Circles represent the current measured, squares depict the corresponding leakage current. Adapted with permission from Schedel et al.[50] and modified. Copyright 2022, the Royal Society of Chemistry (PCCP Owner Societies).

7.4 Conclusion

The time-resolved photoelectrical response of WSe_2 photodetectors on polyimide with a small dielectric constant and on glass with a large dielectric constant have been investigated. The mechanism that limits the speed of response of the photodetector changes by varying the substrate material. Photodetectors on polyimide are RC limited while the ones on glass are limited by excitonic diffusion processes and can be accelerated with an increasing electric field to a bandwidth of about 2.6 MHz. I attribute this change in the limitation of the speed of response to a shortening of the depletion width at the metal electrode / WSe_2 interface for the detectors on glass due to higher dielectric screening.

8

Summary and Outlook

8.1 Summary

In the present work, the influence of the substrate towards the speed of response of otherwise identical photodetectors is investigated, an aspect scarcely considered in literature.

Therefore, a setup for time-resolved photocurrent studies for both, square pulse and impulse illumination of photodetectors, was established initially. The functionality of the setup is verified with the use of commercial photodetectors in Chapter 4. The measurement techniques utilized in this work, illumination of a detector with a laser impulse or a laser square pulse, are introduced. Materials that are photoactive themselves at the spectral range of the utilized illumination cannot be used as substrate materials for photodetectors. Even with a thin insulating layer on top, as for the investigated Si/SiO_2 substrates, in time-resolved photocurrent studies, a convoluted photoresponse of the substrate and the material to be investigated must be expected. Details are given in Chapter 5. Since I was planning to work in the vis and NIR range for the development of high-speed photodetectors for visible range communication and telecommunication, I chose to fabricate detectors on glass and on the polyimide foil Kapton.

The present work shows that the choice of glass or polyimide as substrate has a significant influence on the speed of response of photodetectors. The observed effects can be explained by different dielectric screening caused by the substrates, since glass has a high dielectric constant whereas polyimide has a low one. The influence of the substrate on the speed of response of photodetectors is demonstrated for detectors with photoactive layers based on CdSe QDs or WSe_2 crystals.

An iodide capped CdSe QD thin film, sensitized with zinc β-tetraaminophthalocyanine (CdSe/I^-/Zn4APc), absorbs both in the vis range and in the first telecommunication window, thus, it is a fascinating material for application in optical communication. The transient response shows the higher electrical bandwidth of 85 kHz when the films are prepared on polyimide compared to 67 kHz when glass is utilized. This is due to a slowly decaying long tail in the transient photoresponse which can be ascribed to multiple trapping and release and is more pronounced on glass. The high dielectric constant of glass reduces the charging energy of the QDs close to glass and enables more trap states to be occupied at the QD – glass interface compared to the QD – polyimide interface. Thus, the tail current is enhanced for photodetectors based on glass due to a more pronounced multiple trapping and release process in the QD film. All detectors are RC limited as capacitive (dis-)charging limits their speed of response. Details are given in Chapter 6, and these results have been published in ACS Materials and Interfaces under the title "Substrate Effects on the Bandwidth of CdSe Quantum Dot Photodetectors".

The large RC time of the CdSe/I^-/Zn4APc detectors is induced by the low mobilities of QD based photodetectors. Significantly higher mobilities can be found in layered materials, as for example in transition metal dichalcogenides. Therefore, a faster switching speed than observed for the CdSe/I^-/Zn4APc detectors is expected. Moreover, TMDCs offer interesting excitonic features and, due to their layered structures, large influences of the dielectric environment on their optoelectronic properties are already known.

For WSe_2 photodetectors on glass and polyimide, the choice of the substrate influences the mechanism that limits the speed of the detectors. The detectors on polyimide are RC limited and their speed is not affected by an applied electric field. On the contrary, detectors on glass can be accelerated with an increasing electric field and the bandwidth is enhanced up to about 2.6 MHz. I ascribe this to excitonic diffusion processes. They arise as the depletion width at the metal / WSe_2 interface is shortened on glass compared to the one on polyimide due to the strong dielectric screening. Details are given in Chapter 7 and these results have been published in Physical Chemistry Chemical Physics under the title "Substrate Effects on the Speed Limiting Factor of WSe_2 Photodetectors".

In summary, the present work demonstrates that the substrate can be a crucial factor in the time-resolved photoelectrical response of photodetectors and must be considered to a much greater extent than has been the case to date. The large impact of the substrate on the speed of response of two such different classes of materials highlights the importance of the choice of substrate in the development of high-speed photodetectors.

8.2 Outlook

Many different substrate materials are used in the development of photodetectors, and this work shows that the substrate has a significant effect on the speed of response of otherwise identical detectors. I ascribe this to the different dielectric constants of the substrates investigated. An in-depth study, in which the effect of many different isolating substrate materials with dielectric constants as identical as possible is examined towards the properties of one photoabsorber material, could supportively investigate, whether the dielectric constant is the key factor for the observed effects, as I assume, or if the chemical interface and the surface roughness must be considered more closely. For this purpose, WSe_2 detectors are more suitable than CdSe QD detectors, since they do not require an annealing step during their fabrication and many polymers, which usually have low glass transition temperatures, can be considered as substrate materials. Simultaneously, due to the chemical variety of possible substrates, such an investigation can also determine whether there are more functional groups that act as charge carrier traps, such as the silanol group.

In the present work, bulk-like WSe_2 crystals were considered. Since the effect of a dielectric on optoelectronic properties is much more pronounced for thin layers, the investigation of mono- or few-layer TMDC detectors could reveal even more distinct effects. Moreover, the electronic properties of TMDCs are influenced not only by the substrate but also by surface adsorbates. A variation of this second interface offers further possibilities that might influence the speed of these photodetectors and in-depth investigations are still lacking.

Not only for WSe_2 detectors, but also for the CdSe QD photodetectors, further questions arise from the present investigation. The RC limitation could not be avoided with the investigated reduction of the channel length. An examination of even shorter channel lengths of, for example, a few tens of nanometers significantly reduces the number of necessary hopping steps. In combination with sufficiently wide electrode fingers that ensure low electrode resistance, this could possibly circumvent the major disadvantage of QD detectors, their high resistances. Moreover, it could be checked whether the RC limitation could be circumvented by using other ligands than zinc β-tetraaminophthalocyanine which might allow much higher mobilities in the QD film. However, a loss of responsivity in the NIR range would have to be accepted.

In the present work, a bottom electrode configuration was used. This was done to ensure that the substrate is directly adjacent to the region where charge transport takes place predominantly, so that that the effect of the dielectric constant is maximized. The thicknesses of the active materials varied greatly with 30 – 200 nm for WSe_2 crystals, while the QD films were up to 4 µm thick. When using top electrodes on the optically active material, it would now be interesting to explore where the limit is, up to which the substrate still has a significant effect on the detector performance.

In summary, many open questions remain to be investigated to gain a profound understanding of the effects of a substrate on the speed of the response of otherwise identical photodetectors.

List of Abbreviations

0D	zero dimensional
1D	one dimensional
2D	two dimensional
3D	three dimensional
AFM	atomic force microscopy
CdSe/I^-/Zn4APc	iodide-capped CdSe quantum dots, sensitized with zinc β-tetraaminophthalocyanine
COINFLIP	Coupled Organic Inorganic Nanostructures for Fast, Light-Induced Data Processing
dB	decibel
FFT	fast Fourier transformation
FWHM	full width half maximum
high-κ-dielectric	material with high dielectric constant
HMDS	hexamethyldisilazane
IS	impedance spectroscopy
ITO	indium tin oxide
Kapton HN	poly(4,4'-oxydiphenylene pyromellitimide)
k-space	reciprocal space
MSM	metal-semiconductor-metal
NEP	Noise Equivalent Power
NIR	Near Infrared
PDMS	polydimethylsiloxane
PEN	polyethylene naphthalate
PET	polyethylene terephthalate
QD	quantum dot
RC	resistance-capacitance
RMS	root mean square
SEM	scanning electron microscopy
TMDC	transition metal dichalcogenide
UV	Ultraviolet
Vis	Visible
Zn4APc	zinc β-tetraaminophthalocyanine

List of Symbols

a_{Exc}	Bohr exciton radius
A	detector area
α	empirical scaling factor
$\alpha(\lambda)$	absorption coefficient
$\Delta\alpha$	energetic disorder
β	transfer integral
β_0	current gain
C	capacitance
C_C	collector-base junction capacitance
C_E	emitter-base junction capacitance
C_S	self capacitance
C_M	mutual capacitance
d	detector length
d	interparticle distance
D	displacement field
$D(E)$	density of states
$D_{occ}(E)$	occupation density
D^*	specific detectivity
D_i	diffusion coefficient, for $i = n, p$ with $n =$ electron, $p =$ hole
e	elementary charge
E	energy
E_a	activation energy
E_B	exciton binding energy
E_C	conduction band
E_C	charging energy
$E_d(t)$	demarcation energy
E_g	band gap
$E_{g,opt}$	optical band gap
$E_{th}(t)$	thermalization energy
E_U	Urbach energy
E_V	valence band
ΔE	tunnel barrier height
$\mathcal{E}$	electric field
ε_0	vacuum permittivity
ε_b	dielectric constant of the bottom layer
ε_r	dielectric constant, relative permittivity
ε_{QD}	dielectric constant of QD
ε_M	dielectric constant of the surrounding
ε_t	dielectric constant of the top layer
η	external quantum efficiency

$f_{3\ dB}$	3 dB bandwidth
$f_{3dB,RC}$	RC limited 3 dB bandwidth
f_{trans}	transit time limited bandwidth
g	channel length
G	gain
h	Planck's constant
$\hbar$	reduced Planck's constant
I_E	emitter current
I_{Photo}	photocurrent
I_{SD}	source-drain current
I_{SG}	leakage current, gate current
δI_{noise}	current noise spectral density
$K(k)$	complete elliptical integral of first kind
k_B	Boltzmann constant
κ	average dielectric constant of the surrounding material
L	length of the box
L	electrode finger length
l	diffusion length
λ	wavelength
M	reduced mass
m	mass of a particle
m_n	electron mass
m_p	hole mass
m^*	charge carrier effective mass
μ_n	mobility of electrons
μ_h	mobility of holes
n	principal quantum number
n	number of nearest neighbors
n	electron density
Δn	photogenerated electron density
N	number of electrode fingers
ν	frequency of the incident radiation
p	hole density
Δp	photogenerated hole density
P	polarization
$P(\omega)$	power spectrum
P_1	signal power under steady state conditions
P_{opt}	incident optical power
Φ_{bi}	built-in potential
Φ_m	metal work function
Φ_{SB}	Schottky barrier
ψ	wave function
r	QD radius

r_0	characteristic screening length
R	responsivity
R	resistance
R_L	load resistance
σ	conductivity
$\Delta\sigma$	photoconductivity
T	temperature
$t_{diff,i}$	diffusion time, for $i = n, p$ with $n =$ electron, $p =$ hole
t_{drift}	drift time = transit time
t_{fall}	fall time
t_{life}	lifetime, recombination time
t_{rise}	rise time
t_{trans}	transit time
τ	response time
τ_n	free electron lifetime
τ_p	free hole lifetime
τ_{RC}	RC time constant
U	voltage
U_B	reverse bias
$V(r)$	distance dependent electrostatic potential
v_n	electron velocity
v_p	hole velocity
w	width of the electrode finger
x	one dimension
Δx	tunnel barrier width
χ	electron affinity
χ	polarizability
υ	attempt-to-escape frequency

List of Figures

List of Tables

List of Publications

This thesis contains results published in the following publications:

- Schedel, C.; Strauß, F.; Kumar, K.; Maier, A.; Wurst, K. M.; Michel, P.; Scheele, M., Substrate Effects on the Bandwidth of CdSe Quantum Dot Photodetectors. *ACS Appl. Mater. Interfaces* **2021,** *13* (40), 47954-47961.

- Schedel, C.; Strauß, F.; Kohlschreiber, P.; Geladari, O.; Meixner, A. J.; Scheele, M., Substrate Effects on the Speed Limiting Factor of WSe_2 Photodetectors. *Phys. Chem. Chem. Phys.* **2022,** *24* (41), 25383-25390.

- Kumar, K.; Liu, Q.; Hiller, J.; Schedel, C.; Maier, A.; Meixner, A.; Braun, K.; Lauth, J.; Scheele, M., Fast, Infrared-Active Optical Transistors Based on Dye-Sensitized CdSe Nanocrystals. *ACS Appl. Mater. Interfaces* **2019,** *11* (51), 48271-48280.

- Schedel, C.; Strauß, F.; Scheele, M., Pitfalls in Determining the Electrical Bandwidth of Nonideal Nanomaterials for Photodetection. *J. Phys. Chem. C* **2022,** *126* (32), 14011-14016

Acknowledgements

Without the help of many brilliant, creative, motivated and hard working people, this work would not have come about. Therefore, I would like to take this opportunity to express my sincere thanks.

As my supervisor and head of the group, Prof. Dr. Marcus Scheele made this work possible for me, both financially and creatively. Without your ideas, the COINFLIP project and this thesis would not have been possible, and I want to thank you for your support, your optimism, and your help in our many conversations. Thank you for always having time and an open ear for me, no matter how busy you have been yourself. The high degree of freedom you gave me in developing this project and the faith you had in me and my work has allowed me to learn a great deal over the past few years, both scientifically and personally.

I am thankful to my secondary supervisor, Prof. Dr. Thomas Chassé, for his support and his ideas especially in the initial phase of the work when I was troubleshooting my setup. I could always count on helpful hints and ideas by him and his whole group, where I want to name in specific Prof. Dr. Heiko Peisert and Hilmar Adler. Moreover, I want to thank Prof. Dr. Thomas Chassé for being the second reviewer of this work.

I thank Prof. Dr. Alfred J. Meixner for the access to his lab and with that for the opportunity to investigate WSe_2, which would have been impossible otherwise. I thank Prof. Dr. David Wharam for his advice when I was troubleshooting my setup and the fruitful discussion. I want to thank Dr. Alexandru Oprea and Kai Wurst for their advice regarding impedance spectroscopy and many fruitful discussions.

My special thank goes to Dr. Andre Maier and Fabian Strauß, who are among the best office colleagues imaginable. You provided me with the substrates I needed thanks to your fast and reliable work in the clean room, and I always had someone with whom I could discuss problems, weird effects, and confusing stuff. Despite the many setbacks I had, I always had companions in you who supported me in word and action. Andre, thank you for always being interested in my work, offering another perspective, and pointing out to me that things are moving forward. Fabian, thank you for sharing some of the setbacks (and the suffering) with me, while still having so much fun together. Without the two of you, everyday life would have been much harder and much less fun!

My special thank also goes to Kai Wurst, who supported me in every possible way. Without your patient introduction into Python and the correction of my errors in the scripts, I would probably still be evaluating my data today. Thank you for always being there for me.

Patrick Michel provided me with high-quality QDs and Olympia Geladari introduced me into her exfoliation setup. Pia Kohlschreiber supported me in my last weeks in the lab, and Elke Nadler, Andre Maier and Fabian Strauß performed electron microscopy measurements for me. Furthermore, Fabian Strauß performed profilometer measurements for me. Karsten Stampke and Walter Schaal assisted me with their technical advice. The crew of the mechanical workshop, especially Alexander Schnapper and Christof Binder, realized my drawings and the secretary office, especially Bettina Kappler, Brigitte Doez and Heike Alexa, always kept a wary eye on all forms and the daily business. – Thank you all for all of this! Furthermore, I want to thank Claudius Riek (Zurich Instruments), and Denis Doerr, Steffen Ruettinger and Mario Gerecke (PicoQuant) for technical support and fruitful discussions.

I enjoy teaching and thank my students for their enthusiasm: Fabian Strauß, Nicolas Bader, Katharina Gerber and Leah Schynowski. Moreover, I thank Jochen Mehne for his technical assistance in the student practical course.

I want to thank the whole Scheele group for the great working atmosphere, that they were always ready to talk about both scientific and non-scientific topics and for all the enjoyable activities we had. Thank you: Kai Wurst, Andre Maier, Fabian Strauß, Krishan Kumar, Björn Märker, Philipp Frech, Theresa Hettiger, Patrick Michel, Philipp Heizmann, Jan Wahl, Christopher Kirsch, Sonam Maiti, Michelle Weber, Sophia Westendorf, Pia Kohlschreiber and Robert Thalwitzer.

My special thank goes to Fabian Strauß und Kai Wurst for proofreading this thesis.

Last but not least, I want to thank my family. Your constant support and encouragement have always helped me to achieve my goals and I could not have done it all without you.

I received my academic education thanks to:

R. Anwander, N. Barsan, H. Bettinger, B. Casu, T. Chassé, K. Eichele, R. Fink, G. Gauglitz, S. Grond, C. Huhn, W. Jäger, S. Keppeler, M. Kramer, D. Kunz, C. Maichle-Mössmer, M. E. Maier, H. A. Mayer, A. J. Meixner, H.-J. Meyer, B. Nachtsheim, U. Nagel, H. Peisert, T. E. Schäffer, M. Scheele, P. Sirsch, A. Schnepf, E. Schweda, B. Speiser, U. Weimar, L. Wesemann, D. Wistuba, D. Zhang, K.-P. Zeller, T. Ziegler.

Bibliography

1. Smith, W., Effect of Light on Selenium During the Passage of an Electric Current. *Nature* **1873,** *7*, 303-303.

2. Sale, Effect of Light on Selenium During the Passage of an Electric Current. *Nature* **1873,** *7*, 303-303.

3. Adams, W. G.; Day, R. E., V. The Action of Light on Selenium. *Proc. R. Soc. Lond.* **1877,** *25* (171-178), 113-117.

4. Hellmich, P., Record Data Transfer Speed in Fiber Optic Network Using TUM Algorithm - New Speed Record set under Real-World Conditions. URL: https://www.tum.de/en/about-tum/news/press-releases/details/35244/, 2019, date accessed: 11.05.2022.

5. Chakraborty, P. S.; Cardoso, A. S.; Wier, B. R.; Omprakash, A. P.; Cressler, J. D.; Kaynak, M.; Tillack, B., A 0.8 THz f_{MAX} SiGe HBT Operating at 4.3 K. *IEEE Electron Device Lett.* **2014,** *35* (2), 151-153.

6. Nada, M.; Nakajima, F.; Yoshimatsu, T.; Nakanishi, Y.; Kanda, A.; Shindo, T.; Tatsumi, S.; Matsuzaki, H.; Sano, K., Inverted p-Down Design for High-Speed Photodetectors. *Photonics* **2021,** *8* (2), 39.

7. Miya, T.; Terunuma, Y.; Hosaka, T.; Miyashita, T., Ultimate Low-Loss Single-Mode Fibre at 1.55 µm. *Electron. Lett.* **1979,** *15* (4), 106-108.

8. Wartak, M. S., *Computational Photonics: An Introduction with MATLAB*. Cambridge University Press: Cambridge, 2013; p 1-16.

9. Grobe, L.; Paraskevopoulos, A.; Hilt, J.; Schulz, D.; Lassak, F.; Hartlieb, F.; Kottke, C.; Jungnickel, V.; Langer, K., High-Speed Visible Light Communication Systems. *IEEE Commun. Mag.* **2013,** *51* (12), 60-66.

10. Khan, L. U., Visible Light Communication: Applications, Architecture, Standardization and Research Challenges. *Digit. Commun. Netw.* **2017,** *3* (2), 78-88.

11. Li, Z.; Xu, K.; Wei, F., Recent Progress in Photodetectors based on Low-Dimensional Nanomaterials. *Nanotechnol. Rev.* **2018,** *7* (5), 393-411.

12. Yadav, P. V. K.; Ajitha, B.; Kumar Reddy, Y. A.; Sreedhar, A., Recent Advances in Development of Nanostructured Photodetectors from Ultraviolet to Infrared Region: A Review. *Chemosphere* **2021,** *279*, 130473.

13. Konstantatos, G.; Levina, L.; Fischer, A.; Sargent, E. H., Engineering the Temporal Response of Photoconductive Photodetectors via Selective Introduction of Surface Trap States. *Nano Lett.* **2008,** *8* (5), 1446-1450.

14. Tang, J.; Konstantatos, G.; Hinds, S.; Myrskog, S.; Pattantyus-Abraham, A. G.; Clifford, J.; Sargent, E. H., Heavy-Metal-Free Solution-Processed Nanoparticle-Based Photodetectors: Doping of Intrinsic Vacancies Enables Engineering of Sensitivity and Speed. *ACS Nano* **2009,** *3* (2), 331-338.

15. Dolatyari, M.; Rostami, A.; Mathur, S.; Klein, A., Trap Engineering in Solution Processed PbSe Quantum Dots for High-Speed MID-Infrared Photodetectors. *J. Mater. Chem. C* **2019,** *7* (19), 5658-5669.

16. Wei, H.; Fang, Y.; Yuan, Y.; Shen, L.; Huang, J., Trap Engineering of CdTe Nanoparticle for High Gain, Fast Response, and Low Noise P3HT:CdTe Nanocomposite Photodetectors. *Adv. Mater.* **2015,** *27* (34), 4975-4981.

17. Seo, J.; Cho, K.; Lee, W.; Shin, J.; Kim, J.-K.; Kim, J.; Pak, J.; Lee, T., Effect of Facile p-Doping on Electrical and Optoelectronic Characteristics of Ambipolar WSe_2 Field-Effect Transistors. *Nanoscale Res. Lett.* **2019,** *14* (1), 313.

18. Hong, J.; Wang, M.; Jiang, J.; Zheng, P.; Zheng, H.; Zheng, L.; Huo, D.; Wu, Z.; Ni, Z.; Zhang, Y., Optoelectronic Performance of Multilayer WSe_2 Transistors Enhanced by Defect Engineering. *Appl. Phys. Express* **2020,** *13* (6), 061004.

19. Kufer, D.; Konstantatos, G., Highly Sensitive, Encapsulated MoS_2 Photodetector with Gate Controllable Gain and Speed. *Nano Lett.* **2015,** *15* (11), 7307-7313.

20. Zhang, W.; Chiu, M.-H.; Chen, C.-H.; Chen, W.; Li, L.-J.; Wee, A. T. S., Role of Metal Contacts in High-Performance Phototransistors Based on WSe_2 Monolayers. *ACS Nano* **2014,** *8* (8), 8653-8661.

21. Wang, T.; Andrews, K.; Bowman, A.; Hong, T.; Koehler, M.; Yan, J.; Mandrus, D.; Zhou, Z.; Xu, Y.-Q., High-Performance WSe_2 Phototransistors with 2D/2D Ohmic Contacts. *Nano Lett.* **2018,** *18* (5), 2766-2771.

22. Lopez-Sanchez, O.; Lembke, D.; Kayci, M.; Radenovic, A.; Kis, A., Ultrasensitive Photodetectors Based on Monolayer MoS_2. *Nat. Nanotechnol.* **2013,** *8* (7), 497-501.

23. Luo, W.; Cao, Y.; Hu, P.; Cai, K.; Feng, Q.; Yan, F.; Yan, T.; Zhang, X.; Wang, K., Gate Tuning of High-Performance InSe-Based Photodetectors using Graphene Electrodes. *Adv. Optical Mater.* **2015,** *3* (10), 1418-1423.

24. Jain, S. K.; Aggarwal, N.; Krishna, S.; Kumar, R.; Husale, S.; Gupta, V.; Gupta, G., GaN-UV Photodetector Integrated with Asymmetric Metal Semiconductor Metal Structure for Enhanced Responsivity. *J. Mater. Sci.: Mater. Electron.* **2018,** *29* (11), 8958-8963.

25. Ostroverkhova, O.; Platt, A. D.; Shepherd, W. E. B., Optical, Photoluminescent, and Photoconductive Properties of Novel High-Performance Organic Semiconductors. In *Advances in Lasers and Electro Optics*, Costa, N.; Cartaxo, A., Eds. Intech: Rijeka, 2010; pp 1-32.

26. Wu, H.; Huang, Y.; Zhi, Y.; Wang, X.; Chu, X.; Chen, Z.; Li, P.; Wu, Z.; Tang, W., Single-Layer Graphene Electrode Enhanced Sensitivity and Response Speed of β-Ga_2O_3 Solar-Blind Photodetector. *Opt. Mater. Express* **2019,** *9* (3), 1394-1403.

27. Burm, J.; Litvin, K. I.; Schaff, W. J.; Eastman, L. F., Optimization of High-Speed Metal-Semiconductor-Metal Photodetectors. *IEEE Photon. Technol. Lett.* **1994,** *6* (6), 722-724.

28. Averine, S. V.; Chan, Y. C.; Lam, Y. L., Geometry Optimization of Interdigitated Schottky-Barrier Metal–Semiconductor–Metal Photodiode Structures. *Solid-State Electron.* **2001,** *45* (3), 441-446.

29. Bencherif, H.; Djeffal, F.; Ferhati, H., Performance Enhancement of Pt/TiO_2/Si UV-Photodetector by Optimizing Light Trapping Capability and Interdigitated Electrodes Geometry. *Superlattices Microstruct.* **2016,** *97*, 303-312.

30. Koscielniak, W. C.; Pelouard, J. L.; Littlejohn, M. A., Dynamic Behavior of Photocarriers in a GaAs Metal-Semiconductor-Metal Photodetector with Sub-Half-Micron Electrode Pattern. *Appl. Phys. Lett.* **1989,** *54* (6), 567-569.

31. Gant, P.; Huang, P.; Pérez de Lara, D.; Guo, D.; Frisenda, R.; Castellanos-Gomez, A., A Strain Tunable Single-Layer MoS_2 Photodetector. *Mater. Today* **2019,** *27*, 8-13.

32. Lu, J.; Yao, J.; Yan, J.; Gao, W.; Huang, L.; Zheng, Z.; Zhang, M.; Li, J., Strain Engineering Coupled with Optical Regulation towards a High-Sensitivity In_2S_3 Photodetector. *Mater. Horiz.* **2020,** *7* (5), 1427-1435.

33. Li, Z.; Wu, J.; Wang, C.; Zhang, H.; Yu, W.; Lu, Y.; Liu, X., High-Performance Monolayer MoS_2 Photodetector Enabled by Oxide Stress Liner using Scalable Chemical Vapor Growth Method. *Nanophotonics* **2020,** *9* (7), 1981-1991.

34. Kim, D. B.; Han, J.; Jung, Y. S.; Park, K. S.; Park, Y.; Heo, J.; Cho, Y. S., Origin of the Anisotropic-Strain-Driven Photoresponse Enhancement in Inorganic Halide-Based Self-Powered Flexible Photodetectors. *Mater. Horiz.* **2022,** *9* (4), 1207-1215.

35. Peng, W.; Wang, X.; Yu, R.; Dai, Y.; Zou, H.; Wang, A. C.; He, Y.; Wang, Z. L., Enhanced Performance of a Self-Powered Organic/Inorganic Photodetector by Pyro-Phototronic and Piezo-Phototronic Effects. *Adv. Mater.* **2017,** *29* (23), 1606698.

36. Liu, K.; Sakurai, M.; Aono, M.; Shen, D., Ultrahigh-Gain Single SnO_2 Microrod Photoconductor on Flexible Substrate with Fast Recovery Speed. *Adv. Funct. Mater.* **2015,** *25* (21), 3157-3163.

37. Ding, M.; Guo, Z.; Chen, X.; Ma, X.; Zhou, L., Surface/Interface Engineering for Constructing Advanced Nanostructured Photodetectors with Improved Performance: A Brief Review. *Nanomaterials* **2020,** *10* (2), 362.

38. Hu, P.; Wang, L.; Yoon, M.; Zhang, J.; Feng, W.; Wang, X.; Wen, Z.; Idrobo, J. C.; Miyamoto, Y.; Geohegan, D. B.; Xiao, K., Highly Responsive Ultrathin GaS Nanosheet Photodetectors on Rigid and Flexible Substrates. *Nano Lett.* **2013,** *13* (4), 1649-1654.

39. Late, D. J.; Liu, B.; Matte, H. S. S. R.; Dravid, V. P.; Rao, C. N. R., Hysteresis in Single-Layer MoS_2 Field Effect Transistors. *ACS Nano* **2012,** *6* (6), 5635-5641.

40. Nagashio, K.; Yamashita, T.; Nishimura, T.; Kita, K.; Toriumi, A., Electrical Transport Properties of Graphene on SiO_2 with Specific Surface Structures. *J. Appl. Phys.* **2011,** *110* (2), 024513.

41. Cui, S.; Mei, Z.; Zhang, Y.; Liang, H.; Du, X., Room-Temperature Fabricated Amorphous Ga_2O_3 High-Response-Speed Solar-Blind Photodetector on Rigid and Flexible Substrates. *Adv. Opt. Mater.* **2017,** *5* (19), 1700454.

42. E, W.; Li, M.; Meng, D.; Cheng, Y.; Fu, W.; Ye, P.; He, Y., High-Performance Amorphous BeZnO-Alloy-Based Solar-Blind Ultraviolet Photodetectors on Rigid and Flexible Substrates. *J. Alloys Compd.* **2020,** *831*, 154819.

43. Cadatal-Raduban, M.; Kato, T.; Horiuchi, Y.; Olejníček, J.; Kohout, M.; Yamanoi, K.; Ono, S., Effect of Substrate and Thickness on the Photoconductivity of Nanoparticle Titanium Dioxide Thin Film Vacuum Ultraviolet Photoconductive Detector. *Nanomaterials* **2022,** *12* (1), 10.

44. Gao, L.; Ma, C.; Wei, S.; Kuklin, A. V.; Zhang, H.; Ågren, H., Applications of Few-Layer Nb_2C MXene: Narrow-Band Photodetectors and Femtosecond Mode-Locked Fiber Lasers. *ACS Nano* **2021,** *15* (1), 954-965.

45. Konstantatos, G.; Sargent, E. H., PbS Colloidal Quantum Dot Photoconductive Photodetectors: Transport, Traps, and Gain. *Appl. Phys. Lett.* **2007,** *91* (17), 173505.

46. European Research Council, Coupled Organic Inorganic Nanostructures for Fast, Light-Induced Data Processing - Fact Sheet, 2020, URL: https://cordis.europa.eu/project/id/802822; date accessed: 20.04.2022.

47. EDMA COINFLIP Project by Dr. Marcus Scheele: Coupled Organic-Inorganic Nanostructures for Fast, Light-Induced Data Processing, URL: https://www.europeandissemination.eu/coinflip-project-by-dr-marcus-scheele/4009, date accessed: 20.04.2022.

48. Scheele, M. Coupled Organic-Inorganic Nanostructures for Fast, Light-Induced Data Processing, URL: https://uni-tuebingen.de/fakultaeten/mathematisch-naturwissenschaftliche-fakultaet/fachbereiche/chemie/institute/physikalische-chemie/professoren/ag-scheele/welcome/current-projects/coupled-organic-inorganic-nanostructures-for-fast-light-induced-data-processing/; date accessed: 20.04.2022.

49. Schedel, C.; Strauß, F.; Kumar, K.; Maier, A.; Wurst, K. M.; Michel, P.; Scheele, M., Substrate Effects on the Bandwidth of CdSe Quantum Dot Photodetectors. *ACS Appl. Mater. Interfaces* **2021,** *13* (40), 47954-47961.

50. Schedel, C.; Strauß, F.; Kohlschreiber, P.; Geladari, O.; Meixner, A. J.; Scheele, M., Substrate Effects on the Speed Limiting Factor of WSe_2 Photodetectors. *Phys. Chem. Chem. Phys.* **2022,** *24* (41), 25383-25390.

51. Saleh, B. E. A.; Teich, M. C., Semiconductor Photon Detectors. In *Fundamentals of Photonics*, Goodman, J. W., Ed. John Wiley Sons, Inc.: 1991.

52. Sze, S. M.; Kg, K. K., *Physics of Semiconductor Devices*. 3. ed.; John Wiley & Sons, Inc.: Hoboken, New Jersey, 2007.

53. Norton, P. R., Photodetectors. In *Handbook of Optics - Volume I: Fundamentals, Techniques, and Design*, 2 ed.; Bass, M.; Van Stryland, E. W.; Williams, D. R.; Wolfe, W. L., Eds. McGraw-Hill, Inc.: 1995.

54. Wolfe, W. L.; Kruse, P. W., Thermal Detectors. In *Handbook of Optics - Volume I: Fundamentals, Techniques, and Design*, 2 ed.; Bass, M.; van Stryland, E. W.; Williams, D. R.; Wolfe, W. L., Eds. McGraw-Hill, Inc: 1995.

55. Winstel, G.; Weyrich, C., *Optoelektronik II - Photodioden, Phototransistoren, Photoleiter und Bildsensoren*. Springer-Verlag Berlin Heidelberg: 1986.

56. Herrmann, K. H., *Der Photoeffekt - Grundlagen der Strahlungsmessung*. Friedr. Vieweg & Sohn Verlagsgesellschaft mbH, Braunschweig / Wiesbaden: 1994.

57. Göbel, H., *Einführung in die Halbleiter-Schaltungstechnik*. 6. ed.; Springer-Verlag GmbH Deutschland: 2019.

58. Joshi, A. M.; Olsen, G. H., Photodetection. In *Handbook of Optics - Volume I: Fundamentals, Techniques, and Design*, 2 ed.; Bass, M.; Van Stryland, E. W.; Williams, D. R.; Wolfe, W. L., Eds. McGraw-Hill, Inc.: 1995.

59. Saleh, B. E. A.; Teich, M. C., Photons in Semiconductors. In *Fundamentals of Photonics*, John Wiley & Sons, Inc. : 1991.

60. Czycholl, G., *Theoretische Festkörperphysik Band 1 - Grundlagen: Phononen und Elektronen in Kristallen*. 4 ed.; Springer-Verlag Berlin Heidelberg: 2016.

61. Demtröder, W., *Experimentalphysik 3 - Atome, Moleküle und Festkörper*. 5 ed.; Springer-Verlag Berlin Heidelberg: 2016.

62. Kitai, A., *Principles of Solar Cells, LEDs and Diodes: The role of the PN junction*. John Wiley & Sons, Ltd: 2011.

63. Bube, R. H., *Photoconductivity of Solids*. John Wiley & Sons, Inc.: New York, London, 1960.

64. Hanbicki, A. T.; Currie, M.; Kioseoglou, G.; Friedman, A. L.; Jonker, B. T., Measurement of High Exciton Binding Energy in the Monolayer Transition-Metal Dichalcogenides WS_2 and WSe_2. *Solid State Commun.* **2015,** *203*, 16-20.

65. Keldysh, L. V., Coulomb Interaction in Thin Semiconductor and Semimetal Films. *JETP Lett.* **1979,** *29* (11), 716-719.

66. De Cremoux, B., PIN Photodiodes for the Visible and Near-Infrared. In *Optoelectronic Sensors*, Decoster, D.; Harari, J., Eds. ISTE Ltd.: London, 2009.

67. Agrawal, G. P., Optical Communication: Its History and Recent Progress. In *Optics in Our Time*, Al-Amri, M. D.; El-Gomati, M.; Zubairy, M. S., Eds. Springer International Publishing: Cham, 2016; pp 177-199.

68. Shen, L.; Fang, Y.; Wang, D.; Bai, Y.; Deng, Y.; Wang, M.; Lu, Y.; Huang, J., A Self-Powered, Sub-Nanosecond-Response Solution-Processed Hybrid Perovskite Photodetector for Time-Resolved Photoluminescence-Lifetime Detection. *Adv. Mater.* **2016,** *28* (48), 10794-10800.

69. Gréboval, C.; Dabard, C.; Konstantinov, N.; Cavallo, M.; Chee, S.-S.; Chu, A.; Dang, T. H.; Khalili, A.; Izquierdo, E.; Prado, Y.; Majjad, H.; Xu, X. Z.; Dayen, J.-F.; Lhuillier, E., Split-Gate Photodiode Based on Graphene/HgTe Heterostructures with a Few Nanosecond Photoresponse. *ACS Appl. Electron. Mater.* **2021,** *3* (11), 4681-4688.

70. Zhao, Z.; Liu, B.; Xie, C.; Ma, Y.; Wang, J.; Liu, M.; Yang, K.; Xu, Y.; Zhang, J.; Li, W.; Shen, L.; Zhang, F., Highly Sensitive, Sub-Microsecond Polymer Photodetectors for Blood Oxygen Saturation Testing. *Sci. China Chem.* **2021,** *64* (8), 1302-1309.

71. Lisakov, S. A.; Pavlov, A. N.; Sypin, E. V. In *High-Speed Flame Detector with the Reduction of Optical Noise by the Compensation Method*, 2015 16th International Conference of Young Specialists on Micro/Nanotechnologies and Electron Devices, Erlagol (Altai Republic), Russia, 29 June-3 July 2015; Erlagol (Altai Republic), Russia, 2015; pp 297-301.

72. Fossum, E. R., Digital Camera System on a Chip. *IEEE Micro* **1998,** *18* (3), 8–15.

73. Saran, R.; Curry, R. J., Lead Sulphide Nanocrystal Photodetector Technologies. *Nat. Photonics* **2016,** *10* (2), 81-92.

74. Omnes, F., Introduction to Semiconductor Photodetectors. In *Optoelectronic Sensors*, ISTE Ltd: London, 2009.

75. Talapin, D. V.; Lee, J.-S.; Kovalenko, M. V.; Shevchenko, E. V., Prospects of Colloidal Nanocrystals for Electronic and Optoelectronic Applications. *Chem. Rev.* **2010,** *110* (1), 389-458.

76. Soole, J. B. D.; Schumacher, H.; LeBlanc, H. P.; Bhat, R.; Koza, M. A., High-Frequency Performance of InGaAs Metal-Semiconductor-Metal Photodetectors at 1.55 and 1.3 μm Wavelengths. *Appl. Phys. Lett.* **1989,** *55* (8), 729-731.

77. Punke, M.; Valouch, S.; Kettlitz, S. W.; Christ, N.; Gärtner, C.; Gerken, M.; Lemmer, U., Dynamic Characterization of Organic Bulk Heterojunction Photodetectors. *Appl. Phys. Lett.* **2007,** *91* (7), 071118.

78. Shimizu, N.; Watanabe, N.; Furuta, T.; Ishibashi, T., InP-InGaAs Uni-Traveling-Carrier Photodiode with Improved 3-dB Bandwidth of Over 150 GHz. *IEEE Photon. Technol. Lett.* **1998,** *10* (3), 412-414.

79. Moglestue, C.; Rosenzweig, J.; Kuhl, J.; Klingenstein, M.; Lambsdorff, M.; Axmann, A.; Schneider, J.; Hülsmann, A., Picosecond Pulse Response Characteristics of GaAs Metal-Semiconductor-Metal Photodetectors. *J. Appl. Phys.* **1991,** *70* (4), 2435-2448.

80. Soole, J. B. D.; Schumacher, H., Transit-Time Limited Frequency Response of InGaAs MSM Photodetectors. *IEEE Trans. Electron Devices* **1990,** *37* (11), 2285-2291.

81. Chen, X.; Nabet, B.; Quaranta, F.; Cola, A.; Currie, M., Resonant-Cavity-Enhanced Heterostructure Metal–Semiconductor–Metal Photodetector. *Appl. Phys. Lett.* **2002,** *80* (17), 3222-3224.

82. Gallo, E. M.; Cola, A.; Quaranta, F.; Spanier, J. E., High Speed Photodetectors Based on a Two-Dimensional Electron/Hole Gas Heterostructure. *Appl. Phys. Lett.* **2013,** *102* (16), 161108.

83. Peumans, P.; Bulović, V.; Forrest, S. R., Efficient, High-Bandwidth Organic Multilayer Photodetectors. *Appl. Phys. Lett.* **2000,** *76* (26), 3855-3857.

84. OSI Optoelectronics, Application Note - Photodiode Characteristics and Application. *www.osioptoelectronics.com, URL: http://www.osioptoelectronics.com/application-notes/AN-Photodiode-Parameters-and-Characteristics.pdf, date accessed: 30.12.2018.*

85. HAMAMATSU, Technical Note - Si photodiodes. *www.hamamatsu.com;* **2020**.

86. Beneking, H., Gain and Bandwidth of Fast Near-Infrared Photodetectors: A Comparison of Diodes, Phototransistors, and Photoconductive Devices. *IEEE Trans. Electron Devices* **1982,** *29* (9), 1420-1431.

87. General Monitors. How to Select a Flame Detector, URL: https://www.aft.net/wp-content/uploads/2018/10/General-Monitors-Flame-Detector-Selection-Guide.pdf, date accessed: 10.05.2022 undated.

88. Herzallah, S. M., Determination of Aflatoxins in Eggs, Milk, Meat and Meat Products Using HPLC Fluorescent and UV Detectors. *Food Chem.* **2009,** *114* (3), 1141-1146.

89. Blumthaler, M., UV Monitoring for Public Health. *Int. J. of Environ. Res. Public Health* **2018,** *15* (8), 1723.

90. Konstantatos, G.; Clifford, J.; Levina, L.; Sargent, E. H., Sensitive Solution-Processed Visible-Wavelength Photodetectors. *Nat. Photonics* **2007,** *1* (9), 531-534.

91. Fernández, C.; Llorca, D. F.; Sotelo, M. A.; Daza, I. G.; Hellín, A. M.; Álvarez, S., Real-Time Vision-Based Blind Spot Warning System: Experiments with Motorcycles in Daytime/Nighttime Conditions. *Int. J. Automot. Technol.* **2013,** *14* (1), 113-122.

92. Bach, H.-G., Ultrafast Photodetectors and Receivers. In *Optical and Fiber Communications Reports - Ultrahigh-Speed Optical Transmission Technology*, Weber, H.-G.; Nakazawa, M., Eds. Springer Science+Business Media, LLC: New York, USA, 2007.

93. Kim, S.; Lim, Y. T.; Soltesz, E. G.; De Grand, A. M.; Lee, J.; Nakayama, A.; Parker, J. A.; Mihaljevic, T.; Laurence, R. G.; Dor, D. M.; Cohn, L. H.; Bawendi, M. G.; Frangioni, J. V., Near-Infrared Fluorescent Type II Quantum Dots for Sentinel Lymph Node Mapping. *Nat. Biotechnol.* **2004,** *22* (1), 93-97.

94. Corsi, C., Infrared: A Key Technology for Security Systems. *Adv. Opt. Technol.* **2012,** *2012*, 838752.

95. Ramade, J.; Qu, J.; Chu, A.; Gréboval, C.; Livache, C.; Goubet, N.; Martinez, B.; Vincent, G.; Lhuillier, E., Potential of Colloidal Quantum Dot Based Solar Cells for Near-Infrared Active Detection. *ACS Photonics* **2020,** *7* (1), 272-278.

96. Gréboval, C.; Chu, A.; Goubet, N.; Livache, C.; Ithurria, S.; Lhuillier, E., Mercury Chalcogenide Quantum Dots: Material Perspective for Device Integration. *Chem. Rev.* **2021,** *121* (7), 3627-3700.

97. Scavennec, A.; Giraudet, L., Optical Photodetectors. In *Fibre Optic Communication Devices*, Grote, N.; Venghaus, H., Eds. Springer-Verlag Berlin Heidelberg New York: 2001.

98. Lee, J.-S.; Kovalenko, M. V.; Huang, J.; Chung, D. S.; Talapin, D. V., Band-Like Transport, High Electron Mobility and High Photoconductivity in All-Inorganic Nanocrystal Arrays. *Nat. Nanotechnol.* **2011,** *6* (6), 348-352.

99. Guyot-Sionnest, P.; Lhuillier, E.; Liu, H., A Mirage Study of CdSe Colloidal Quantum Dot Films, Urbach Tail, and Surface States. *J. Chem. Phys.* **2012,** *137* (15), 154704.

100. Adinolfi, V.; Kramer, I. J.; Labelle, A. J.; Sutherland, B. R.; Hoogland, S.; Sargent, E. H., Photojunction Field-Effect Transistor Based on a Colloidal Quantum Dot Absorber Channel Layer. *ACS Nano* **2015,** *9* (1), 356-362.

101. Rogalski, A.; Bielecki, Z., Detection of Optical Radiation. *Bull. Pol. Acad. Sci. Tech. Sci.* **2004,** *vol. 52* (No 1), 43-66.

102. Konstantatos, G.; Howard, I.; Fischer, A.; Hoogland, S.; Clifford, J.; Klem, E.; Levina, L.; Sargent, E. H., Ultrasensitive Solution-Cast Quantum Dot Photodetectors. *Nature* **2006,** *442* (7099), 180-183.

103. Bowers, J. E.; Wey, Y. G., High-Speed Photodetectors. In *Handbook of Optics - Volume I: Fundamentals, Techniques, and Design*, Bass, M.; Van Stryland, E. W.; Williams, D. R.; Wolfe, W. L., Eds. McGraw-Hill, Inc.: 1995.

104. Ramo, S., Currents Induced by Electron Motion. *Proc. I.R.E.* **1939,** *27* (9), 584-585.

105. Bowers, J.; Burrus, C., Ultrawide-Band Long-Wavelength p-i-n Photodetectors. *J. Light. Technol.* **1987,** *5* (10), 1339-1350.

106. Otuonye, U.; Kim, H. W.; Lu, W. D., Ge Nanowire Photodetector with High Photoconductive Gain Epitaxially Integrated on Si Substrate. *Appl. Phys. Lett.* **2017,** *110* (17), 173104.

107. Hinds, S.; Levina, L.; Klem, E. J. D.; Konstantatos, G.; Sukhovatkin, V.; Sargent, E. H., Smooth-Morphology Ultrasensitive Solution-Processed Photodetectors. *Adv. Mater.* **2008,** *20* (23), 4398-4402.

108. Buscema, M.; Island, J. O.; Groenendijk, D. J.; Blanter, S. I.; Steele, G. A.; van der Zant, H. S. J.; Castellanos-Gomez, A., Photocurrent Generation with Two-Dimensional Van Der Waals Semiconductors. *Chem. Soc. Rev.* **2015,** *44* (11), 3691-3718.

109. Wadhwa, R.; Agrawal, A. V.; Kumar, M., A Strategic Review of Recent Progress, Prospects and Challenges of MoS_2-Based Photodetectors. *J. Phys. D: Appl. Phys.* **2021,** *55* (6), 063002.

110. Hunklinger, S., *Festkörperphysik*. 4. ed.; Oldenbourg Wissenschaftsverlag GmbH: München, 2014.

111. Choi, W.; Cho, M. Y.; Konar, A.; Lee, J. H.; Cha, G.-B.; Hong, S. C.; Kim, S.; Kim, J.; Jena, D.; Joo, J.; Kim, S., High-Detectivity Multilayer MoS_2 Phototransistors with Spectral Response from Ultraviolet to Infrared. *Adv. Mater.* **2012,** *24* (43), 5832-5836.

112. Harari, J.; Magnin, V., Metal-Semiconductor-Metal Photodiodes. In *Optoelectronic Sensors*, ISTE Ltd: London, 2009; pp 155-180.

113. Bardeen, J., Surface States and Rectification at a Metal Semi-Conductor Contact. *Phys. Rev.* **1947,** *71* (10), 717-727.

114. Xu, Q.; Meng, L.; Sinha, K.; Chowdhury, F. I.; Hu, J.; Wang, X., Ultrafast Colloidal Quantum Dot Infrared Photodiode. *ACS Photonics* **2020,** *7* (5), 1297-1303.

115. Xia, F.; Mueller, T.; Lin, Y.-m.; Valdes-Garcia, A.; Avouris, P., Ultrafast Graphene Photodetector. *Nat. Nanotechnol.* **2009,** *4* (12), 839-843.

116. Nabet, B.; Liou, L.; Paolella, A. In *Transit Time and RC Time Constant Trade-Offs in MSM Photodetectors*, 1993 IEEE Princeton Section Sarnoff Symposium, 26 March 1993; 1993 IEEE Princeton Section Sarnoff Symposium: 1993; pp 0_187-0_191.

117. Goushcha, A.; Tabbert, B., On Response Time of Semiconductor Photodiodes. *Opt. Eng.* **2017,** *56* (9), 097101.

118. Clifford, J. P.; Konstantatos, G.; Johnston, K. W.; Hoogland, S.; Levina, L.; Sargent, E. H., Fast, Sensitive and Spectrally Tuneable Colloidal-Quantum-Dot Photodetectors. *Nat. Nanotechnol.* **2009,** *4* (1), 40-44.

119. Naftaly, M.; Das, S.; Gallop, J.; Pan, K.; Alkhalil, F.; Kariyapperuma, D.; Constant, S.; Ramsdale, C.; Hao, L., Sheet Resistance Measurements of Conductive Thin Films: A Comparison of Techniques. *Electronics* **2021,** *10* (8), 960.

120. Young, J. F.; van Driel, H. M., Ambipolar Diffusion of High-Density Electrons and Holes in Ge, Si, and GaAs: Many-Body Effects. *Phys. Rev. B* **1982,** *26* (4), 2147-2158.

121. Xu, G. Y.; Salvador, A.; Kim, W.; Fan, Z.; Lu, C.; Tang, H.; Morkoç, H.; Smith, G.; Estes, M.; Goldenberg, B.; Yang, W.; Krishnankutty, S., High Speed, Low Noise Ultraviolet Photodetectors Based on GaN p-i-n and AlGaN(p)-GaN(i)-GaN(n) Structures. *Appl. Phys. Lett.* **1997,** *71* (15), 2154-2156.

122. Forrest, S. R.; Kim, O. K.; Smith, R. G., Optical Response Time of $In_{0.53}Ga_{0.47}As/InP$ Avalanche Photodiodes. *Appl. Phys. Lett.* **1982,** *41* (1), 95-98.

123. Das, N. R.; Deen, M. J., Calculating the Photocurrent and Transit-Time-Limited Bandwidth of a Heterostructure p-i-n Photodetector. *IEEE J. Quantum Electron.* **2001,** *37* (12), 1574-1587.

124. Kashiwaba, Y.; Kanno, I.; Ikeda, T., p-Type Characteristics of Cu-Doped CdS Thin Films. *Jpn. J. Appl. Phys.* **1992,** *31* (Part 1, No. 4), 1170-1175.

125. Ogawa, H.; Irfan, G. S.; Nakayama, H.; Nishio, M.; Yoshida, A., Growth of Low-Resistivity n-Type ZnTe by Metalorganic Vapor Phase Epitaxy. *Jpn. J. Appl. Phys.* **1994,** *33* (Part 2, No. 7B), L980-L982.

126. Yu, L. S.; Xing, Q. J.; Qiao, D.; Lau, S. S.; Boutros, K. S.; Redwing, J. M., Internal Photoemission Measurement of Schottky Barrier Height for Ni on AlGaN/GaN Heterostructure. *Appl. Phys. Lett.* **1998,** *73* (26), 3917-3919.

127. Hong, T.; Chamlagain, B.; Hu, S.; Weiss, S. M.; Zhou, Z.; Xu, Y.-Q., Plasmonic Hot Electron Induced Photocurrent Response at MoS_2–Metal Junctions. *ACS Nano* **2015,** *9* (5), 5357-5363.

128. Chou, S. Y.; Liu, Y.; Fischer, P. B., Fabrication of Sub-50 nm Finger Spacing and Width High-Speed Metal–Semiconductor–Metal Photodetectors Using High-Resolution Electron Beam Lithography and Molecular Beam Epitaxy. *J. Vac. Sci. Technol. B* **1991,** *9* (6), 2920-2924.

129. Klingenstein, M.; Kuhl, J.; Rosenzweig, J.; Moglestue, C.; Hülsmann, A.; Schneider, J.; Köhler, K., Photocurrent Gain Mechanisms in Metal-Semiconductor-Metal Photodetectors. *Solid-State Electron.* **1994,** *37* (2), 333-340.

130. Gonzalez, C.; Marty, A., Phototransistors. In *Optoelectronic Sensors*, Decoster, D.; Harari, J., Eds. ISTE Ltd: London, 2009; pp 111-154.

131. Monier, C.; Fan, R.; Jung, H.; Ping-Chih, C.; Shul, R. J.; Kyu-Pil, L.; Anping, Z.; Baca, A. G.; Pearton, S., Simulation of npn and pnp AlGaN/GaN Heterojunction Bipolar Transistors Performances: Limiting Factors and Optimum Design. *IEEE Trans. Electron Devices* **2001,** *48* (3), 427-432.

132. Otto, T.; Miller, C.; Tolentino, J.; Liu, Y.; Law, M.; Yu, D., Gate-Dependent Carrier Diffusion Length in Lead Selenide Quantum Dot Field-Effect Transistors. *Nano Lett.* **2013,** *13* (8), 3463-3469.

133. Livache, C.; Izquierdo, E.; Martinez, B.; Dufour, M.; Pierucci, D.; Keuleyan, S.; Cruguel, H.; Becerra, L.; Fave, J. L.; Aubin, H.; Ouerghi, A.; Lacaze, E.; Silly, M. G.; Dubertret, B.; Ithurria, S.; Lhuillier, E., Charge Dynamics and Optolectronic Properties in HgTe Colloidal Quantum Wells. *Nano Lett.* **2017,** *17* (7), 4067-4074.

134. Lee, A. Y.; Ra, H.-S.; Kwak, D.-H.; Jeong, M.-H.; Park, J.-H.; Kang, Y.-S.; Chae, W.-S.; Lee, J.-S., Hybrid Black Phosphorus/Zero-Dimensional Quantum Dot Phototransistors:

Tunable Photodoping and Enhanced Photoresponsivity. *ACS Appl. Mater. Interfaces* **2018,** *10* (18), 16033-16040.

135. Yin, Z.; Li, H.; Li, H.; Jiang, L.; Shi, Y.; Sun, Y.; Lu, G.; Zhang, Q.; Chen, X.; Zhang, H., Single-Layer MoS_2 Phototransistors. *ACS Nano* **2012,** *6* (1), 74-80.

136. Yi, Y.; Wu, C.; Liu, H.; Zeng, J.; He, H.; Wang, J., A Study of Lateral Schottky Contacts in WSe_2 and MoS_2 Field Effect Transistors Using Scanning Photocurrent Microscopy. *Nanoscale* **2015,** *7* (38), 15711-15718.

137. Giraud, P.; Hou, B.; Pak, S.; Sohn, J. I.; Morris, S.; Cha, S.; Kim, J. M., Field Effect Transistors and Phototransistors Based upon p-Type Solution-Processed PbS Nanowires. *Nanotechnology* **2018,** *29* (7), 075202.

138. Mir, W. J.; Livache, C.; Goubet, N.; Martinez, B.; Jagtap, A.; Chu, A.; Coutard, N.; Cruguel, H.; Barisien, T.; Ithurria, S.; Nag, A.; Dubertret, B.; Ouerghi, A.; Silly, M. G.; Lhuillier, E., Strategy to Overcome Recombination Limited Photocurrent Generation in $CsPbX_3$ Nanocrystal Arrays. *Appl. Phys. Lett.* **2018,** *112* (11), 113503.

139. Adhikari, P.; Kobbekaduwa, K.; Shi, Y.; Zhang, J.; Abass, N. A.; He, J.; Rao, A.; Gao, J., Sub-50 Picosecond to Microsecond Carrier Transport Dynamics in Pentacene Thin Films. *Appl. Phys. Lett.* **2018,** *113* (18), 183509.

140. Martinez, B.; Livache, C.; Goubet, N.; Jagtap, A.; Cruguel, H.; Ouerghi, A.; Lacaze, E.; Silly, M. G.; Lhuillier, E., Probing Charge Carrier Dynamics to Unveil the Role of Surface Ligands in HgTe Narrow Band Gap Nanocrystals. *J. Phys. Chem. C* **2018,** *122* (1), 859-865.

141. Livache, C.; Goubet, N.; Martinez, B.; Jagtap, A.; Qu, J.; Ithurria, S.; Silly, M. G.; Dubertret, B.; Lhuillier, E., Band Edge Dynamics and Multiexciton Generation in Narrow Band Gap HgTe Nanocrystals. *ACS Appl. Mater. Interfaces* **2018,** *10* (14), 11880-11887.

142. Day, J.; Subramanian, S.; Anthony, J. E.; Lu, Z.; Twieg, R. J.; Ostroverkhova, O., Photoconductivity in Organic Thin Films: From Picoseconds to Seconds after Excitation. *J. Appl. Phys.* **2008,** *103* (12), 123715.

143. Yu, G.; Phillips, S. D.; Tomozawa, H.; Heeger, A. J., Subnanosecond Transient Photoconductivity in Poly(3-hexylthiophene). *Phys. Rev. B* **1990,** *42* (5), 3004-3010.

144. Gréboval, C.; Izquierdo, E.; Livache, C.; Martinez, B.; Dufour, M.; Goubet, N.; Moghaddam, N.; Qu, J.; Chu, A.; Ramade, J.; Aubin, H.; Cruguel, H.; Silly, M.; Lhuillier, E.; Ithurria, S., Impact of Dimensionality and Confinement on the Electronic Properties of Mercury Chalcogenide Nanocrystals. *Nanoscale* **2019,** *11* (9), 3905-3915.

145. Christ, N.; Kettlitz, S.; Mescher, J.; Valouch, S.; Lemmer, U., Dispersive Transport in the Temperature Dependent Transient Photoresponse of Organic Photodiodes and Solar Cells. *J. Appl. Phys.* **2013,** *113* (23), 234503.

146. Hvam, J. M.; Brodsky, M. H., Dispersive Transport and Recombination Lifetime in Phosphorus-Doped Hydrogenated Amorphous Silicon. *Phys. Rev. Lett.* **1981,** *46* (5), 371-374.

147. Christ, N.; Kettlitz, S. W.; Mescher, J.; Lemmer, U., Extracting the Charge Carrier Mobility from the Nanosecond Photocurrent Response of Organic Solar Cells and Photodiodes. *Appl. Phys. Lett.* **2014,** *104* (5), 053302.

148. Orenstein, J.; Kastner, M., Photocurrent Transient Spectroscopy: Measurement of the Density of Localized States in α-As_2Se_3. *Phys. Rev. Lett.* **1981,** *46* (21), 1421-1424.

149. Orenstein, J.; Kastner, M. A.; Vaninov, V., Transient Photoconductivity and Photo-Induced Optical Absorption in Amorphous Semiconductors. *Philos. Mag., B* **1982,** *46* (1), 23-62.

150. Tiedje, T.; Cebulka, J. M.; Morel, D. L.; Abeles, B., Evidence for Exponential Band Tails in Amorphous Silicon Hydride. *Phys. Rev. Lett.* **1981,** *46* (21), 1425-1428.

151. Tiedje, T.; Rose, A., A Physical Interpretation of Dispersive Transport in Disordered Semiconductors. *Solid State Commun.* **1981,** *37* (1), 49-52.

152. Main, C., Determination of the Density of States in Semiconductors from Transient Photoconductivity. *Mat. Res. Soc. Symp. Proc.* **1997,** *467*, 167.

153. Monroe, D.; Kastner, M. A., Exactly Exponential Band Tail in a Glassy Semiconductor. *Phys. Rev. B* **1986,** *33* (12), 8881-8884.

154. Urbach, F., The Long-Wavelength Edge of Photographic Sensitivity and of the Electronic Absorption of Solids. *Phys. Rev.* **1953,** *92* (5), 1324-1324.

155. Beaudoin, M.; DeVries, A. J. G.; Johnson, S. R.; Laman, H.; Tiedje, T., Optical Absorption Edge of Semi-Insulating GaAs and InP at High Temperatures. *Appl. Phys. Lett.* **1997,** *70* (26), 3540-3542.

156. Studenyak, I.; Kranjčec, M.; Kurik, M. V., Urbach Rule in Solid State Physics. *Int. J. Opt. Appl.* **2014,** *4* (3), 76-83.

157. Liang, S.; Dai, Y.; Wang, G.; Xia, H.; Zhao, J., Room-Temperature Fabrication of SiC Microwire Photodetectors on Rigid and Flexible Substrates via Femtosecond Laser Direct Writing. *Nanoscale* **2020,** *12* (45), 23200-23205.

158. Octon, T. J.; Nagareddy, V. K.; Russo, S.; Craciun, M. F.; Wright, C. D., Fast High-Responsivity Few-Layer $MoTe_2$ Photodetectors. *Adv. Opt. Mater.* **2016,** *4* (11), 1750-1754.

159. Georgiadou, D. G.; Lin, Y.-H.; Lim, J.; Ratnasingham, S.; McLachlan, M. A.; Snaith, H. J.; Anthopoulos, T. D., High Responsivity and Response Speed Single-Layer Mixed-Cation Lead Mixed-Halide Perovskite Photodetectors Based on Nanogap Electrodes Manufactured on Large-Area Rigid and Flexible Substrates. *Adv. Funct. Mater.* **2019,** *29* (28), 1901371.

160. Özdemir, O.; Ramiro, I.; Gupta, S.; Konstantatos, G., High Sensitivity Hybrid PbS CQD-TMDC Photodetectors up to 2 µm. *ACS Photonics* **2019,** *6* (10), 2381-2386.

161. Sukhovatkin, V.; Hinds, S.; Brzozowski, L.; Sargent, E. H., Colloidal Quantum-Dot Photodetectors Exploiting Multiexciton Generation. *Science* **2009,** *324* (5934), 1542.

162. Oertel, D. C.; Bawendi, M. G.; Arango, A. C.; Bulović, V., Photodetectors Based on Treated CdSe Quantum-Dot Films. *Appl. Phys. Lett.* **2005,** *87* (21), 213505.

163. Tetsuka, H.; Nagoya, A.; Tamura, S.-i., Graphene/Nitrogen-Functionalized Graphene Quantum Dot Hybrid Broadband Photodetectors with a Buffer Layer of Boron Nitride Nanosheets. *Nanoscale* **2016,** *8* (47), 19677-19683.

164. Zhang, S.; Cyr, P. W.; McDonald, S. A.; Konstantatos, G.; Sargent, E. H., Enhanced Infrared Photovoltaic Efficiency in PbS Nanocrystal/Semiconducting Polymer Composites: 600-Fold Increase in Maximum Power Output via Control of the Ligand Barrier. *Appl. Phys. Lett.* **2005,** *87* (23), 233101.

165. Goubet, N.; Livache, C.; Martinez, B.; Xu, X. Z.; Ithurria, S.; Royer, S.; Cruguel, H.; Patriarche, G.; Ouerghi, A.; Silly, M.; Dubertret, B.; Lhuillier, E., Wave-Function Engineering in HgSe/HgTe Colloidal Heterostructures To Enhance Mid-infrared Photoconductive Properties. *Nano Lett.* **2018,** *18* (7), 4590-4597.

166. Kim, J.; Oh, E.; Xiao, R.; Ritter, S.; Yang, Y.; Yu, D.; Hee Im, J.; Hyuk Kim, S.; Jun Choi, W.; Park, J.-G., Optical Properties and Bridge Photodetector Integration of Lead Sulfide Nanowires. *Nanotechnology* **2017,** *28* (47), 475706.

167. Ozden, B.; Khanal, M. P.; Mirkhani, V.; Yapabandara, K.; Yang, C.; Ko, S.; Youn, S.; Hamilton, M. C.; Sk, M. H.; Ahyi, A. C.; Park, M., Time-Resolved Photocurrent Spectroscopic Diagnostics of Electrically Active Defects in AlGaN/GaN High Electron Mobility Transistor (HEMT) Structure Grown on Si Wafers. *J. Nanosci. Nanotechnol.* **2016,** *16* (7), 7630–7634.

168. Osedach, T. P.; Zhao, N.; Geyer, S. M.; Chang, L.-Y.; Wanger, D. D.; Arango, A. C.; Bawendi, M. C.; Bulović, V., Interfacial Recombination for Fast Operation of a Planar Organic/QD Infrared Photodetector. *Adv. Mater.* **2010,** *22* (46), 5250-5254.

169. Ghosh, S.; Hoogland, S.; Sukhovatkin, V.; Levina, L.; Sargent, E. H., A Tunable Colloidal Quantum Dot Photo Field-Effect Transistor. *Appl. Phys. Lett.* **2011,** *99* (10), 101102.

170. Ackerman, M. M.; Tang, X.; Guyot-Sionnest, P., Fast and Sensitive Colloidal Quantum Dot Mid-Wave Infrared Photodetectors. *ACS Nano* **2018,** *12* (7), 7264-7271.

171. Hanrath, T., Colloidal Nanocrystal Quantum Dot Assemblies as Artificial Solids. *J. Vac. Sci. Technol. A* **2012,** *30* (3), 030802.

172. Göpel, W.; Ziegler, C., *Einführung in die Materialwissenschaften: Physikalisch-chemische Grundlagen und Anwendungen*. B. G. Teubner Vertragsgesellschaft: Leipzig, 1996.

173. Murray, C. B.; Norris, D. J.; Bawendi, M. G., Synthesis and Characterization of Nearly Monodisperse CdE (E = Sulfur, Selenium, Tellurium) Semiconductor Nanocrystallites. *J. Am. Chem. Soc.* **1993,** *115* (19), 8706-8715.

174. Talapin, D. V.; Rogach, A. L.; Kornowski, A.; Haase, M.; Weller, H., Highly Luminescent Monodisperse CdSe and CdSe/ZnS Nanocrystals Synthesized in a Hexadecylamine−Trioctylphosphine Oxide−Trioctylphospine Mixture. *Nano Lett.* **2001,** *1* (4), 207-211.

175. Sayevich, V.; Guhrenz, C.; Dzhagan, V. M.; Sin, M.; Werheid, M.; Cai, B.; Borchardt, L.; Widmer, J.; Zahn, D. R.; Brunner, E.; Lesnyak, V.; Gaponik, N.; Eychmüller, A., Hybrid N-Butylamine-Based Ligands for Switching the Colloidal Solubility and Regimentation of Inorganic-Capped Nanocrystals. *ACS Nano* **2017,** *11* (2), 1559-1571.

176. Zhang, H.; Jang, J.; Liu, W.; Talapin, D. V., Colloidal Nanocrystals with Inorganic Halide, Pseudohalide, and Halometallate Ligands. *ACS Nano* **2014,** *8* (7), 7359-7369.

177. Liu, Y.; Gibbs, M.; Puthussery, J.; Gaik, S.; Ihly, R.; Hillhouse, H. W.; Law, M., Dependence of Carrier Mobility on Nanocrystal Size and Ligand Length in PbSe Nanocrystal Solids. *Nano Lett.* **2010,** *10* (5), 1960-1969.

178. Majetich, S. A.; Carter, A. C.; McCullough, R. D.; Seth, J.; Belot, J. A., Connected CdSe Nanocrystallite Networks. *Z. Phys. D* **1993,** *26* (1), 210-212.

179. Scheele, M.; Hanifi, D.; Zherebetskyy, D.; Chourou, S. T.; Axnanda, S.; Rancatore, B. J.; Thorkelsson, K.; Xu, T.; Liu, Z.; Wang, L.-W.; Liu, Y.; Alivisatos, A. P., PbS Nanoparticles Capped with Tetrathiafulvalenetetracarboxylate: Utilizing Energy Level Alignment for Efficient Carrier Transport. *ACS Nano* **2014,** *8* (3), 2532-2540.

180. Szendrei, K.; Jarzab, D.; Yarema, M.; Sytnyk, M.; Pichler, S.; Hummelen, J. C.; Heiss, W.; Loi, M. A., Surface Modification of Semiconductor Nanocrystals by a Methanofullerene Carboxylic Acid. *J. Mater. Chem.* **2010,** *20* (39), 8470-8473.

181. Scheele, M.; Brütting, W.; Schreiber, F., Coupled Organic-Inorganic Nanostructures (COIN). *Phys. Chem. Chem. Phys.* **2015,** *17* (1), 97-111.

182. Kagan, C. R.; Lifshitz, E.; Sargent, E. H.; Talapin, D. V., Building Devices from Colloidal Quantum Dots. *Science* **2016,** *353* (6302), aac5523.

183. Dolzhnikov, D. S.; Zhang, H.; Jang, J.; Son, J. S.; Panthani, M. G.; Shibata, T.; Chattopadhyay, S.; Talapin, D. V., Composition-Matched Molecular "Solders" for Semiconductors. *Science* **2015,** *347* (6220), 425-428.

184. Yu, W. W.; Qu, L.; Guo, W.; Peng, X., Experimental Determination of the Extinction Coefficient of CdTe, CdSe, and CdS Nanocrystals. *Chem. Mater.* **2003,** *15* (14), 2854-2860.

185. Konstantatos, G.; Sargent, E. H., Nanostructured Materials for Photon Detection. *Nat. Nanotechnol.* **2010,** *5* (6), 391-400.

186. Kucur, E.; Riegler, J.; Urban, G. A.; Nann, T., Determination of Quantum Confinement in CdSe Nanocrystals by Cyclic Voltammetry. *J. Chem. Phys.* **2003,** *119* (4), 2333-2337.

187. Jasieniak, J.; Califano, M.; Watkins, S. E., Size-Dependent Valence and Conduction Band-Edge Energies of Semiconductor Nanocrystals. *ACS Nano* **2011,** *5* (7), 5888-5902.

188. Querner, C.; Reiss, P.; Sadki, S.; Zagorska, M.; Pron, A., Size and Ligand Effects on the Electrochemical and Spectroelectrochemical Responses of CdSe Nanocrystals. *Phys. Chem. Chem. Phys.* **2005,** *7* (17), 3204-3209.

189. Soreni-Harari, M.; Yaacobi-Gross, N.; Steiner, D.; Aharoni, A.; Banin, U.; Millo, O.; Tessler, N., Tuning Energetic Levels in Nanocrystal Quantum Dots Through Surface Manipulations. *Nano Lett.* **2008,** *8* (2), 678-684.

190. Brown, P. R.; Kim, D.; Lunt, R. R.; Zhao, N.; Bawendi, M. G.; Grossman, J. C.; Bulović, V., Energy Level Modification in Lead Sulfide Quantum Dot Thin Films through Ligand Exchange. *ACS Nano* **2014,** *8* (6), 5863-5872.

191. Baker, D. R.; Kamat, P. V., Tuning the Emission of CdSe Quantum Dots by Controlled Trap Enhancement. *Langmuir* **2010,** *26* (13), 11272-11276.

192. Xu, F.; Gerlein, L. F.; Ma, X.; Haughn, C. R.; Doty, M. F.; Cloutier, S. G., Impact of Different Surface Ligands on the Optical Properties of PbS Quantum Dot Solids. *Materials* **2015,** *8* (4), 1858-1870.

193. Dirin, D. N.; Dreyfuss, S.; Bodnarchuk, M. I.; Nedelcu, G.; Papagiorgis, P.; Itskos, G.; Kovalenko, M. V., Lead Halide Perovskites and Other Metal Halide Complexes As Inorganic Capping Ligands for Colloidal Nanocrystals. *J. Am. Chem. Soc.* **2014,** *136* (18), 6550-6553.

194. Majetich, S. A.; Carter, A. C., Surface Effects on the Optical Properties of Cadmium Selenide Quantum Dots. *J. Phys. Chem.* **1993,** *97* (34), 8727-8731.

195. Katari, J. E. B.; Colvin, V. L.; Alivisatos, A. P., X-Ray Photoelectron Spectroscopy of CdSe Nanocrystals with Applications to Studies of the Nanocrystal Surface. *J. Phys. Chem.* **1994,** *98* (15), 4109-4117.

196. Tan, Y.; Jin, S.; Hamers, R. J., Photostability of CdSe Quantum Dots Functionalized with Aromatic Dithiocarbamate Ligands. *ACS Appl. Mater. Interfaces* **2013,** *5* (24), 12975-12983.

197. Kumar, K.; Liu, Q.; Hiller, J.; Schedel, C.; Maier, A.; Meixner, A.; Braun, K.; Lauth, J.; Scheele, M., Fast, Infrared-Active Optical Transistors Based on Dye-Sensitized CdSe Nanocrystals. *ACS Appl. Mater. Interfaces* **2019,** *11* (51), 48271-48280.

198. Castellanos-Gomez, A.; Buscema, M.; Molenaar, R.; Singh, V.; Janssen, L.; van der Zant, H. S. J.; Steele, G. A., Deterministic Transfer of Two-Dimensional Materials by All-Dry Viscoelastic Stamping. *2D Mater.* **2014,** *1* (1), 011002.

199. Meitl, M. A.; Zhu, Z.-T.; Kumar, V.; Lee, K. J.; Feng, X.; Huang, Y. Y.; Adesida, I.; Nuzzo, R. G.; Rogers, J. A., Transfer Printing by Kinetic Control of Adhesion to an Elastomeric Stamp. *Nat. Mater.* **2006,** *5* (1), 33-38.

200. Wang, Q. H.; Kalantar-Zadeh, K.; Kis, A.; Coleman, J. N.; Strano, M. S., Electronics and Optoelectronics of Two-Dimensional Transition Metal Dichalcogenides. *Nat. Nanotechnol.* **2012,** *7* (11), 699-712.

201. Castellanos-Gomez, A.; Poot, M.; Steele, G. A.; van der Zant, H. S. J.; Agraït, N.; Rubio-Bollinger, G., Elastic Properties of Freely Suspended MoS_2 Nanosheets. *Adv. Mater.* **2012,** *24* (6), 772-775.

202. Zhang, R.; Koutsos, V.; Cheung, R., Elastic Properties of Suspended Multilayer WSe_2. *Appl. Phys. Lett.* **2016,** *108* (4), 042104.

203. Wang, H.; Yuan, H.; Sae Hong, S.; Li, Y.; Cui, Y., Physical and Chemical Tuning of Two-Dimensional Transition Metal Dichalcogenides. *Chem. Soc. Rev.* **2015,** *44* (9), 2664-2680.

204. Chhowalla, M.; Shin, H. S.; Eda, G.; Li, L.-J.; Loh, K. P.; Zhang, H., The Chemistry of Two-Dimensional Layered Transition Metal Dichalcogenide Nanosheets. *Nat. Chem.* **2013,** *5* (4), 263-275.

205. Podzorov, V.; Gershenson, M. E.; Kloc, C.; Zeis, R.; Bucher, E., High-Mobility Field-Effect Transistors Based on Transition Metal Dichalcogenides. *Appl. Phys. Lett.* **2004,** *84* (17), 3301-3303.

206. Pudasaini, P. R.; Oyedele, A.; Zhang, C.; Stanford, M. G.; Cross, N.; Wong, A. T.; Hoffman, A. N.; Xiao, K.; Duscher, G.; Mandrus, D. G.; Ward, T. Z.; Rack, P. D., High-Performance Multilayer WSe_2 Field-Effect Transistors with Carrier Type Control. *Nano Res.* **2018,** *11* (2), 722-730.

207. Radisavljevic, B.; Radenovic, A.; Brivio, J.; Giacometti, V.; Kis, A., Single-Layer MoS_2 Transistors. *Nat. Nanotechnol.* **2011,** *6* (3), 147-150.

208. Fang, H.; Chuang, S.; Chang, T. C.; Takei, K.; Takahashi, T.; Javey, A., High-Performance Single Layered WSe_2 p-FETs with Chemically Doped Contacts. *Nano Lett.* **2012,** *12* (7), 3788-3792.

209. Sun, Y.; Wang, D.; Shuai, Z., Indirect-to-Direct Band Gap Crossover in Few-Layer Transition Metal Dichalcogenides: A Theoretical Prediction. *J. Phys. Chem. C* **2016,** *120* (38), 21866-21870.

210. Mak, K. F.; Lee, C.; Hone, J.; Shan, J.; Heinz, T. F., Atomically Thin MoS_2: A New Direct-Gap Semiconductor. *Phys. Rev. Lett.* **2010,** *105* (13), 136805.

211. Kumar, A.; Ahluwalia, P. K., Electronic Structure of Transition Metal Dichalcogenides Monolayers 1H-MX_2 (M = Mo, W; X = S, Se, Te) from Ab-Initio Theory: New Direct Band Gap Semiconductors. *Eur. Phys. J. B* **2012,** *85* (6), 186.

212. Lee, H. S.; Min, S.-W.; Chang, Y.-G.; Park, M. K.; Nam, T.; Kim, H.; Kim, J. H.; Ryu, S.; Im, S., MoS_2 Nanosheet Phototransistors with Thickness-Modulated Optical Energy Gap. *Nano Lett.* **2012,** *12* (7), 3695-3700.

213. Zhou, C.; Zhao, Y.; Raju, S.; Wang, Y.; Lin, Z.; Chan, M.; Chai, Y., Carrier Type Control of WSe_2 Field-Effect Transistors by Thickness Modulation and MoO_3 Layer Doping. *Adv. Funct. Mater.* **2016,** *26* (23), 4223-4230.

214. Sahin, H.; Tongay, S.; Horzum, S.; Fan, W.; Zhou, J.; Li, J.; Wu, J.; Peeters, F. M., Anomalous Raman Spectra and Thickness-Dependent Electronic Properties of WSe_2. *Phys. Rev. B* **2013,** *87* (16), 165409.

215. Zhou, H.; Wang, C.; Shaw, J. C.; Cheng, R.; Chen, Y.; Huang, X.; Liu, Y.; Weiss, N. O.; Lin, Z.; Huang, Y.; Duan, X., Large Area Growth and Electrical Properties of p-Type WSe_2 Atomic Layers. *Nano Lett.* **2015,** *15* (1), 709-713.

216. Pei, J.; Yang, J.; Yildirim, T.; Zhang, H.; Lu, Y., Many-Body Complexes in 2D Semiconductors. *Adv. Mater.* **2019,** *31* (2), 1706945.

217. Kam, K. K.; Parkinson, B. A., Detailed Photocurrent Spectroscopy of the Semiconducting Group VIB Transition Metal Dichalcogenides. *J. Phys. Chem.* **1982,** *86* (4), 463-467.

218. Desai, S. B.; Seol, G.; Kang, J. S.; Fang, H.; Battaglia, C.; Kapadia, R.; Ager, J. W.; Guo, J.; Javey, A., Strain-Induced Indirect to Direct Bandgap Transition in Multilayer WSe_2. *Nano Lett.* **2014,** *14* (8), 4592-4597.

219. Kong, L.; Zhang, X.; Tao, Q.; Zhang, M.; Dang, W.; Li, Z.; Feng, L.; Liao, L.; Duan, X.; Liu, Y., Doping-Free Complementary WSe_2 Circuit via Van Der Waals Metal Integration. *Nat Commun* **2020,** *11* (1), 1866.

220. Wang, S.; Zhao, W.; Giustiniano, F.; Eda, G., Effect of Oxygen and Ozone on p-Type Doping of Ultra-Thin WSe_2 and $MoSe_2$ Field Effect Transistors. *Phys. Chem. Chem. Phys.* **2016,** *18* (6), 4304-4309.

221. Wang, T.; Zhao, R.; Zhao, X.; An, Y.; Dai, X.; Xia, C., Tunable Donor and Acceptor Impurity States in a WSe_2 Monolayer by Adsorption of Common Gas Molecules. *RSC Adv.* **2016,** *6* (86), 82793-82800.

222. Arora, A.; Koperski, M.; Nogajewski, K.; Marcus, J.; Faugeras, C.; Potemski, M., Excitonic Resonances in Thin Films of WSe_2: From Monolayer to Bulk Material. *Nanoscale* **2015,** *7* (23), 10421-10429.

223. Qiu, D. Y.; da Jornada, F. H.; Louie, S. G., Optical Spectrum of MoS_2: Many-Body Effects and Diversity of Exciton States. *Phys. Rev. Lett.* **2013,** *111* (21), 216805.

224. You, Y.; Zhang, X.-X.; Berkelbach, T. C.; Hybertsen, M. S.; Reichman, D. R.; Heinz, T. F., Observation of Biexcitons in Monolayer WSe_2. *Nat. Phys.* **2015,** *11* (6), 477-481.

225. Beal, A. R.; Knights, J. C.; Liang, W. Y., Transmission Spectra of Some Transition Metal Dichalcogenides. II. Group VIA: Trigonal Prismatic Coordination. *J. Phys. C* **1972,** *5* (24), 3540-3551.

226. Dneprovskii, V. S.; Zhukov, E. A.; Muljarov, E. A.; Tikhodeev, S. G., Linear and Nonlinear Excitonic Absorption in Semiconducting Quantum Wires Crystallized in a Dielectric Matrix. *J. Exp. Theor. Phys.* **1998,** *87* (2), 382-387.

227. Komsa, H.-P.; Krasheninnikov, A. V., Effects of Confinement and Environment on the Electronic Structure and Exciton Binding Energy of MoS_2 from First Principles. *Phys. Rev. B* **2012,** *86* (24), 241201.

228. Kylänpää, I.; Komsa, H.-P., Binding Energies of Exciton Complexes in Transition Metal Dichalcogenide Monolayers and Effect of Dielectric Environment. *Phys. Rev. B* **2015,** *92* (20), 205418.

229. Jones, A. M.; Yu, H.; Ghimire, N. J.; Wu, S.; Aivazian, G.; Ross, J. S.; Zhao, B.; Yan, J.; Mandrus, D. G.; Xiao, D.; Yao, W.; Xu, X., Optical Generation of Excitonic Valley Coherence in Monolayer WSe_2. *Nat. Nanotechnol.* **2013,** *8* (9), 634-638.

230. Ross, J. S.; Klement, P.; Jones, A. M.; Ghimire, N. J.; Yan, J.; Mandrus, D. G.; Taniguchi, T.; Watanabe, K.; Kitamura, K.; Yao, W.; Cobden, D. H.; Xu, X., Electrically Tunable Excitonic Light-Emitting Diodes Based on Monolayer WSe_2 p–n Junctions. *Nat. Nanotechnol.* **2014,** *9* (4), 268-272.

231. Liu, Y.; Li, H.; Qiu, C.; Hu, X.; Liu, D., Layer-Dependent Signatures for Exciton Dynamics in Monolayer and Multilayer WSe_2 Revealed by Fluorescence Lifetime Imaging Measurement. *Nano Res.* **2020,** *13* (3), 661-666.

232. Casas Espínola, J. L.; Hernández Contreras, X. A., Effect of Dielectric Constant on Emission of CdSe Quantum Dots. *J. Mater. Sci.: Mater. Electron.* **2017,** *28* (10), 7132-7138.

233. Miloszewski, J. M.; Walsh, T.; Tomić, S., Influence of Dielectric Environment on Exciton and Bi-Exciton Properties in Colloidal, Type II Quantum Dots. *J. Phys.: Conf. Ser.* **2015,** *609*, 012003.

234. Sadeghi, S. M.; Wing, W. J.; Gutha, R. R.; Capps, L., Control of Spontaneous Emission of Quantum Dots Using Correlated Effects of Metal Oxides and Dielectric Materials. *Nanotechnology* **2017,** *28* (9), 095701.

235. Sundheep, R.; Prasanth, R., The Effect of Solvent Dependent Local Field Factor in the Optical Properties of CdTe Quantum Dots. *J. Mater. Sci. Mater. Electron.* **2017,** *28* (4), 3168-3174.

236. Issac, A.; Krasselt, C.; Cichos, F.; von Borczyskowski, C., Influence of the Dielectric Environment on the Photoluminescence Intermittency of CdSe Quantum Dots. *ChemPhysChem* **2012,** *13* (13), 3223-3230.

237. Tvrdy, K.; Kamat, P. V., Substrate Driven Photochemistry of CdSe Quantum Dot Films: Charge Injection and Irreversible Transformations on Oxide Surfaces. *J. Phys. Chem. A* **2009,** *113* (16), 3765-3772.

238. Guyot-Sionnest, P., Electrical Transport in Colloidal Quantum Dot Films. *J. Phys. Chem. Lett.* **2012,** *3* (9), 1169-1175.

239. Remacle, F.; Levine, R. D., Quantum Dots as Chemical Building Blocks: Elementary Theoretical Considerations. *ChemPhysChem* **2001,** *2* (1), 20-36.

240. Duan, C.; Wang, Y.; Sun, J.; Guan, C.; Grunder, S.; Mayor, M.; Peng, L.; Liao, J., Controllability of the Coulomb Charging Energy in Close-Packed Nanoparticle Arrays. *Nanoscale* **2013,** *5* (21), 10258-10266.

241. Quinn, A. J.; Beecher, P.; Iacopino, D.; Floyd, L.; De Marzi, G.; Shevchenko, E. V.; Weller, H.; Redmond, G., Manipulating the Charging Energy of Nanocrystal Arrays. *Small* **2005,** *1* (6), 613-618.

242. Laikhtman, B.; Wolf, E. L., Tunneling Time and Effective Capacitance for Single Electron Tunneling. *Phys. Lett. A* **1989,** *139* (5), 257-260.

243. Lannoo, M.; Delerue, C.; Allan, G., Screening in Semiconductor Nanocrystallites and Its Consequences for Porous Silicon. *Phys. Rev. Lett.* **1995,** *74* (17), 3415-3418.

244. Scheele, M.; Engel, J. H.; Ferry, V. E.; Hanifi, D.; Liu, Y.; Alivisatos, A. P., Nonmonotonic Size Dependence in the Hole Mobility of Methoxide-Stabilized PbSe Quantum Dot Solids. *ACS Nano* **2013,** *7* (8), 6774-6781.

245. Ghatak, S.; Pal, A. N.; Ghosh, A., Nature of Electronic States in Atomically Thin MoS_2 Field-Effect Transistors. *ACS Nano* **2011,** *5* (10), 7707-7712.

246. Zhang, Y.; Ma, K.; Zhao, C.; Hong, W.; Nie, C.; Qiu, Z.-J.; Wang, S., An Ultrafast WSe_2 Photodiode Based on a Lateral p-i-n Homojunction. *ACS Nano* **2021,** *15* (3), 4405-4415.

247. Jena, D.; Konar, A., Enhancement of Carrier Mobility in Semiconductor Nanostructures by Dielectric Engineering. *Phys. Rev. Lett.* **2007,** *98* (13), 136805.

248. Chen, F.; Xia, J.; Ferry, D. K.; Tao, N., Dielectric Screening Enhanced Performance in Graphene FET. *Nano Lett.* **2009,** *9* (7), 2571-2574.

249. Schneider, L. M.; Lippert, S.; Kuhnert, J.; Renaud, D.; Kang, K. N.; Ajayi, O.; Halbich, M. U.; Abdulmunem, O. M.; Lin, X.; Hassoon, K.; Edalati-Boostan, S.; Kim, Y. D.; Heimbrodt, W.; Yang, E. H.; Hone, J. C.; Rahimi-Iman, A., The Impact of the Substrate Material on the Optical Properties of 2D WSe_2 Monolayers. *Semiconductors* **2018,** *52* (5), 565-571.

250. Ryou, J.; Kim, Y.-S.; Kc, S.; Cho, K., Monolayer MoS_2 Bandgap Modulation by Dielectric Environments and Tunable Bandgap Transistors. *Sci. Rep.* **2016,** *6* (1), 29184.

251. Borghardt, S.; Tu, J.-S.; Winkler, F.; Schubert, J.; Zander, W.; Leosson, K.; Kardynał, B. E., Engineering of Optical and Electronic Band Gaps in Transition Metal Dichalcogenide Monolayers Through External Dielectric Screening. *Phys. Rev. Mater.* **2017,** *1* (5), 054001.

252. Rösner, M.; Steinke, C.; Lorke, M.; Gies, C.; Jahnke, F.; Wehling, T. O., Two-Dimensional Heterojunctions from Nonlocal Manipulations of the Interactions. *Nano Lett.* **2016,** *16* (4), 2322-2327.

253. Lin, Y.; Ling, X.; Yu, L.; Huang, S.; Hsu, A. L.; Lee, Y.-H.; Kong, J.; Dresselhaus, M. S.; Palacios, T., Dielectric Screening of Excitons and Trions in Single-Layer MoS_2. *Nano Lett.* **2014,** *14* (10), 5569-5576.

254. Liu, D.; Yan, X.-Q.; Guo, H.-W.; Liu, Z.-B.; Zhou, W.-Y.; Tian, J.-G., Substrate Effect on the Photoluminescence of Chemical Vapor Deposition Transferred Monolayer WSe_2. *J. Appl. Phys.* **2020,** *128* (4), 043101.

255. Stier, A. V.; Wilson, N. P.; Clark, G.; Xu, X.; Crooker, S. A., Probing the Influence of Dielectric Environment on Excitons in Monolayer WSe_2: Insight from High Magnetic Fields. *Nano Lett.* **2016,** *16* (11), 7054-7060.

256. Chernikov, A.; Berkelbach, T. C.; Hill, H. M.; Rigosi, A.; Li, Y.; Aslan, O. B.; Reichman, D. R.; Hybertsen, M. S.; Heinz, T. F., Exciton Binding Energy and Nonhydrogenic Rydberg Series in Monolayer WS_2. *Phys. Rev. Lett.* **2014,** *113* (7), 076802.

257. Velizhanin, K. A.; Saxena, A., Excitonic Effects in Two-Dimensional Semiconductors: Path Integral Monte Carlo Approach. *Phys. Rev. B* **2015,** *92* (19), 195305.

258. Murbach, M. D.; Gerwe, B.; Dawson-Elli, N.; Tsui, L.-k., impedance.py: A Python Package for Electrochemical Impedance Analysis. *J. Open Source Softw.* **2020,** *5* (52), 2349.

259. Hsu, C. H.; Mansfeld, F., Technical Note: Concerning the Conversion of the Constant Phase Element Parameter Y_0 into a Capacitance. *Corrosion* **2001,** *57* (9), 747-748.

260. OSRAM Opto Semiconductors, Silicon PIN Photodiode BPW34. 1.1 ed.; 2014, URL: https://asset.conrad.com/media10/add/160267/c1/-/gl/000153005DS01/datenblatt-153005-osram-fotodiode-dil-1100-nm-60-bpw-34.pdf; date accessed: 18.12.2018.

261. OSRAM Opto Semiconductors, Silicon PIN Photodiode SFH 203 P, SFH 203 PFA. 1.1 ed.; 2014, URL: https://asset.conrad.com/media10/add/160267/c1/-/gl/000154029DS01/datenblatt-154029-osram-fotodiode-5-mm-1100-nm-75-sfh-203-p.pdf, date accessed: 21.12.2018.

262. OSRAM Opto Semiconductors, Silicon NPN Phototransistor BPX 81. 1.1 ed.; 2014, URL: https://asset.re-in.de/add/160267/c1/-/gl/000153175DS01/DA_Osram-Fototransistor-Sonderform-1100-nm-18-BPX-81.pdf, date accessed: 23.01.2020.

263. Honeywell, SDP8406 Silicon Phototransistor. URL: https://datasheet.octopart.com/SDP8406-004-Honeywell-datasheet-8398943.pdf, date accessed: 19.03.2019.

264. Davidson, A.; Dessau, K. L. Photodiode-Based Detector Operates at 60 GHz. 2002. URL: https://www.photonicsonline.com/doc/photodiode-based-detector-operates-at-60-ghz-0001; date accessed: 20.03.2019.

265. Newport, User's Guide: High Speed Recievers, High-Speed Detectors. **2013**.

266. Newport, Tutorial - Optical Meters and Detectors. *Photonics* **undated**.

267. Prins, F.; Buscema, M.; Seldenthuis, J. S.; Etaki, S.; Buchs, G.; Barkelid, M.; Zwiller, V.; Gao, Y.; Houtepen, A. J.; Siebbeles, L. D. A.; van der Zant, H. S. J., Fast and Efficient Photodetection in Nanoscale Quantum-Dot Junctions. *Nano Lett.* **2012,** *12* (11), 5740-5743.

268. Ghosh, S.; Varghese, A.; Thakar, K.; Dhara, S.; Lodha, S., Enhanced Responsivity and Detectivity of Fast WSe_2 Phototransistor Using Electrostatically Tunable In-Plane Lateral p-n Homojunction. *Nat Commun* **2021,** *12* (1), 3336.

269. Lippert, S.; Schneider, L. M.; Renaud, D.; Kang, K. N.; Ajayi, O.; Kuhnert, J.; Halbich, M.-U.; Abdulmunem, O. M.; Lin, X.; Hassoon, K.; Edalati-Boostan, S.; Kim, Y. D.; Heimbrodt, W.; Yang, E.-H.; Hone, J. C.; Rahimi-Iman, A., Influence of the Substrate Material on the Optical Properties of Tungsten Diselenide Monolayers. *2D Mater.* **2017,** *4* (2), 025045.

270. Gao, J.; Nguyen, S. C.; Bronstein, N. D.; Alivisatos, A. P., Solution-Processed, High-Speed, and High-Quantum-Efficiency Quantum Dot Infrared Photodetectors. *ACS Photonics* **2016,** *3* (7), 1217-1222.

271. Son, D. I.; Yang, H. Y.; Kim, T. W.; Park, W. I., Transparent and Flexible Ultraviolet Photodetectors Based on Colloidal ZnO Quantum Dot/Graphene Nanocomposites Formed on Poly(ethylene terephthalate) Substrates. *Compos. B. Eng.* **2015,** *69*, 154-158.

272. Robin, A.; Livache, C.; Ithurria, S.; Lacaze, E.; Dubertret, B.; Lhuillier, E., Surface Control of Doping in Self-Doped Nanocrystals. *ACS Appl. Mater. Interfaces* **2016,** *8* (40), 27122-27128.

273. Falk, R. A. In *Near IR Absorption in Heavily Doped Silicon – An Empirical Approach*, ISTFA 2000, Bellevue, Washington, USA., Bellevue, Washington, USA., 2000; pp 121-123.

274. Green, M. A.; Keevers, M. J., Optical Properties of Intrinsic Silicon at 300 K. *Prog. Photovolt.: Res. Appl.* **1995,** *3* (3), 189-192.

275. Jellison, G. E.; Modine, F. A.; White, C. W.; Wood, R. F.; Young, R. T., Optical Properties of Heavily Doped Silicon between 1.5 and 4.1 eV. *Phys. Rev. Lett.* **1981,** *46* (21), 1414-1417.

276. Livache, C. Quantum-Confined Nanocrystals for Infrared Optoelectronics: Carrier Dynamics and Intraband Transitions, p. 67. Sorbonne Université, Paris, France., 2019.

277. SCHOTT AG, Technical Glasses - Physical and Technical Properties. Mainz, 2014.

278. Dammel, R., *Diazonaphthoquinone-Based Resists*. SPIE Optical Engineering Press: Bellingham, Washington, USA, 1993.

279. Chua, L.-L.; Zaumseil, J.; Chang, J.-F.; Ou, E. C. W.; Ho, P. K. H.; Sirringhaus, H.; Friend, R. H., General Observation of n-Type Field-Effect Behaviour in Organic Semiconductors. *Nature* **2005,** *434* (7030), 194-199.

280. Chung, D. S.; Lee, J.-S.; Huang, J.; Nag, A.; Ithurria, S.; Talapin, D. V., Low Voltage, Hysteresis Free, and High Mobility Transistors from All-Inorganic Colloidal Nanocrystals. *Nano Lett.* **2012,** *12* (4), 1813-1820.

281. DUPONT, DuPont™ Kapton® - Summary of Properties, EI-10142 (1/22). 2022.

282. DETAKTA, KAPTON® HN- Polyimid-Folie. Isolier- und Messtechnik GmbH & Co KG: KAPTON® HN- Polyimid-Folie: 2015.

283. Yu, D.; Wang, C.; Guyot-Sionnest, P., n-Type Conducting CdSe Nanocrystal Solids. *Science* **2003,** *300* (5623), 1277-1280.

284. Straus, D. B.; Goodwin, E. D.; Gaulding, E. A.; Muramoto, S.; Murray, C. B.; Kagan, C. R., Increased Carrier Mobility and Lifetime in CdSe Quantum Dot Thin Films Through Surface Trap Passivation and Doping. *J. Phys. Chem. Lett.* **2015,** *6* (22), 4605-4609.

285. Dean, C. R.; Young, A. F.; Meric, I.; Lee, C.; Wang, L.; Sorgenfrei, S.; Watanabe, K.; Taniguchi, T.; Kim, P.; Shepard, K. L.; Hone, J., Boron Nitride Substrates for High-Quality Graphene Electronics. *Nat. Nanotechnol.* **2010,** *5* (10), 722-726.

286. Pradhan, N. R.; Ludwig, J.; Lu, Z.; Rhodes, D.; Bishop, M. M.; Thirunavukkuarasu, K.; McGill, S. A.; Smirnov, D.; Balicas, L., High Photoresponsivity and Short Photoresponse Times in Few-Layered WSe_2 Transistors. *ACS Appl. Mater. Interfaces* **2015,** *7* (22), 12080-12088.

287. Luo, M.; Wu, F.; Long, M.; Chen, X., WSe_2/Au Vertical Schottky Junction Photodetector with Low Dark Current and Fast Photoresponse. *Nanotechnology* **2018,** *29* (44), 444001.

288. Tsai, D.-S.; Liu, K.-K.; Lien, D.-H.; Tsai, M.-L.; Kang, C.-F.; Lin, C.-A.; Li, L.-J.; He, J.-H., Few-Layer MoS_2 with High Broadband Photogain and Fast Optical Switching for Use in Harsh Environments. *ACS Nano* **2013,** *7* (5), 3905-3911.

289. Taffelli, A.; Dirè, S.; Quaranta, A.; Pancheri, L., MoS_2 Based Photodetectors: A Review. *Sensors* **2021,** *21* (8), 2758.

290. Gu, H.; Song, B.; Fang, M.; Hong, Y.; Chen, X.; Jiang, H.; Ren, W.; Liu, S., Layer-Dependent Dielectric and Optical Properties of Centimeter-Scale 2D WSe_2: Evolution From a Single Layer to Few Layers. *Nanoscale* **2019,** *11* (47), 22762-22771.

291. Li, Y.; Chernikov, A.; Zhang, X.; Rigosi, A.; Hill, H. M.; van der Zande, A. M.; Chenet, D. A.; Shih, E.-M.; Hone, J.; Heinz, T. F., Measurement of the Optical Dielectric Function of Monolayer Transition-Metal Dichalcogenides: MoS_2, $MoSe_2$, WS_2 and WSe_2. *Phys. Rev. B* **2014,** *90* (20), 205422.

292. Li, H.-M.; Lee, D.-Y.; Choi, M. S.; Qu, D.; Liu, X.; Ra, C.-H.; Yoo, W. J., Metal-Semiconductor Barrier Modulation for High Photoresponse in Transition Metal Dichalcogenide Field Effect Transistors. *Sci. Rep.* **2014,** *4* (1), 4041.

293. Allain, A.; Kang, J.; Banerjee, K.; Kis, A., Electrical Contacts to Two-Dimensional Semiconductors. *Nat. Mater.* **2015,** *14* (12), 1195-1205.

294. Sanvitto, D.; Pulizzi, F.; Shields, A. J.; Christianen, P. C. M.; Holmes, S. N.; Simmons, M. Y.; Ritchie, D. A.; Maan, J. C.; Pepper, M., Observation of Charge Transport by Negatively Charged Excitons. *Science* **2001,** *294* (5543), 837-839.

295. Lui, C. H.; Frenzel, A. J.; Pilon, D. V.; Lee, Y. H.; Ling, X.; Akselrod, G. M.; Kong, J.; Gedik, N., Trion-Induced Negative Photoconductivity in Monolayer MoS_2. *Phys. Rev. Lett.* **2014,** *113* (16), 166801.

296. Cui, Q.; Ceballos, F.; Kumar, N.; Zhao, H., Transient Absorption Microscopy of Monolayer and Bulk WSe_2. *ACS Nano* **2014,** *8* (3), 2970-2976.

297. Uddin, S. Z.; Kim, H.; Lorenzon, M.; Yeh, M.; Lien, D.-H.; Barnard, E. S.; Htoon, H.; Weber-Bargioni, A.; Javey, A., Neutral Exciton Diffusion in Monolayer MoS_2. *ACS Nano* **2020,** *14* (10), 13433-13440.

298. Kato, T.; Kaneko, T., Transport Dynamics of Neutral Excitons and Trions in Monolayer WS_2. *ACS Nano* **2016,** *10* (10), 9687-9694.

299. Urban, F.; Martucciello, N.; Peters, L.; McEvoy, N.; Di Bartolomeo, A., Environmental Effects on the Electrical Characteristics of Back-Gated WSe_2 Field-Effect Transistors. *Nanomaterials* **2018,** *8* (11), 901.

300. Lu, J.; Carvalho, A.; Chan, X. K.; Liu, H.; Liu, B.; Tok, E. S.; Loh, K. P.; Castro Neto, A. H.; Sow, C. H., Atomic Healing of Defects in Transition Metal Dichalcogenides. *Nano Lett.* **2015,** *15* (5), 3524-3532.